University of Alberta

Polymer Processing in Miniature Mixers

By

Yun Bai   ©

A thesis submitted to the Faculty of Graduate Studies and Research in partial
fulfillment of the requirements for the degree of
Doctor of Philosophy

in

Chemical Engineering

Department of Chemical and Materials Engineering
Edmonton, Alberta

Spring 2008

Canada

Abstract

This thesis investigates processing of polymer blends and nanocomposites in small-scale mixers using experimental and computational approaches. Two main topics are addressed in this thesis: one is non-isothermal modeling of polymer processing in batch mixers using full 3-D geometries and the other is evaluating the mixing efficiency of the small-scale mixers in terms of compounding polymer blends and nanocomposites.

The non-isothermal transient process of temperature increase due to viscous heating was simulated for a 69 mL internal batch mixer (BM), a 3 mL miniature batch mixer (MBM) and a 2 mL Alberta Polymer Asymmetric Mixer (APAM). Numerical simulations were used to obtain the temporal temperature distribution and characterize the heat transfer between polymer melt and the mixer wall. The melt temperatures obtained from simulation were verified with corresponding experimental data. For polystyrene (PS) processed at 50 rpm, viscous heating caused an average temperature rise of 2K for BM, 1K for MBM, and 4K for APAM. The time average heat transfer coefficient is 9 $W/m^2/K$ for BM, 3 $W/m^2/K$ for MBM and 14 $W/m^2/K$ for APAM.

For processing polymer blends and nanocomposites, the miniature mixers (MBM, APAM, and DSM) proved to be comparable to larger mixers (BM and Prism) for compatibilized systems and less efficient for immiscible systems. The in-house built miniature mixer MBM and APAM have an overall superior mixing capability to the commercial miniature extruder DSM based on the simulations and the experimental morphologies of non-reactive systems.

Acknowledgement

First, I would like to express my sincere gratitude to Prof. Uttandaraman Sundararaj and Prof. Krishnaswamy Nandakumar for their guidance, stimulating suggestions and inspiration throughout my thesis research and writing. Their dedication to their jobs and enthusiasm of exploring new fields present me a model to follow in my career. Furthermore, they helped me a lot when I was looking for a job and gave me a full support to start my career before I finished this thesis. Without their support and help, this thesis would be impossible.

I would like to thank my colleagues and friends in the polymer processing group for their help through the past five years. My appreciation goes to Dr. Bin Lin for her help with the rheological data used throughout the thesis and many other help during the experiments. She is also a good friend and helps me a lot in everyday life. I would also like to thank Dr. Hongbin Chen for tutoring me on using Polyflow and many great suggestions and comments on my modeling work; Dr. Kirill Alemaskin for letting me using his program for particle tracking in Chapter 5; Mr. Ben Palathinkal for doing some of the experiments in Chapter 3. My thanks also go to Mr. Bob Barton, Mr. Walter Boddez, Mr. Richard Cooper, and Mr. Les Dean, Ms. Tina Barker in the Department of Chemical and Materials Engineering, University of Alberta for their excellent technical support during my research.

I would like to express my gratitude to Mr. Mark Wetzel in DuPont Experimental Station for providing me the opportunity to carry out the experiments in Chapter 5. I also received lots of help from many other people

TABLE OF CONTENTS

LIST OF TABLES:

List of Figures:

ABBREVIATIONS:

APAM	Alberta polymer asymmetric mixer
BM	Batch mixer
C20A	Cloisite^{R}20A
HDPE	High density polyethylene
LLDPE	Linear low density polyethylene
MBM	Miniature batch mixer
MWCNT	Multi wall carbon nano tube
PA	Polyamide
PE	Polyethylene
PEMA	Maleic anhydride grafted polyethylene
PS	Polystyrene
PSMA	Maleic anhydride grafted polystyrene
TSE	Twin-screw extruder

Nomenclature

A	Local surface area
C_p	Thermal capacity
$\overline{\overline{D}}$	Rate of deformation tensor
g	gravity
h	Heat transfer coefficient
$\overline{h}$	Time-averaged mean heat transfer coefficient
k	Thermal conductivity
L	Characteristic length
m	mass
$\overline{Nu}$	Mean Nusselt number
P	Pressure
Pr	Prandtl number
q''	Local heat flux
Re	Reynolds number
t	Time
Δt	Time interval
T	Temperature
T_m	Measured temperature or melting temperature
V	Velocity vector or Volume

Greek Letters

α	Thermal diffusivity
$\dot{\gamma}$	Shear rate
η	Viscosity
η_0	Zero shear rate viscosity
ρ	Density
$\overline{\overline{\tau}}, \tau$	Stress tensor

Chapter 1

INTRODUCTION

1.1 Polymer processing

Polymers play an important role in industry and everyday life. For example, the clothes we wear are made of polymer fibers, the shopping bags we use are made of plastics and the tires of our cars are made of rubber. However, before raw polymers are used as products, they need to be processed and shaped. The field of polymer processing encompasses the methods used to convert raw polymeric materials to final products. One of its popular definitions was given by Tadmor and Gogos [1]: "operations carried out on polymeric materials or systems to increase their utility".

Few polymers are used alone. Compounding or blending with additives or other materials is necessary to improve polymer properties, appearance, or to reduce cost. Various fillers are incorporated into polymers to fulfill specific requirements. In industry, synthetic rubber and natural rubber are compounded with carbon blacks as well as other additives to improve strength and chemical resistance of the rubber before it is molded into car tires [2].

To achieve the desired property, a polymer can be synthesized from designed monomers that have desirable functional groups, but developing a new polymer is usually very costly and time-consuming. As an alternative, polymer blending is widely used to generate polymeric materials with desired properties in a rapid and economical way [3]. For example, Polyamide (PA) has been blended with

Poly(phenylene ether) (PPE) to obtain a flame retardant material with good chemical resistance and high impact strength contributed by PPE, and good heat deflection temperature provided by PA [4, 5].

The most important sub-process that occurs during polymer blending and compounding is mixing, which can be further subdivided to distributive mixing and dispersive mixing [6]. Dispersive mixing involves breaking down agglomerates of solid particles or clusters of liquid drops into fine structures, while distributive mixing is defined as the process of spreading the minor component throughout the matrix in order to get a good spatial distribution [6, 7]. Understanding and characterizing the mixing process is a difficult task which demands further study.

Currently, twin-screw extruder (TSE), single screw extruder (SSE) and intensive batch mixers are three kinds of mixing equipment widely used in production and research for polymer blending and compounding. While TSE and SSE are continuous mixing equipments and widely used for mixing most polymer blends and polymer composites, the intensive batch mixers are mainly used in the rubber industry for incorporating carbon black and in the laboratory for initial testing.

In addition, before a new product can be produced on the manufacturing scale, small amounts of specially synthesized materials must be processed in miniature mixers. Our group has designed and built new miniature mixers that are useful for processing polymer blends and nanocomposites. The mixing performance of these small-scale mixers is usually compared with the performance of conventional

mixers, especially the internal batch mixer, because of its relatively small capacity and easy operation.

1.2 Internal batch mixer

Internal batch mixers are the earliest mixing equipment used in polymer processing. The first internal batch mixer developed for processing polymer was the Banbury mixer, which was invented by B. F. Banbury in 1916 to incorporate carbon black to rubber [8]. Due to its versatility and ease in controlling operating conditions, large size internal batch mixers are still widely used in rubber industry and laboratory size mixers are extensively used for testing materials and processes.

The internal batch mixer generally consists of two specially designed blades installed in a temperature controlled chamber. Figure 1.1 shows the schematic figure of an internal batch mixer with roller rotors. Different blades such as Banbury blades and sigma blades can be used. A torque meter is used to record the torque change during the process. One of the two roller blades rotates with the shaft rotor at the same speed and the other one is geared to the shaft rotor to rotate at a different speed. A thermocouple protrudes into the polymer melt to track the temperature change during melting and mixing. Other thermocouples are inserted into different parts of the metal barrel to measure the barrel temperature. The operating temperature and rotation speed are controlled by an electronic system, which also records the melting temperature and the applied torque.

Operation of the batch mixer is simple. Once the chamber is heated to the preset temperature, the rotors are turned on to rotate at the desired speed, the

torque is calibrated, and the materials are then fed into the mixing chamber. After

the loading is done, the feeding hole on top is closed to form the closed system.

The materials will be mixed for a desired time and then discharged either by

opening the discharging door or disassembling the mixing chamber. The fillers or

the minor components can also be added into the mixing chamber after the

polymer matrix completely melts or any time during melting.
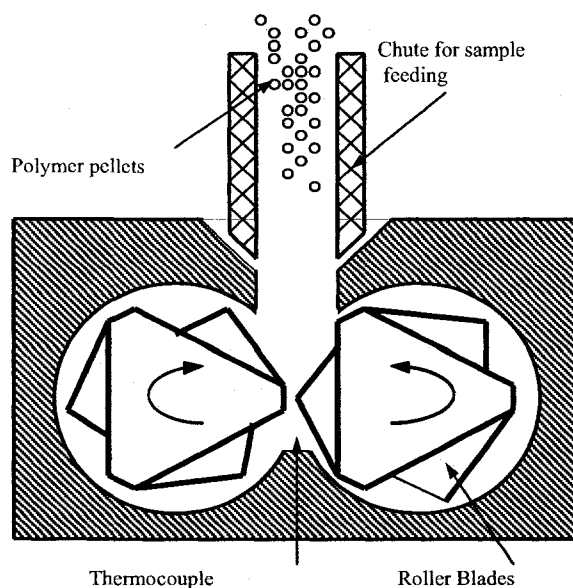
Figure 1.1: Schematic section of an internal batch mixer.

Various rotors have been designed to enhance the mixing performance of the

internal batch mixers. The spiral rotors used in the internal batch mixer are good

to give a pumping, rolling or turning action in the axial direction. As indicated

earlier, the two rotors rotate at different speeds. One of the important factors in

rotor design is the size of the clearance between the rotor tip and the chamber wall.

The flow regions inside the internal batch mixer are divided into two parts: regions of multi-dimensional flow with low shear strain rate and shear stress; regions of unidirectional flow with high shear strain rate and high shear stress. Flows from left rotor side and right rotor side mix and exchange in the region between the two rotors to promote the incorporation and distributive mixing of minor components. The unidirectional flow between the rotor and the chamber wall produces high shear stress to break droplets and particle into finer structures [9].

Heat transfer is another important issue for polymer processing. The high viscosities and low conductivities of polymers make it very difficult to keep an even temperature inside the mixing equipment. It is also difficult to measure more than one point temperature in a batch mixer because of the relatively small volume of the mixing chamber and the high force exerted on the thermocouple. Numerical modeling of polymer processing in mixers can give a more detailed photograph of the temperature field and heat transfer in such devices.

1.3 Development of miniature mixer

To meet the increasing demand to process small amounts of materials, miniature mixers with capacities of a few milliliters have been developed. Most of the miniature mixers are operated in a batch mode because it is difficult to achieve good mixing in a continuous mode with such a small amount of materials and short residence time.

Figure 1.2 shows several commercially available miniature mixers. The first one is known as "MiniMax" and was developed by Maxwell [10]. The mixer consists of a cylindrical mixer sitting in a cup. The mixing is relatively simple
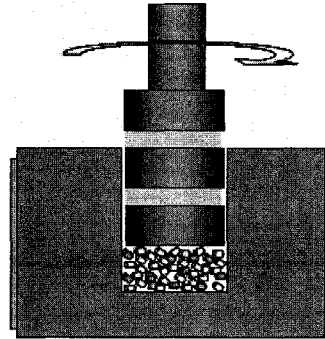
(a)
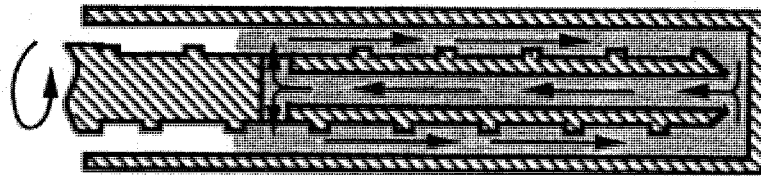
(b)

(c)

Figure 1.2: Three miniature mixers available in the market: (a) MiniMax; (b) Re-circulating screw mixer; (c) Miniature twin-screw extruder (batch).

and the device is easy to operate. However the mixing efficiency is known to be low due to the lack of elongational flow and lack of a high shear stress region. It was shown by Maric et al [11] that the mixing performance can be improved by

adding steel balls. The re-circulating mixer, given in Figure 1.2b, is developed from single-screw extruder and has a hollow channel inside the rotor to promote flow recirculation [12]. Slightly different versions of the mini twin-screw extruders such as the micro-compounder shown in Figure 1.2c are commercially available from DACA instruments [13], DSM Xplore [14], and Thermal Scientific [15]. The Micro-compounder has been extensively used for polymer nanocomposites processing [16-23].

A 3 mL internal miniature mixer (MBM), as shown in Figure 1.3a and 1.3b, was developed in our group. MBM is a miniature version of the commercial internal batch mixer (Haake Instrument) and also driven by the same control system. The details about the MBM are described in Chapter 3.

The Alberta Polymer Asymmetric Mixer (APAM), as shown in Figure 1.4, is another miniature mixer developed in the group and designed as a batch mixer with a single asymmetric screw. The APAM has been tested and used for polymer blends and nanocomposites compounding [24-30].
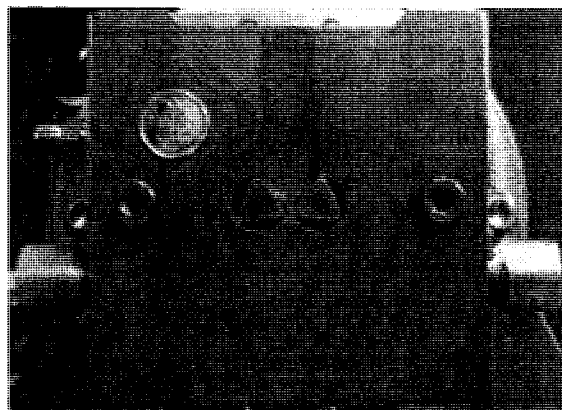
(a)
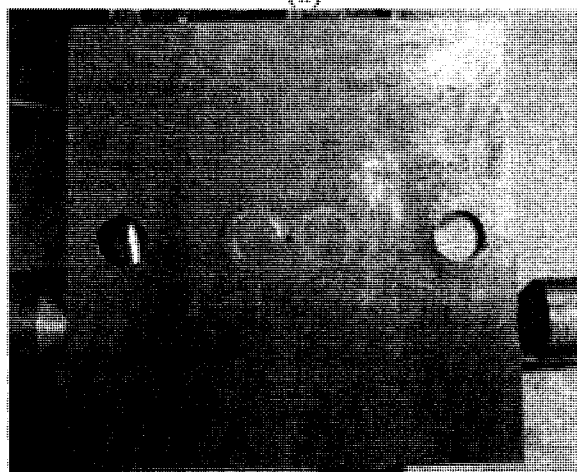
(b)

Figure 1.3: Photograph of MBM: (a) Mixing chamber of MBM; (b) Front plate with thermocouple of MBM.
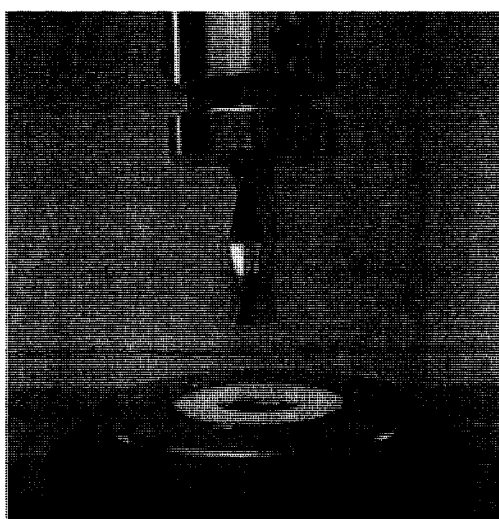
Figure 1. 4: Photograph of the Alberta Polymer Asymmetric Mixer (APAM).

1.4 Numerical simulation of batch mixers

Due to the complex geometries of these mixers, it is difficult to investigate the mixing process by analytical methods. Hence numerical modeling is becoming an alternate tool to study polymer processing, especially in light of the ever-increasing power of computers and sophistication of mathematical and numerical models. `

The governing equations used in the simulations are the conservation laws for mass, momentum and energy as follows

Continuity equation

$$\nabla \cdot V = 0 \tag{1.1}$$

Momentum equation

$$-\nabla p + \nabla \cdot \overline{\overline{\tau}} + \rho(\frac{\partial V}{\partial t} + V \cdot \nabla V) = 0 \tag{1.2}$$

Energy equation

$$\rho_f c_{pf}(\frac{\partial T}{\partial t} + V \cdot \nabla T) - \overline{\overline{\tau}} : \nabla V - \nabla \cdot (k_f \nabla T) = 0 \tag{1.3}$$

where the shear stress τ is related to the rate of strain tensor D through

$$\overline{\overline{\tau}} = 2\eta(\dot{\gamma}, T)\overline{\overline{D}} \tag{1.4}$$

Simulations of polymer melt flow and heat transfer in batch mixers have not been well studied compared to SSE and TSE. Among the available literature, most of batch mixer studies were based on 2-D geometry with the axial cross-section as shown in Figure 1.5 and focused on the flow field such as characterizing flow type and mixing performance [31-34]. Some non-isothermal research has been done using an even simpler 2-D model.
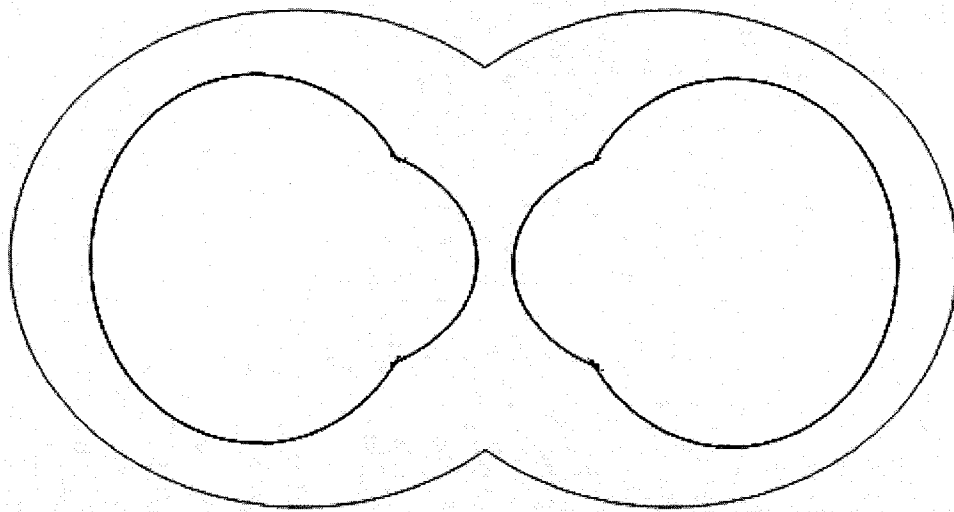
Figure 1. 5: A simplified 2-D representation of a Banbury mixer.

Examples include work done by Hutchinson BC et al [31], who simulated the flow inside a Banbury mixer by boundary element method. They found complex recirculation patterns occurred inside the mixing chamber under isothermal steady-state conditions. The coupled flow and heat transfer simulation was carried out in an eccentric cylinder under constant wall temperature. The maximum temperature was found to be close to the moving boundary resulting from higher velocity gradients in that region. Ghoreishy M. H. R. et al. [32] studied the 2-D temperature distribution between tip part of the rotor and chamber wall with

constant wall and rotor temperature and a higher inlet temperature. The maximum temperature occurred near the inlet where material accumulated. Few of these previous modeling works made comparison between experimental results and model data.

An accurate model of a real scenario representing polymer processing in internal batch mixer is very difficult. First of all, the complex viscous behavior of a polymer is hard to characterize. Several rheological models have been developed to catch the polymer viscosity change with shear rate and temperature. The Power law is commonly used to characterize the viscous behavior of polymeric materials with higher shear rate. At low shear rates, the Bird-Carreau [35], Carreau-Yasuda Law [36] or Cross law [37] is often chosen to capture the plateau zone of the viscosity curve. For each model, several parameters need to be fitted using the experimental data. For temperature dependence, the Arrhenius Law or approximate Arrhenius law is often used. Although none of these models will represent the viscous behavior of polymer exactly, a well chosen model with close fit of the experimental data will give the most accurate results and be very close to reality.

The difficulty for modeling the mixing and heat transfer in the internal batch mixer lies in the complexity of the rotor shapes, which causes difficulties in meshing and requires large memory for calculation. The same difficulty exists in the newly designed miniature mixers as well. Many miniature mixers have been designed and tested by conventional polymer blending or compounding. But the thermal and stress history the materials experience are unknown. At the same

time, it is also difficult to experimentally monitor the pressure and temperature in the small mixers as the extruder does because of a lack of space to make measurements. As an alternative, numerical modeling, especially the non-isothermal modeling with accurate model of the material properties, will help us understand more about the thermal and flow history that the materials experience inside these small mixers and help people design and build more effective mixing devices.

1.5 Computational methods used in this thesis

The simulations in the thesis based on a transient process of the temperature development due to viscous dissipation inside batch mixers. The polymer melt at 190°C was initially static in the mixers. The barrel wall of the mixers was set at constant temperature of 190°C. While rotors started moving, the mechanical energy consumed by the rotors was converted to heat duo to the high viscosity of polymer melt. Part of the generated heat heated the material up and the rest was transferred from the polymer melt to the mixer wall. At a point where the generated heat equals the heat transferred from the polymer melt to the mixer wall, a thermal steady state was then reached. The temperature development and the associated heat transfer during this process were studied in this thesis.

A commercial finite element code, Polyflow 3.9, was used throughout the thesis to solve the governing equations listed previously (Equations from 1-1 to 1-4).

The following assumptions were made in the simulations:

1) The mixer was fully filled with polymer melt.

2) The polymer melt was considered to be incompressible.

3) No-slip boundary condition was applied at the barrel wall and the rotors surfaces.

4) Elasticity of polystyrene and polyethylene at 190°C and 200°C is neglected.

Gambit 1.3 was used to generate the geometry and the meshes of the mixers. For all mixers, the meshes are composed primarily of tetrahedral mesh elements with a small amount of hexahedral, pyramidal, and wedge elements where appropriate.

For mixers with two rotors or two screws, a numerical technique called "mesh superposition technique (MST)" was used to model internal moving parts. By using the MST, the moving parts (solid parts) and the flow domain were meshed separately and no re-meshing is needed during the calculation. A parameter H with a value between 0 and 1 was defined to differentiae the moving parts and the flow domain. H is 1 if an element is inside a moving part and 0 if an element is outside a moving part. The general equations 1-1 to 1-4 were therefore modified as follows:

Continuity equation

$$\nabla \cdot V = 0 \tag{1.5}$$

Momentum equation

$$H(V - \bar{V}) + (1 - H)(-\nabla p + \nabla \cdot \bar{\bar{\tau}} + \rho(\frac{\partial V}{\partial t} + V \cdot \nabla V)) = 0 \tag{1.6}$$

Energy equation

$$(1-H)(\rho_f c_{pf}(\frac{\partial T}{\partial t}+V\cdot\nabla T)-\overline{\overline{\tau}}:\nabla V-\nabla\cdot(k_f\nabla T))+H(\rho_s c_{ps}\frac{\partial T}{\partial t}-\nabla\cdot(k_s\nabla T))=0 \quad (1.7)$$

where the shear stress τ is related to the rate of strain tensor D through

$$\overline{\overline{\tau}} = 2\eta(\dot{\gamma},T)\overline{\overline{D}} \quad (1.8)$$

For mixers with single moving part, a rotating reference frame method is used in the modeling such that the barrel is rotated in an opposite direction to the rotor and the irregular rotor is static. In this way, the numerical mesh is fixed with time and no mesh superposition technique is required.

Material properties of polystyrene (PS) and polyethylene (PE) at 190°C and 200°C were used in the model. All properties other than viscous behavior were assumed to be constant. The Generalized Newtonian model was used to characterize the viscous behavior of PS and PE:

$$\eta(\dot{\gamma},T) = \eta(\dot{\gamma})G(T) \quad (1.9)$$

The Carreau-Yasuda law was used to characterize the viscosity change with shear rate and the approximate Arrhenius law was used to characterize the temperature effect on the viscosity.

The numerical accuracy of the simulations was checked by decreasing the mesh size until a value where a satisfactory information solution was obtained.

The simulations were performed on an IBM RS/6000 Power 4 workstation with 8GB memory.

1.6 Objective of the thesis

This thesis focuses on evaluating various miniature mixers for polymer processing by numerical and experimental methods. The main objective is to investigate the non-isothermal process in batch mixers because of viscous dissipation and characterize the similarity and significance of the mixing, flow field, thermal field and heat transfer for geometrically similar mixers.

The thesis consists of six chapters. Chapter 1 presents an overall introduction to the subject area and the structure of this thesis. Chapter 2 will address the non-isothermal transient process of temperature increase due to heat generated by viscous dissipation in a 69 mL internal batch mixer. Numerical simulations will be presented to obtain the temperature distribution over time and characterize the heat transfer between polymer melt and the mixer wall. The internal batch mixer was experimentally designed to record temperature change at five different points. The simulation results will be verified by comparison with corresponding experimental data.

Chapter 3 will introduce and evaluate a 3 mL internal miniature batch mixer-MBM. MBM will be tested for compounding polymer blends and polymer nanocomposites. Numerical simulations were performed to obtain information about flow field and thermal field. Its mixing performance will be compared to the mixing performance of a commercial internal batch mixer.

Chapter 4 will numerically investigate the different design and sizing of Alberta Polymer Asymmetric Mixer (APAM). Numerical results present design

and sizing effect on the flow field, heat generation, temperature distribution and mixing performance.

Chapter 5 will evaluate the mixing performance of the micro-compounder (DSM) and a small twin screw extruder (Prism).

Chapter 6 will compare and summarize the mixing performance of three miniature mixers: MBM, APAM, and DSM. Future work will also be discussed.

1.7 Reference:

1. Tadmor Z., Gogos C. G., *Principles of Polymer Processing*, Wiley Interscience publication, 1979.

2. Phillips M, The Incredible Tire Journey: From Production to Disposal, *Recycling Today*, Oct00. http://www.mindfully.org/Plastic/Polyester/Tire-Production-DisposalOct00.htm

3. Utracki L. A., *Encyclopedic Dictionary of Commercial Polymer Blends*, Chem. Tech. Publishing, Toronto, 1994.

4. Shaw J. P., "Flame retardant polyamide-polyphenylene ether compositions", *US Patent 5714550*, 1998

5. Brown S. B., Silvi N., Giammattei M. H., Singh N., Khouri, F. F., "Poly(phenylene ether)-polyamide resin blends, method, and articles made therefrom", *US Patent 6362263*, 2002

6. Roger T. Fenner, *Principles of Polymer Processing*, the Macmillan Press LTD, London, 1979.

7. Manas-Zloczower I, "Analysis of mixing in polymer processing equipment", *Rheology Bulletin*, **66 (1),** 5, 1997.

8. Banbury F. H., "Machine for treating rubber and other heavy plastic material", *U. S. Patent: 1,200,070*, 1916.

9. Palmgren H., "Processing conditions in the batch-operated internal batch mixer", *Rubber Chemistry and Technology*, **48**, 463, 1974.

10. Maxwell B., "Miniature injection molder minimizes residence time", *SPE Journal*, **28**, 24, 1972.

11. Maric M, Macosko C. W., "Improving polymer blend dispersions in mini-mixers", *Polymer Engineering and Science*, **41 (1),** 118, 2001.

12. Scott C. E., Macosko C. W., "The Recirculating Screw Mixer: A New Small-Volume Intensive Mixer for the Polymer Laboratory", *Polymer Engineering and Science,* **33,** 1065, 1993.

13. DACA instrument. http://www.daca.com/productsdaca/mcpage.html.

14. DSM Xplore, http://www.xplore-together.com/home.htm

15. Thermal Scientific,

    http://www.thermo.com/com/cda/product/detail/0,1055,21955,00.html

16. Stretz, H.A., Paul, D.R., "Properties and morphology of organoclay/poly(styrene-co-acrylonitrile) nanocomposites: Effect of copolymer composition", *AIChE Annual Meeting, Conference Proceedings,* 4725, 2005.

17. Kumar, S.K.N., Shukla, S.R., Koelling, K.W., "Foaming of PS/clay nanocomposites in supercritical carbon dioxide", *AIChE Annual Meeting, Conference Proceedings,* 1283, 2005.

18. Stretz, H.A. , Paul, D.R., "Properties and morphology of nanocomposites based on styrenic polymers. Part I: Styrene-acrylonitrile copolymers", *Polymer*, **47 (24),** 8123, 2006.

19. Lin, B., Sundararaj, U., Pötschke, P., "Melt mixing of polycarbonate with multi-walled carbon nanotubes in miniature mixers", *Macromolecular Materials and Engineering*, **291(3),** 227, 2006.

20. Loiseau, A., Tassin, J.-F., "Model nanocomposites based on laponite and poly(ethylene oxide): Preparation and Rheology", *Macromolecules*, **39 (26),** 9185, 2006.

21. Cui, L., Paul, D.R., "Evaluation of amine functionalized polypropylenes as compatibilizers for polypropylene nanocomposites", *Polymer*, **48 (6),** 1632, 2007.

22. Pötschke, P., Kretzschmar, B., Janke, A., "Use of carbon nanotube filled polycarbonate in blends with montmorillonite filled polypropylene", *Composites Science and Technology*, **67 (5),** 855, 2007.

23. Abdel-Goad, M.a , Potschke, P. , Zhou, D. , Mark, J.E. , Heinrich, G., " Preparation and rheological characterization of polymer nanocomposites based on expanded graphite", *Journal of Macromolecular Science, Part A: Pure and Applied Chemistry*, **44 (6),** 591, 2007.

24. Breuer, O., Sundararaj, U., Toogood R, "The Design and Performance of a New Miniature Mixer for Specialty Polymer Blends and Nanocomposites", *Polymer Engineering and Science*, **44 (5),** 868, 2004.

25. Breuer, O., Chen, H., Lin, B., Sundararaj, U., "Simulation and visualization of flow in a new miniature mixer for multiphase polymer systems", *Journal of Applied Polymer Science* , **97 (1),** 136, 2005.

26. Sundararaj, U., Bai, Y., Nandakumar, K., "CFD study of flow and heat transfer in miniature mixers for nanocomposites", *AIChE Annual Meeting, Conference Proceedings* 2005, Page 5552.

27. Bai, Y., Sundararaj, U., Nandakumar, K. , "CFD study of flow pattern and heat transfer in miniature mixers using a generalized' newtonian fluid", *Annual Technical Conference - ANTEC, Conference Proceedings*, **1**, 391, 2005.

28. Lin, B., Sundararaj, U., Guegan, P., "Effect of mixing protocol on compatibilized polymer blend morphology", *Polymer Engineering and Science*, **46 (5),** 691, 2006.

29. Bai, Y., Sundararaj, U., Nandakumar, K., "Modification and scale-up of the new miniature mixer-APAM", *Annual Technical Conference - ANTEC, Conference Proceedings*, **2,** 918, 2006.

30. Lin, B., Sundararaj, U., Potschke, P., "Melt mixing of polycarbonate with multi-walled carbon nanotubes in miniature mixers", *Macromolecular Materials and Engineering,* **291 (3),** 227, 2006

31. Hutchinson B. C., Rios A. C., and Osswald T. A., "Modeling the Distributive Mixing in an Internal Batch Mixer", *International Polymer Processing*, **14,** 315, 1999.

32. Ghoreishy M. H. R. and Nassehi V., "Modeling the transient flow of rubber compounds in the dispersive section of an internal mixer with slip-stick boundary conditions ", *Advances in Polymer Technology*, **16,** 45,1997.

33. Jongen T., "Characterization of batch mixers using numerical flow simulations", *AIChE Journal*, **46,** 2140, 2000.

34. Gramann P. J., Mätzig J. C., Osswald T. A., "Simulating the non-isothermal mixing of polymer blend using the boundary element method", *Journal of Reinforced Plastics and Composites*, **12**,787,1993.

2

CHAPTER 2

NON-ISOTHERMAL MODELING OF AN
INTERNAL BATCH MIXER

2.1 Introduction

The internal batch mixer is an important piece of polymer mixing equipment that is widely used in rubber processing and research laboratories for preliminary testing such as new materials development, studying polymer-polymer interactions and verifying mixing quality [1-6]. The mixer consists of two roller blades counter-rotating in a mixing chamber. The mixing domain of the internal batch mixer can be divided into two parts: (1) the narrow region between the rotor tip and chamber wall with unidirectional flow at high temperature and high intensities of shear stress; and (2) the rest of the mixer with multi-directional flow at lower temperature and lower intensities of shear stress [7, 8]. The high viscosities of polymers and the large shear rates generated by the narrow gap may result in a significant increase in temperature due to viscous dissipation [9-11]. A better understanding of temperature distribution and flow pattern inside the internal mixer would potentially provide useful information to evaluate mixing performance of this equipment.

The approximate shear rate and shear stress in the unidirectional region of an internal batch mixer can be obtained from its rotor speed and torque [12-18]. By approximating the mixer as two concentric cylinder viscometers and using a Newtonian fluid, Goodrich et al [12] calculated the viscosity, shear rate, and shear

stress inside the mixer. For polyethylene and polystyrene, the calculated viscosity data are comparable with those obtained using an Instron capillary rheometer. Based on Goodrich's work, Bousmina and coworkers [16, 17] developed more detailed correlations that derive the viscosity data from the torque rheometer for a Non-Newtonian viscosity model. Although an average shear rate and shear stress in the unidirectional flow region can be obtained from these analytical models, the local flow information in that region is still missing and the shear rate and shear stress in the multi-directional flow region are unknown.

The flow field and mixing performance of an internal batch mixer have been studied by various researchers under isothermal and non-isothermal conditions [18-26]. Various viscous models have been used to characterize the non-Newtonian behavior of a polymer melt, but most of the work was based on a 2-D geometry and the axial flow in the rotor axis directions was neglected. Non-isothermal 3-D modeling for a Banbury-type mixer was first studied by Kim et al [27] using the hydrodynamic lubrication theory and a rotating reference frame.

In this study, we study the transient process of the temperature development due to viscous dissipation inside an internal batch mixer using 3-D non-isothermal CFD modeling. Batch mixers are usually operated at a constant wall temperature well above the material's melting temperature. Once materials are added to the mixer, heat is transferred from the mixer wall to melt the material, and the temperature of the material increases. During this process, energy is supplied both from the heaters inside the barrel and by the viscous heating imposed by rotating the rotors. After the temperature of material reaches the wall temperature,

it continues to increase due to heat generated by viscous dissipation until reaching a thermal steady state. At this point, energy is supplied by viscous heating only and heat is transferred from the polymer melt to the mixer wall. When thermal steady state is reached, the heat transfer rate across the wall equals the power consumed. To keep the wall temperature constant, heat from the polymer melt needs to be removed from the mixer wall instantly. For the large-scale batch mixers used in industry, the mixer is cooled using cooling water or air, and the heat transfer rate can be controlled by adjusting the flow rate of the cooling fluid. Because of the small volume of the miniature batch mixer, however, most of the small-size batch mixers used at laboratories are often cooled by surrounding air and it is assumed that the heat removed by natural convection is sufficient to keep the wall temperature constant. In this chapter, we investigated the heat transfer during this viscous-heating dominated process to verify whether a constant wall temperature can be maintained by natural air convection for a 69 mL internal batch mixer.

In previous simulations of heat transfer in internal batch mixer, various simplified geometry and simplified conservation equations were used. For an accurate representation of the realistic scenario, a numerical model with full 3-D geometry and the complete conservation equations is needed to catch the details of flow field and temperature development. The model results need to be compared with experimental data. In our work, the entire process was simulated using a commercial finite element code, Polyflow 3.9, for the full 3-D batch mixer

geometry and the mesh superposition technique was used to handle the motion of the irregular counter-rotating elements.

2.2 Experiment

The Haake Rheocord 90 Torque Rheometer fitted with a Series 600 internal batch mixer was used for the experiment. The rollers and the experimental set-up are shown in Figure 2.1. The barrel temperature was preheated to 190°C. The speed of the left rotor, seen from the front of the mixer, is 50 rpm and the right
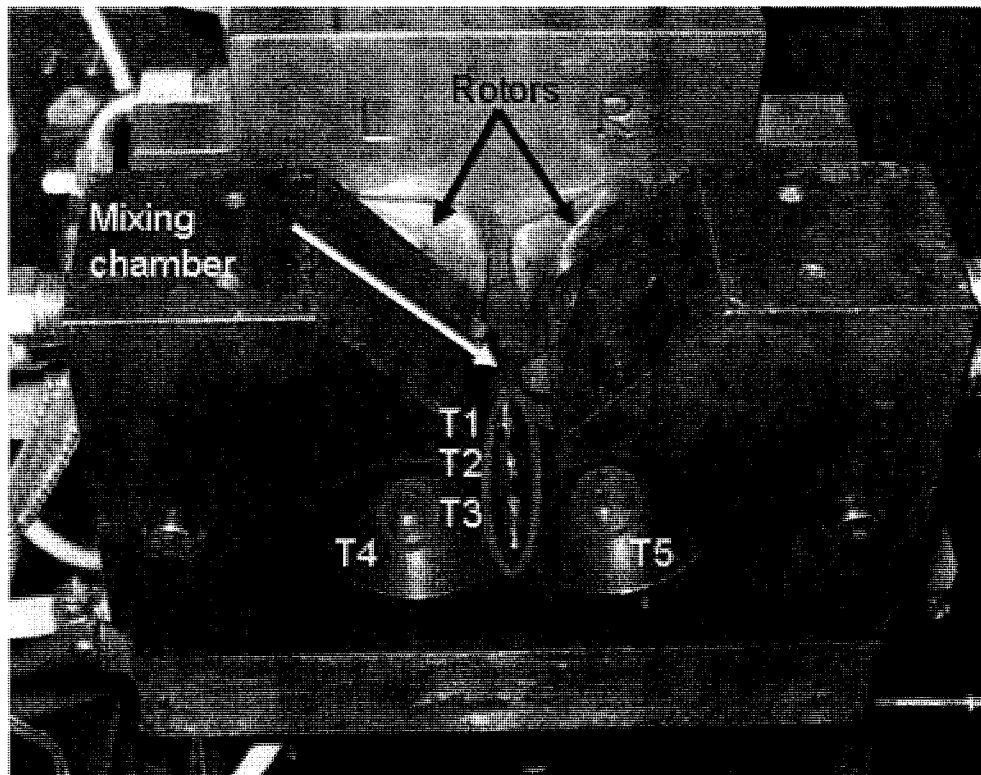
Figure 2.1: **Experimental set-up to record temperatures at five locations. The thermocouples' protrusion: T1: 0.5 mm; T2: 1 mm; T3: 1.5 mm; T4&T5: 0.2 mm.**

rotor is rotated at 2/3 of left rotor speed but in the opposite direction. Five thermocouples were placed into the mixing chamber to monitor the temperatures of polymer melt at different locations. T1, T2, T3 were located in the middle part

between the two rotors and were inserted into the polymer melt 0.5 mm, 1 mm and 1.5 mm from the wall respectively. T4 and T5 were placed into the left chamber and right chamber respectively and each protruded 0.2 mm into the mixer. All five thermocouples were type K with a diameter of 3.175 mm (0.125 inch). The response time of the thermocouples was 0.6 s.

The polymer pellets were stuffed until the mixer was fully filled. After the polymer pellets were completely melted, the melt temperature gradually increased until finally reaching constant values, which meant that a thermal steady state was reached. The motor was then stopped and the temperatures slowly decreased to the wall temperature. After the temperature was constant for 5 minutes, the motor was re-started. The melt temperature and the associated torque were recorded every second using an OPTO 22 data-acquisition system. During the re-starting process, only viscous dissipation contributed to the polymer melt's temperature increase. The above process was repeated three times to check reproducibility.

High-density polyethylene (PE, Petromont, Canada) and Polystyrene (PS, Dow Chemical) were used in the experiments. The rheological properties of PE and PS were measured using a Rheometrics RMS 800 rheometer with parallel-plate fixtures. The shear viscosities of PE and PS at 190°C and 200°C are shown in Figure 2.2. The PE viscosity vs. shear rate at 190°C and 200°C are close to each other, so the viscosity dependence on temperature is neglected and the viscosity dependence on shear rate is characterized by Carreau-Yasuda law:

$$\eta = 1580 \, [1 + (0.17 \, \dot{\gamma})^{0.64}]^{\frac{0.7-1}{0.64}} \qquad (2.1)$$

The combined Approximate Arrhenius law and Carreau-Yasuda law is used to

characterize the viscosity change of PS versus shear rate and temperature:

$$\eta = [\exp(-0.006466\,(T-463))] \cdot 8357.8\left[1 + (0.3347\,\dot{\gamma})^{0.6686}\right]^{\frac{0.3215-1}{0.6686}} \qquad (2.2)$$

Other properties of PE and PS are summarized in Table 2.1. The rotor properties

were assumed to be the same as those of the stainless steel AISI 316.
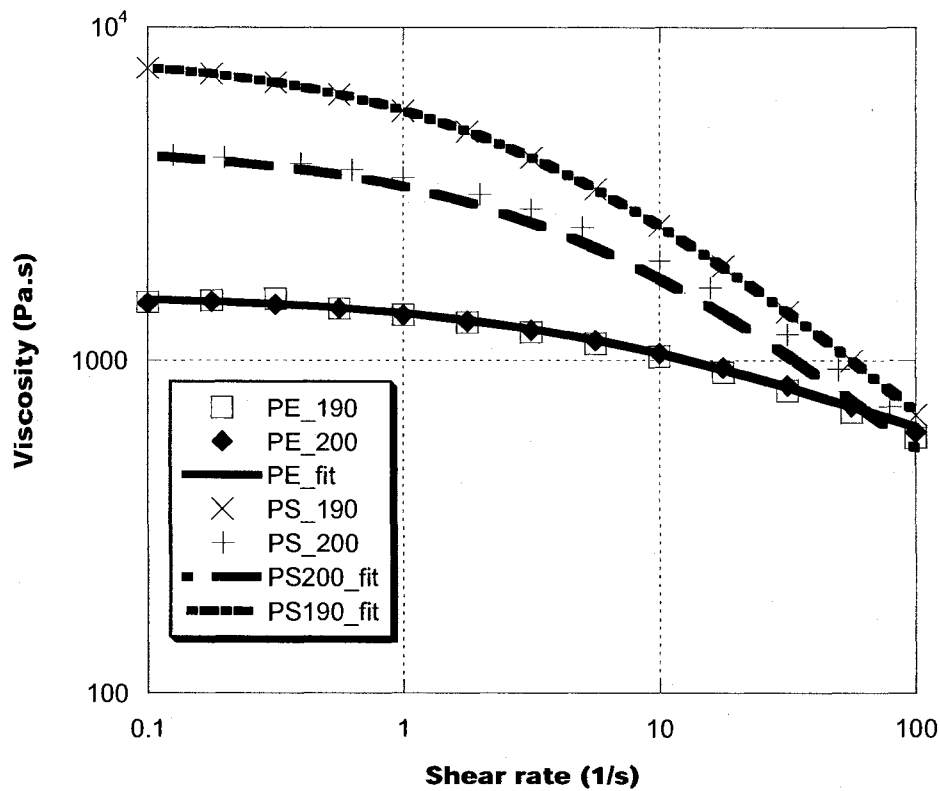
Figure 2.2: The viscosity data of PE and PS at 190°C and 200°C.

Table 2.1: Properties of polymer and rotor.

	Density at 200 °C (kg/m^3)	Thermal capacity (J/kg/K)	Thermal conductivity (W/m/K)	Viscosity (Pa·s)
PE	740	2100	0.182	Eq.1
PS	882	2098	0.123	Eq.2
Rotor	8000	400	15	Not available

2.3 Computational Model

The following assumptions were made in the simulations:

5) The mixer was fully filled with polymer melt.

6) The polymer melt was considered to be incompressible.

7) The no-slip boundary condition was applied at the barrel wall and the rotors surfaces.

Gambit 1.3 was used to generate the geometry and the meshes of the internal batch mixer as shown in Figure 2.3. The mesh is composed primarily of tetrahedral mesh elements with a small amount of hexahedral, pyramidal, and wedge elements where appropriate. The average mesh size of the elements is about 0.8mm with a larger size of 1mm in the moving parts and a smaller size of 0.1mm in the gap areas.
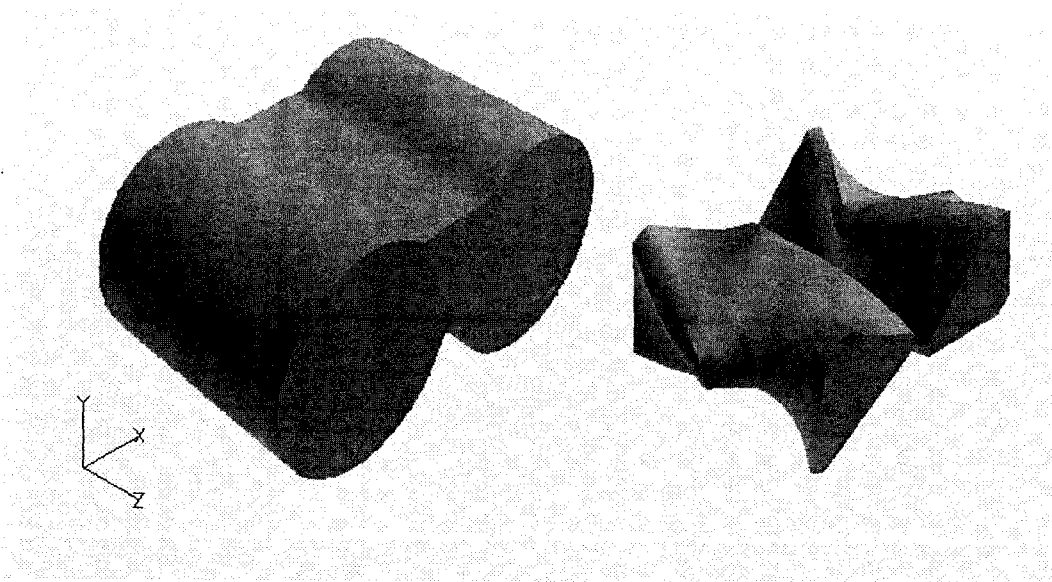
Figure 2.3: Geometry of the internal batch mixer and the roller blades.

The governing equations used in the simulation are the conservation laws for mass, momentum and energy. A mesh superposition technique (MST, Polyflow) was used to model internal moving rotors and the conservation equations are as follows:

Continuity equation

$$\nabla \cdot V = 0 \qquad (2.3)$$

Momentum equation

$$H(V - \overline{V}) + (1 - H)(-\nabla p + \nabla \cdot \overline{\overline{\tau}} + \rho(\frac{\partial V}{\partial t} + V \cdot \nabla V)) = 0 \qquad (2.4)$$

Energy equation

$$(1 - H)(\rho_f c_{pf}(\frac{\partial T}{\partial t} + V \cdot \nabla T) - \overline{\overline{\tau}} : \nabla V - \nabla \cdot (k_f \nabla T)) + H(\rho_s c_{ps} \frac{\partial T}{\partial t} - \nabla \cdot (k_s \nabla T)) = 0$$

$$(2.5)$$

where the shear stress τ is related to the rate of strain tensor D through

$$\overline{\overline{\tau}} = 2\eta(\dot{\gamma}, T)\overline{\overline{D}} \qquad (2.6)$$

and H is a step function, which is 0 for fluid field and 1 for inner moving part. These equations were numerically solved using the finite element code, Polyflow3.9 from Fluent Inc (now ANSYS Inc). The thermal boundary conditions (TBC) and flow boundary conditions (FBC) for the simulations are summarized in Table 2-2.

Table 2.2: Boundary conditions used in the simulations.

	Flow BC	Thermal BC
Left rotor	-5.24 s^{-1}	Not applicable
Right rotor	3.49 s^{-1}	Not applicable
Barrel wall	$V_n = 0$	T= 493 K
	$V_s = 0$	

The simulations were performed on an IBM RS/6000 Power 4 workstation with 8 GB memory. It took an average of three weeks to complete each run.

2.4 Results and Discussion

2.4.1 Heat transfer

2.4.1.1 Self-heating "heat transfer inside mixer"

We studied the temperature evolution of polymer melt in an internal batch mixer at a constant wall temperature. The two roller blades counter-rotate with a specific rotation speed ratio of 3:2 (Left rotor: right rotor) and the left rotor's rotational speed is 50 rpm. So at 50 rpm the left rotor rotates in a repeated cycle of 1.2 s and the right rotor rotates in a repeated cycle of 1.8 s. The two rotors come back to their initial configuration every 3.6 s. The initial temperature of the polymer melt is the same as the wall temperature and the temperature increases because of the heat generation caused by viscous dissipation. The energy balance can therefore be expressed in the following form:

$$q_{st} = \frac{d(mc_p T)}{dt} = q_g - q_{out} \qquad (2.7)$$

where q_{st} is the rate of change of stored energy in the melt which determines the temperature of the material, m is the amount of PS in the mixer, C_p is the heat capacity of PS, T is the temperature, q_g is rate of heat generation due to viscous dissipation, and q_{out} is the heat transfer from polymer melt to the mixer wall. The temperature of the polymer melt keeps increasing until the heat transferred to the mixer wall equals the heat generated by viscous dissipation. A thermal steady state is then achieved. This steady state is periodically stable due to the rotors' configuration and rotational speed ratio. At 50 rpm, the flow repeats every 3.6 s.

In the experiments, the torque evolution during the transient process was recorded for two cases: PE melt and PS melt. The total mechanical power versus time, plotted in Figure 2.4, was obtained by multiplying the measured torque with the angular speed. The transient curves show that the power consumed jumps up from zero to its highest value when the rotors start rotating, and then gradually decreases to a constant value, which indicates that a thermal steady is reached.

In the simulation, the heat generation rate q_g was calculated according to the following equation:

$$q_g = \int_V tr(\sigma : D) dv \tag{2.8}$$

where σ is the Cauchy stress tensor, D is the rate of deformation tensor, $tr(\sigma : D)$ is the sum of the diagonal term of $\sigma : D$, V is the total volume of the mixer. The hear transfer rate q_{out} is calculated as the magnitude of the heat flux integrated over the mixer wall:

$$q_{out} = \iint_A \| -k\nabla T \| dA \tag{2.9}$$

where k is the heat conductivity of polymer melt, ∇T is the temperature gradient,

and A is the total surface area of the mixer.
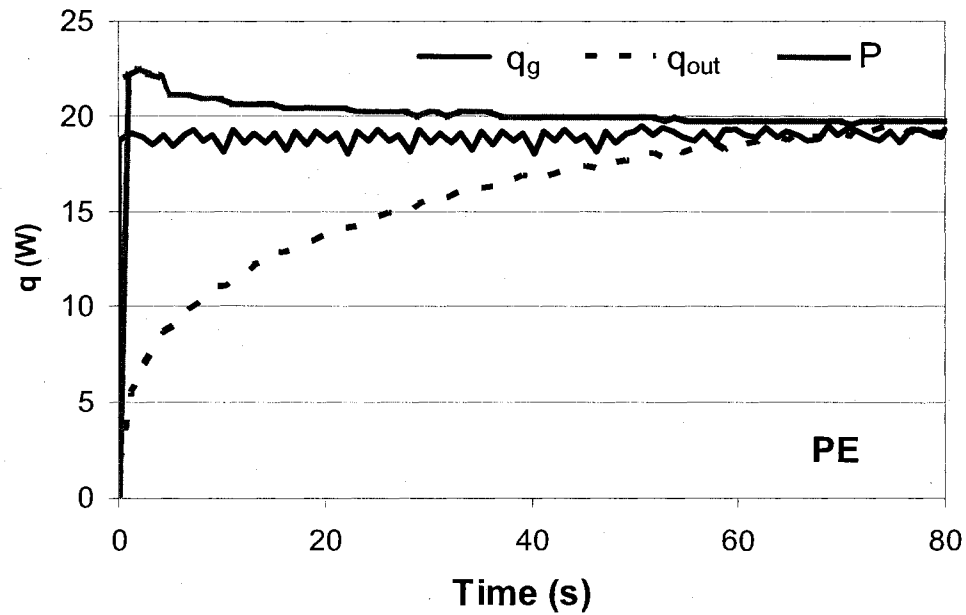
(a)
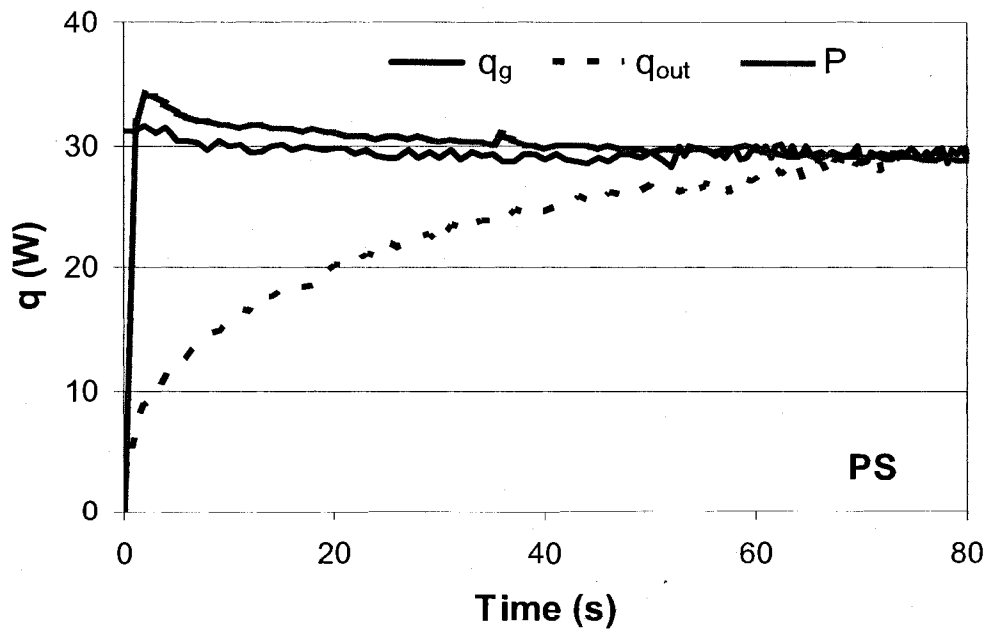
(b)

Figure 2.4: Viscous dissipated power, overall heat transfer rate and experimental power for (a): PE; (b) PS.

The evolution of q_g and q_{out} is plotted in Figure 2.4a for PE melt and Figure 2.4b for PS melt. Although the mechanical power P should all be converted into heat q_g generated by viscous dissipation in the polymer melt, it is found out that the experimentally measured P is initially higher than the theoretically calculated q_g and then is slightly lower than q_g after thermal steady is reached. One explanation is that initially, part of mechanical energy is lost to overcome the frictional force in the bushings outside the mixer when the rotors start rotating. In the rubber industry, it was reported that the mechanical loss in a large internal batch mixer is usually 10-15% of the total consumed energy depending on the size of the mixer [28, 29]. In our case, the mechanical loss is much smaller because of the small size of the mixer (69 mL) and because a torque calibration that was done with an empty mixer.

During the transient process, the heat generation by viscous dissipation raised the temperature of the material and therefore a temperature gradient was created between the polymer melt and the mixer wall. As temperature increases, the heat transfer rate q_{out} increases with time and finally equals the heat generation rate, as shown in Figures 2.4a and 2.4b. On the other hand, the temperature increase of the material resulted in a lower viscosity, and this in turn lowered the heat generation rate because the heat generation rate is proportional to material's viscosity according to Equation 2.8. Because the viscosity of PE is less dependent on temperature than on the viscosity of PS, the rate of heat generated by viscous dissipation for PE does not change much over time while the rate of heat generated by viscous dissipation for PS gradually decreases. For both

materials, it takes about 80 s to reach steady state. The PS melt generally consumes more power than does the PE melt because of the higher viscosity of PS.

2.4.1.2 Self-heating "heat transfer outside mixer"

The heat transfer rate q_{out} from the simulation is plotted in Figure 2.4a for PE melt and Figure 2.4b for PS melt. The corresponding overall heat transfer coefficient can be calculated from the value of q_{out} using the following formula:

$$h = \frac{q_{out}}{A_s (T_w - T_\infty)} \tag{2.10}$$

where A_s is the total outside barrel wall surface area, T_w is the constant wall temperature (463K) and T_∞ is the surrounding room temperature (about 298K). If the instantaneous wall temperature is always constant, the temperature difference between the wall and the surrounding air would be constant. The overall heat transfer coefficient would be proportional to the calculated heat transfer rate and would be as shown in Figure 2.5 for both PE and PS, increasing over time for both materials.
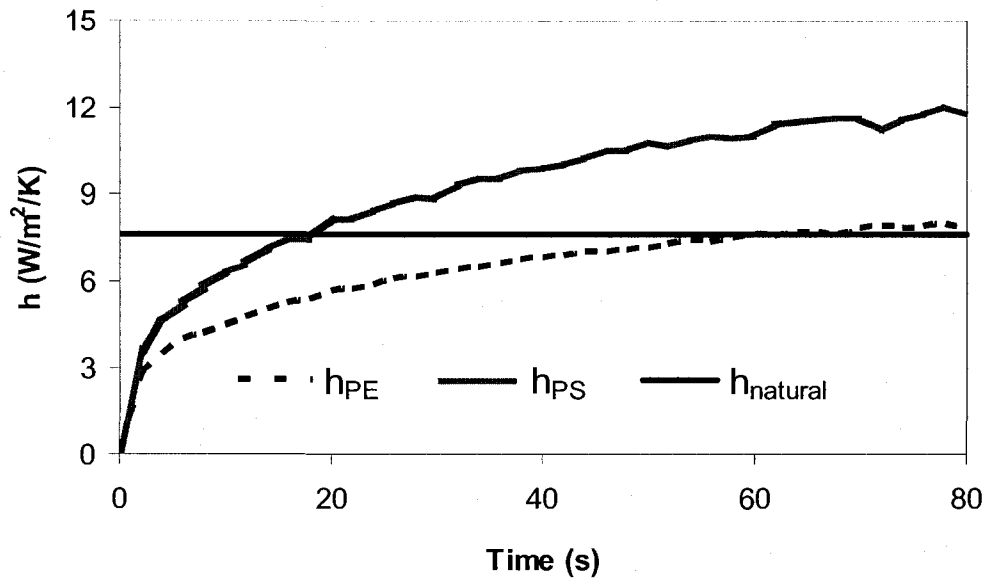
Figure 2.5: Overall heat transfer coefficient during the transient process.

In reality, the front and back walls of the mixer are vertical plates and have a much larger area than the side walls do. So the heat loss from the side walls can be neglected. For a steady free convection flow over the vertical plates, the Churchill-Chu correlation equation [30] as follows can be used to calculate the overall natural convection heat transfer coefficient:

$$\overline{Nu} = 0.68 + \frac{0.670 Ra^{1/4}}{[1+(0.492/\Pr)^{9/16}]^{4/9}} \qquad Ra \le 10^9 \qquad (2.11)$$

The Nusselt number and the Rayleigh number are expressed as:

$$\overline{Nu} = \frac{\overline{h}_{Natural} L}{k} \qquad (2.12)$$

$$Ra = \frac{g\beta(T_w - T_\infty)L^3}{v\alpha} \qquad (2.13)$$

Based on the properties of air at the average temperature of 381K (averaging T_w (463K) and T_∞ (298K)), the Prandtl number is Pr = 0.6939 and the Rayleigh number is $Ra = 9.92 \times 10^6$ for this work. From this correlation, the natural convection heat transfer coefficient was calculated to be 7.62 W/m^2/K and this rate is shown in Figure 2.5. When the instantaneous overall heat transfer coefficient is lower than $\overline{h}_{Natural}$, heat removed by the surrounding air is greater than the heat transferred from polymer melt and the heaters inside the wall work to keep the wall temperature constant. When the instant overall heat transfer coefficient is higher than $\overline{h}_{Natural}$, the heat removed by the atmosphere is less than the heat transferred from polymer melt to the wall and will accumulate inside the wall to raise the wall temperature. As a result of wall temperature increase, less heat is transferred out from polymer melt and in turn the polymer melt temperature increases. A high polymer melt temperature can result in polymer degradation and other problems.

For the PE melt, the instantaneous heat transfer coefficient to the wall is lower than the natural convection heat transfer coefficient for the first 50s and slightly higher afterwards. Because the surface area of the mixer and the temperature difference between the wall and the surrounding air (constant wall temperature, constant surrounding air temperature) are constant, after thermal steady state is reached, the wall temperature can be kept constant via air convection only. For the PS melt, the instantaneous heat transfer coefficient to the wall increases quickly and is greater than the calculated $\overline{h}_{Natural}$ after about 20 s. The heat transferred from the PS melt can't be completely removed by air convection and

the PS melt temperature will be higher than it should be from the numerical simulation where a constant wall temperature was assumed. In the experiments, we also found that the wall temperature increased 1-2K over the simulated temperature for the PS melt while it matched the simulation result for the PE melt.

The time averaged heat transfer coefficient $\bar{h}$ from the simulation is found using

$$\bar{h} = \frac{\sum_{n=1}^{N} \bar{h}(t) \cdot \Delta t}{N \cdot t} \qquad (2.14)$$

where Δt is the time step and N is the number of time steps. The time average heat transfer coefficient is 6.3 W/m^2/K for PE and 9.2 W/m^2/K for PS. These values are close to the natural convection heat transfer coefficient determined from the Churchill-Chu correlations, so this indicates that air convection can remove most of the heat generated in the polymer melt due to viscous heating.

2.4.2 Temperature evolution

The melt temperature at three middle locations versus time for the experiment and the simulation are shown in Figure 2.6a for PE melt and Figure 2.6b for PS melt. Three thermocouples marked as T_1, T_2 and T_3 are located in the middle ridge of the mixer as shown in Figure 2.1. The predicted temperatures are taken from the simulation at the same points. To understand the temperature gradient close to the wall, the thermocouples protruded into the mixer at different depths. For both polymers, it takes about the same time for the three temperatures to reach their corresponding thermal steady-state temperatures. The time for the

temperature to reach thermal steady state from the simulation also matches well with the time obtained from the experiment. All temperatures initially increase with time until the thermal steady state is achieved. The experimentally measured T_2 and T_3 match each other in the first 80 s while the experimentally measured T_1 is always lower than T_2 and T_3. Since the temperature of polymer melt inside the mixer is always higher than the preset wall temperature in our work, the measured temperatures at locations closer to the wall are lower than the temperature away from wall even though this may not represent the actual melt temperature. The actual melt temperature at locations near the walls will be higher than that measured due to the interface of the controlled constant barrel temperature which will lower the temperature measured. Even though thermocouple 3 has a 0.5mm deeper protrusion into the melt than thermocouple 2, the recorded temperatures are about the same because thermocouple 3 is closer to the front wall while thermocouple 2 is in the middle of the mixer where it should be hotter. Thermocouple 1 is close to the back wall and has the less protrusion into the melt, so the recorded temperature T_1 is much lower than the other two. Experimentally, viscous heating causes about a 3K increase for the PE melt and a 6K increase for the PS melt at all three locations.

The temperatures predicted from the simulation at the same three locations have curves similar to the measured data except that in the simulation results, T_2 is slightly higher than T_3. The difference between the experimental data and the predicted data is due to the fact that the wall temperature is constant over the
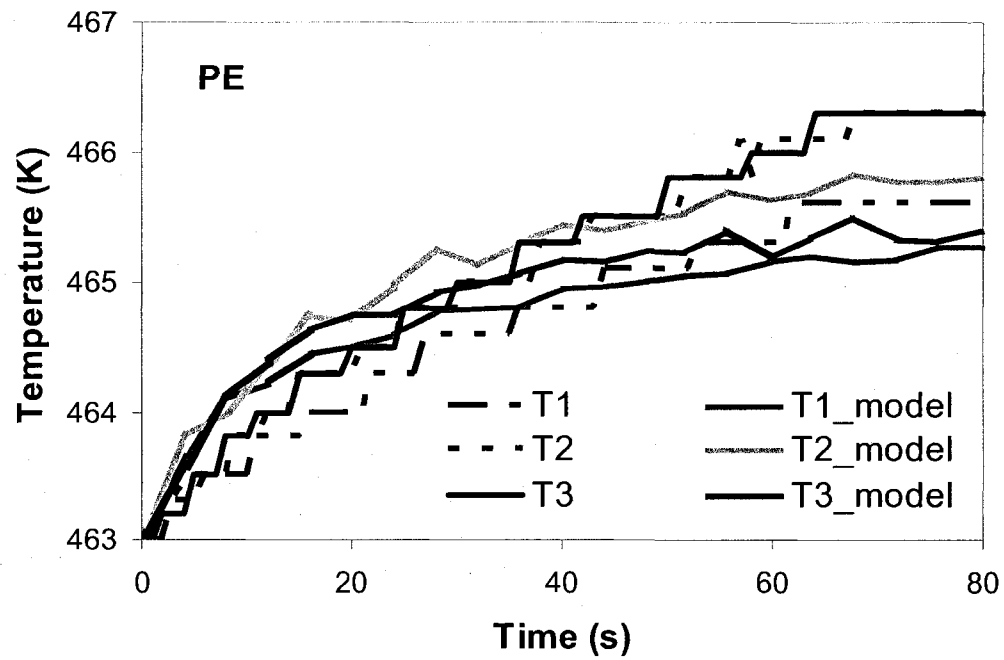
(a)
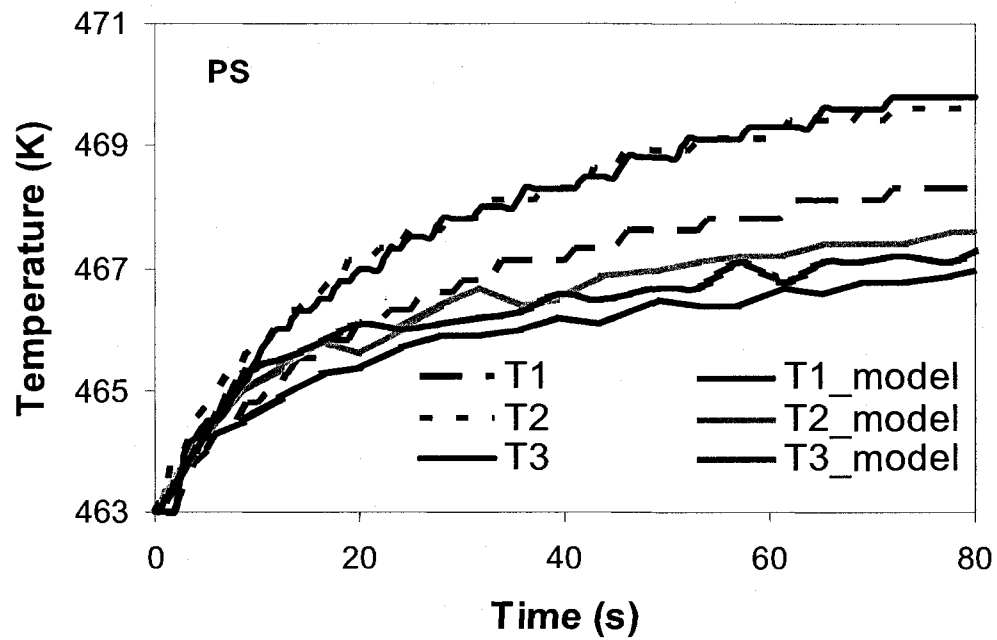
(b)

Figure 2.6: Comparisons of the experimentally measured point temperatures   at three different locations with those predicted from the simulations: (a) PE; (b) PS.

whole process in the simulation, while in the experiment the wall temperature fluctuates somewhat around the pre-set temperature because of the inefficient heat removal by natural air convection. This is especially true for the PS case (Figure 2.6b) because the heat transfer coefficient in the melt is greater than the heat transfer coefficient due to natural convection outside the mixer (see Figure 2.5). In addition the measured temperatures at the locations closer to the front and back walls have a larger deviation from the simulated value.

While the wall temperature of the mixer in the simulation can be fixed, the wall temperature of the mixer in reality is controlled by a dynamic system. For all internal batch mixers, the mixer walls have a built-in heating system to supply heat. Although larger internal batch mixers also have a controlled cooling system to remove heat either by forced air or water cooling, the mixer used in our experiments is cooled by the surrounding air only. During a heating process, the heating system inside the wall not only supplies heat to the material inside the mixer, but also provides heat to the surrounding air because the operating temperature is always much higher than room temperature. During the cooling process, the heat transferred from the material to the wall is removed by the air surrounding the mixer and the actual wall temperature tends to be slightly higher than the pre-set wall temperature, which results in the slightly higher overall rate of heat transfer.

Thermocouple T_4 and T_5 are located at the bottom of the left chamber and the right chamber respectively. Because of the small clearance between the tips of the rotors and the wall, T_4 and T_5 are only inserted into polymer melt about

0.2mm. Figure 2.7 shows the comparisons of the experimentally measured temperatures with predicted ones from simulation. Close to the mixer wall, the temperatures measured by these two thermocouples are much lower than the other three in the middle. In our work, the left rotor of the mixer runs 50% faster than the right one. So the temperature next to the left rotor will be greater than that near the right rotor.

For the same clearance between the rotors and the wall, higher rotational speed (i.e. rotor tip velocity) means a higher shear rate and more viscous heating. Therefore, at longer times, the average temperature in the left chamber is always higher than the average temperature in the right chamber. Using the same reasoning that was for T_1, T_2 and T_3, the measured values at T4 and T5 are also higher than the predicted ones. At shorter times, because the thermocouples at the left and right chamber are located so close to the barrel wall, the constant barrel wall temperature may interfere with the actual measurement of the melt temperature. Essentially, at lower temperature difference (i.e. shorter time), the experimentally measured temperatures will be lower than the actual melt temperature. Overall T4 increases 1.8K for PE and 2.5K for PS while T5 increases 1K for PE and 1.5K for PS. Again, the high viscosity of PS creates higher viscous dissipation and a higher temperature increase.
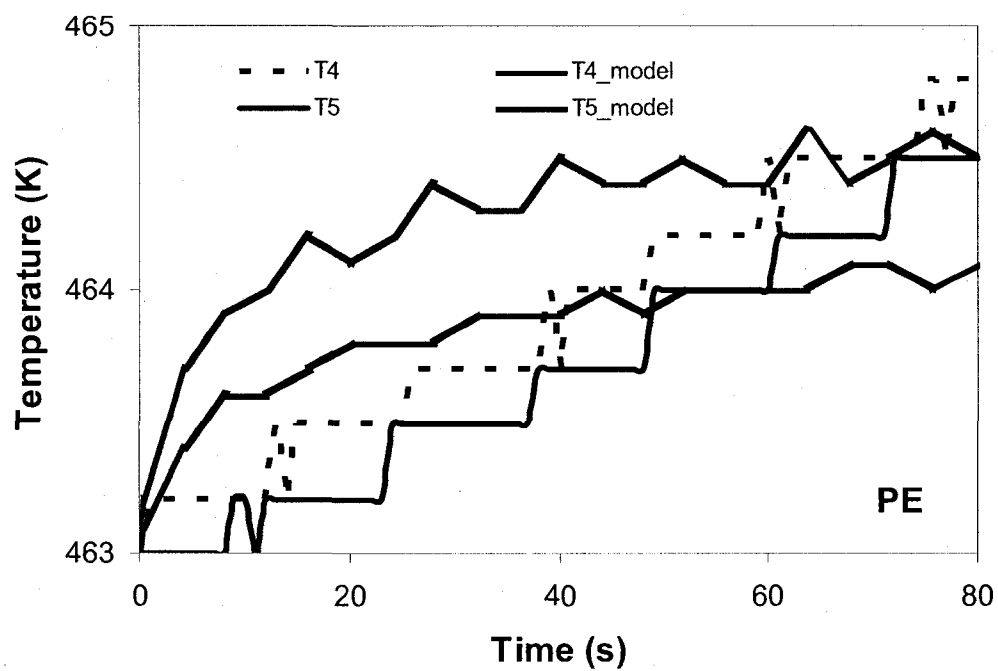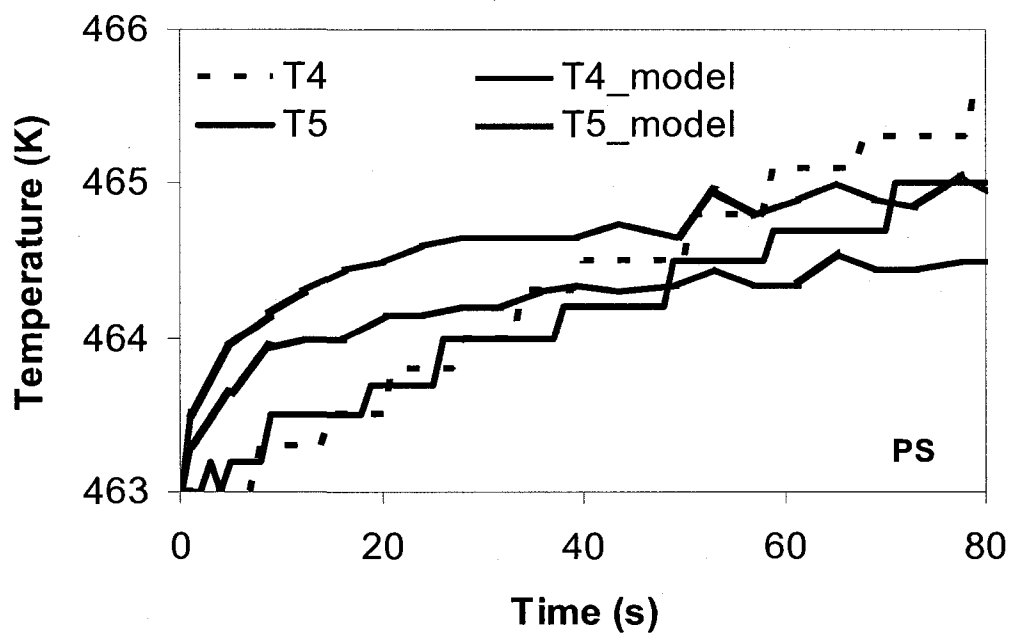
Figure 2.7: The temperature development of thermocouples T4 and T5, located in the left chamber and the right chamber: (a) PE; (b) PS.

Figure 2.8 shows the x-y cross-section surface-averaged temperature obtained from simulations along the axial direction at different times for PE and PS. The axial distance was normalized as the axial distance divided by the mixer length giving a range from 0 to 1. The surface-averaged temperature was obtained by integrating the point temperature over the cross-sectional surface and dividing it by the cross-sectional area. Initially, the temperature in the flow domain is very close to the starting temperature and the average temperature profile is quite flat. Due to the heat generated by viscous dissipation, the temperature increases and a symmetric temperature profile is developed. The middle cross-section surface (i.e. z=0.5) has the highest temperature at any time. The curves of average temperature versus axial distance increase or decrease sharply at locations close to the back and front walls respectively and become flat around the middle of the mixer. Because of its higher viscosity, the PS melt has a higher average temperature than the PE melt over the whole transient process.

(a)

(b)

(c)
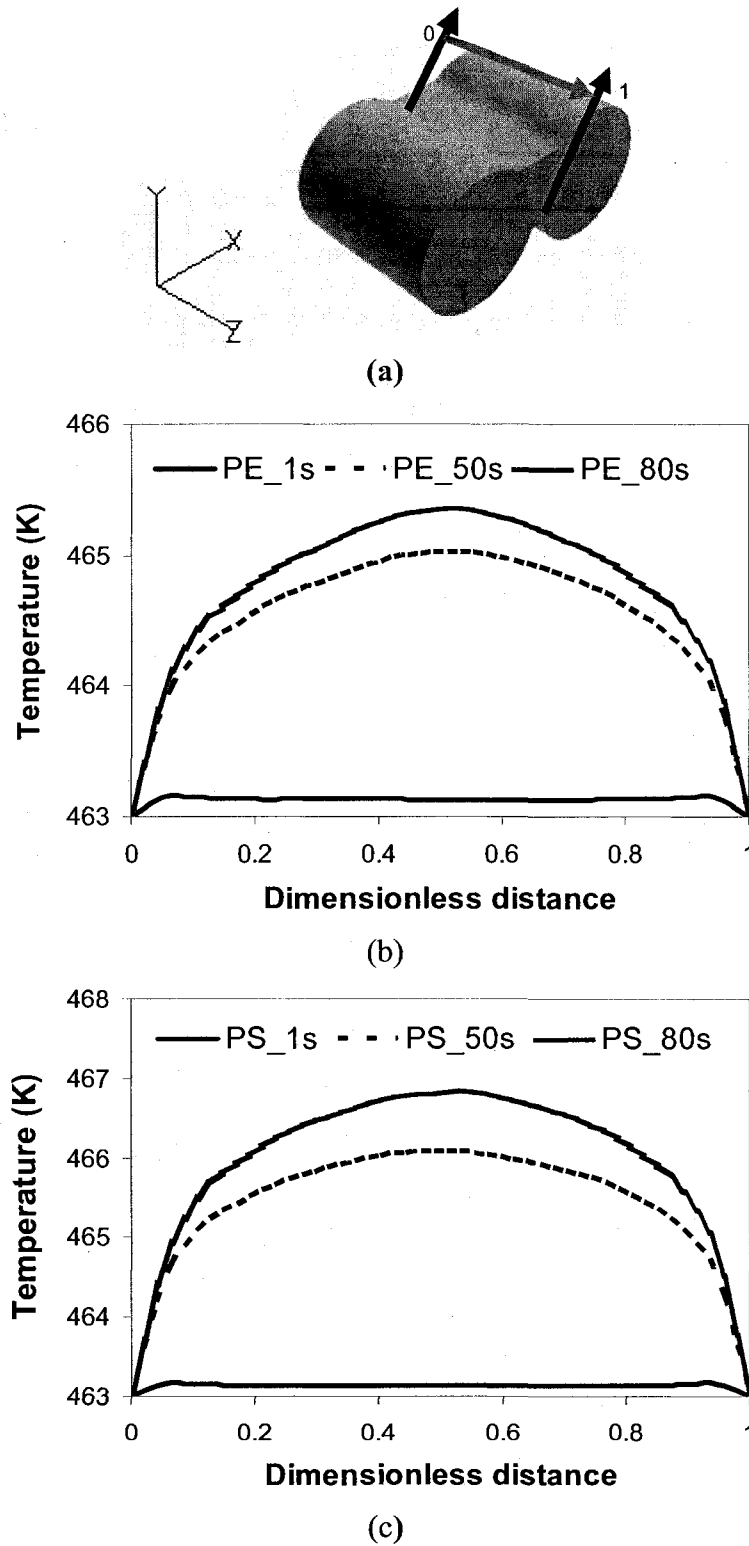
Figure 2.8: Surface-averaged temperature changes: (a) normalized axial distance of the entire mixer, (b) for PE; (c) for PS. The origin (x, y, z) is (0, 0,0). Note different scales on (b) and (c).

2.4.3 Additional simulation results

More detailed information about the temperature field and the flow field can be obtained from the simulation results to give us a better understanding of what happens inside the mixer during the simulated transient process.

2.4.3.1 Heat flux

Figure 2.9 shows the heat flux at the mixer wall as a function of circumferential distance at three different times for PE and PS respectively. The heat flux q'' is calculated by the following equation:

$$q'' = \left\| -k\nabla T_{T=T_w} \right\| \tag{2.15}$$

The heat flux direction is perpendicular to the wall and flows out of the mixer as indicated by the black arrows. The starting point in the plot is shown as a dot on the top of the mixer in Figure 2.9a and the heat flux is plotted in the direction indicated by the white arrow tangent to the circumference from the right chamber to the left chamber and back. For both materials, the heat flux across the wall increases with time and finally reaches a thermal steady state. From 50s to 80s, the heat flux increase changes very little, although the temperature of the polymer melt continues to increase and reaches a thermal steady state as shown in Figure 2.6. At the thermal steady state, the average heat flux for PE is approximately 700W/m^2 in the right chamber and 1050W/m^2 in the left chamber. For PS, the average heat flux is approximately 900W/m^2 in right chamber and 1300W/m^2 in left chamber. The heat flux ratio of the right chamber versus left chamber is about 2/3: the same as the rotation speed ratio of the right rotor versus left rotor.
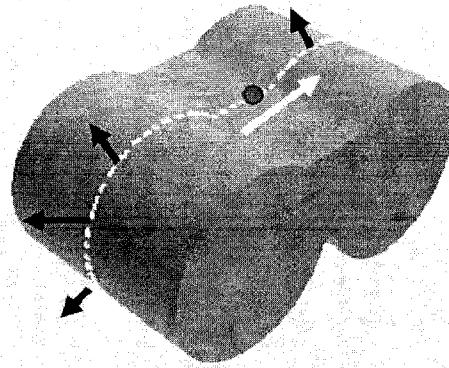
(a)
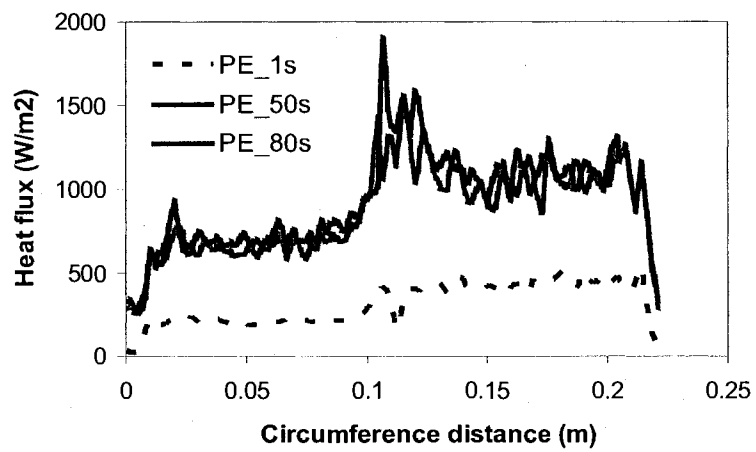
(b)
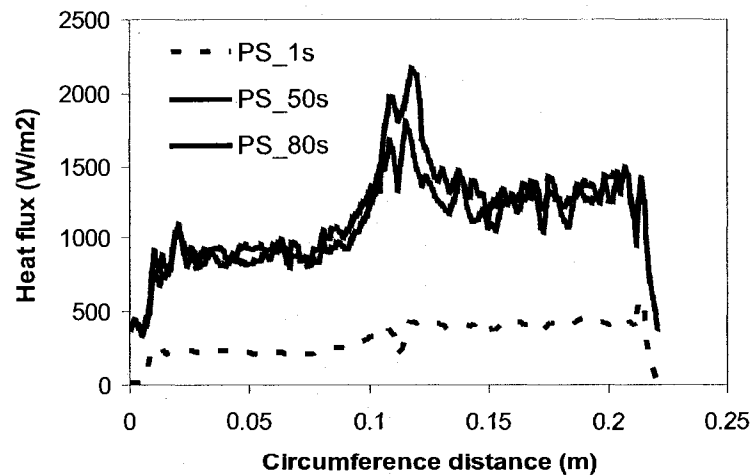
(c)

Figure 2.9: Heat flux across wall around the circumference at the mid-depth for different times: (a) Location where the heat flux is calculated; (b) heat flux for PE; (c) heat flux for PS.

2.4.3.2 Temperature distribution at a cross-section

Figure 2.10 shows the steady-state temperature distribution at the axial middle cross-section for both PE and PS from a starting temperature at 463K. Because of a higher rate of viscous heating near the wall, the temperature at the clearances is as high as 466.6 K for PE and 469.7K for PS, while the average temperature in the mixer increases to 464.5K for PE and 465.5K for PS. It is found that the temperature in the clearance area is about 1K higher than the temperature in the area between two rotors, and that the temperature in the left rotor side is about 0.5K-1K higher than the temperature in the right side.
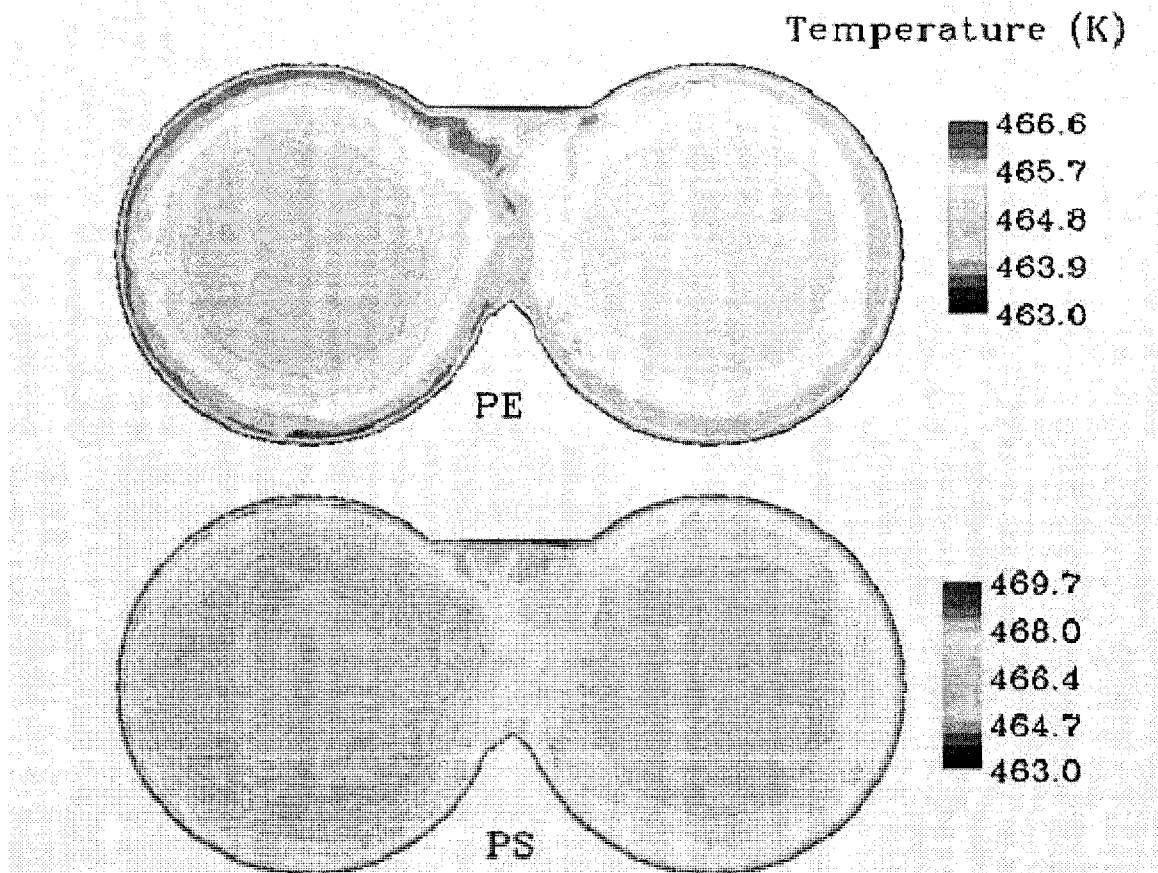
Figure 2.10: The steady-state temperature distribution at the axial middle cross-section.

2.4.3.3 Velocity profile

Due to the high viscosities of polymer melts, laminar flow is the dominant flow in polymer mixing equipment. Various laminar flow patterns such as shearing, squeezing or elongational flows play a very important role in achieving uniformity of polymer blends and nanocomposites, and in dispersing minor components throughout the matrix [31]. As shown in Figure 2.11, the velocity profiles are very similar for PE and PS. The velocity profile consists of two parts: high shear flow in the region between rotor tips and wall; and elongational flow in the middle region between the two rotors. When viewing the velocity profiles in Figure 2.11, one should note that the rotational speed ratio of the left rotor to the right rotor is 3 to 2 in the internal batch mixer; the magnitude of the velocity is scaled by the arrow length; and the color on the legend bar also indicates the magnitude of the velocity vector. The maximum velocity of 0.1 m/s occurs on the tip of the left rotor where the gap is the smallest. While a small amount of extensional flow exists in the middle area between two rotors, shear flow dominates in the narrow region between the rotor tip and chamber wall. As expected, the largest velocity always occurs near the rotor tips and therefore the polymer melt is squeezed in these areas. In the gaps between the two rotors, the materials from left and right chambers meet in the upper area and then split again in the lower part. The velocity profiles show that shear flow dominates in the gap between the rotors and barrel wall, and all other flow types such as folding, elongation and splitting occurs in the middle region between the two rotors.
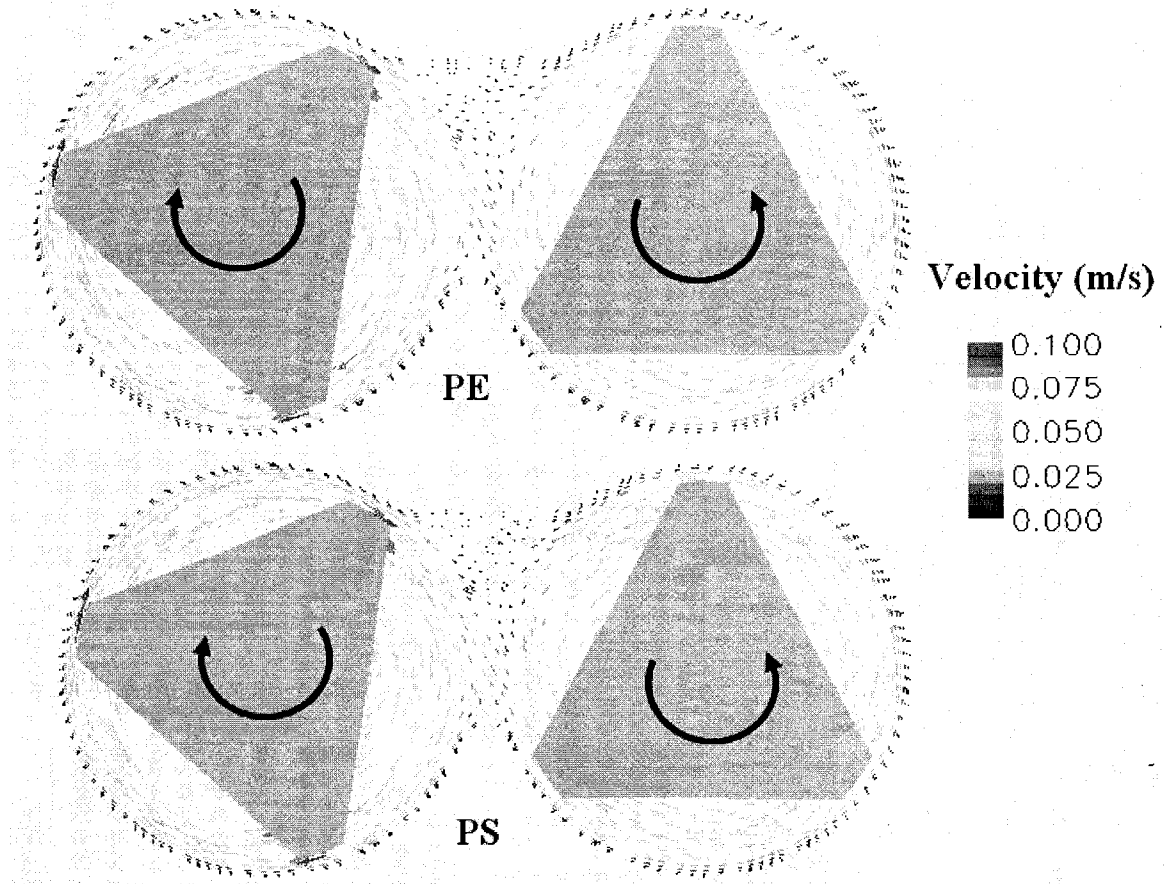
Figure 2. 11: Steady- state velocity profiles at the axial middle cross-section.

Since the two rotors have different configurations along the axial direction, the velocity profiles at different axial cross-sections are different. The centers of three axial cross-sections at the dimensionless axial distances 0.36 (C036), 0.50 (C050), and 0.86(C086) are plotted in Figure 2.12a, b, and c. Figure 2.12a shows the section C036 at the back of the mixer. The tip of the right rotor is slightly higher than that of left rotor and hence the flow from the right chamber is folded and then joins the flow from left. Since the left rotor tip pushes the materials into the right chamber, most of the materials in the gap in the middle of the mixer go to right chamber. In Figure 2.12b, the flow pattern is in the opposite direction,
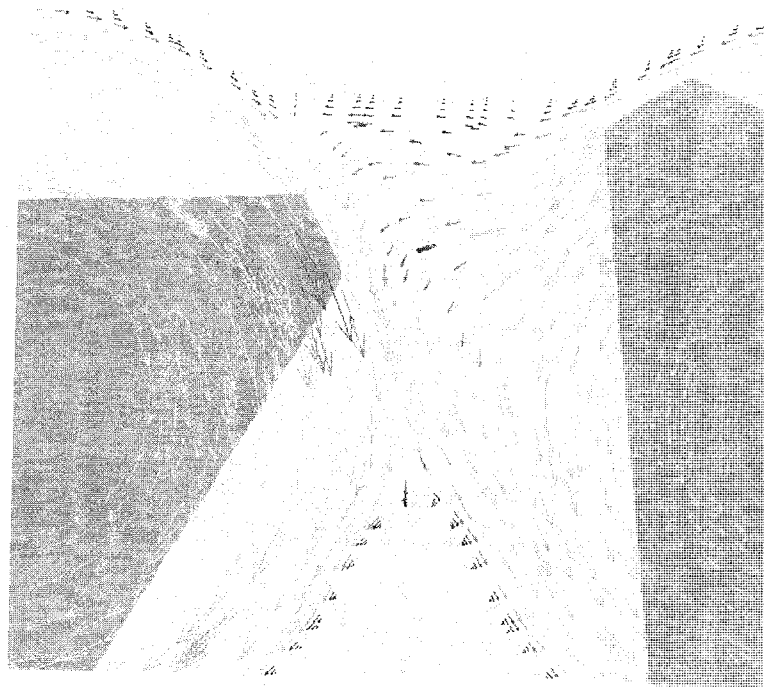
(a)
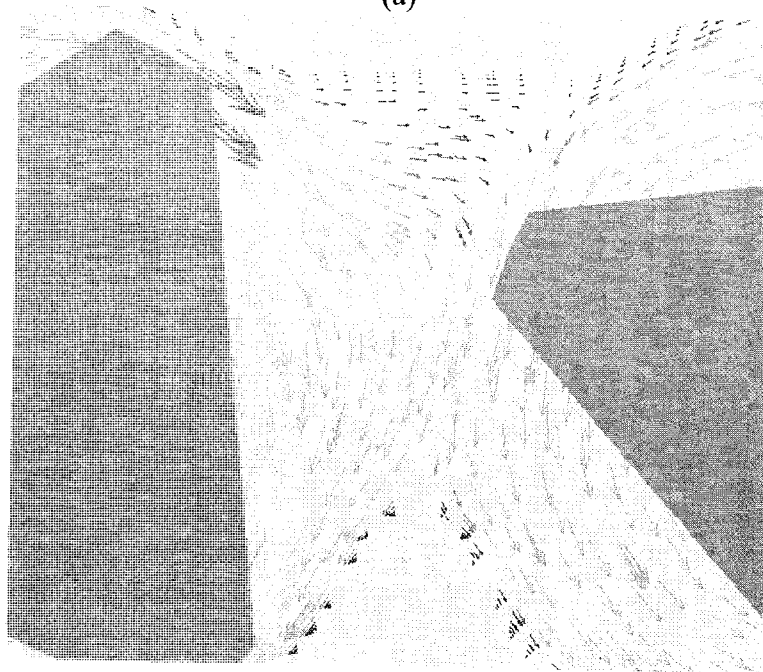
(b)

Figure 2.12: The radial velocity profiles at three typical cross sections (scaled by the same legend bar shown in Figure 2.11): (a) the enlarged center of C036; (b) the enlarged center of C050; (c) the enlarged center of C086. (To be continued).

(c)

Figure 2.12 (Continued)

but the extent of folding of the flow from the left chamber at this location is less than that from the right rotor in C036. When the tips of the two rotors are at the same level as in Figure 2.12c, the flows from the two chambers join together and then split almost equally in two directions. There is not much folding in this configuration.

Figure 2.13a-f shows how the flow field changes between two rotors at cross-section C050 during one rotation of the left rotor ($\theta=0°$ to $\theta=360°$), which takes 1.2s at 50rpm. Due to the different rotational speeds of the two rotors, different configurations occur creating various flow patterns that promote the dispersion and distribution of the minor component. Depending on the positions of the two tips, folding may occur in the upper, center, and/or bottom parts of the middle section of the mixer, or no folding may occur at all. Initially in Figure 2.13a, the

materials mix and mostly flow into the right chamber and folding is seen near the bottom of the mixer. After the left rotor turns 60 degrees (Figure 2.13b), the tips of two rotors are almost in the same position and there is no folding at all. At 120 degrees (Figure 2.13c), the tips of both rotors are located in the central area with the right rotor located a little bit higher. Here, the materials are squeezed and elongated to the maximum extent. In the next two positions (Figure 2.13d and 2.13e), the flow is folded near the bottom of the mixer and flows to the chamber opposite to the tip that is located lower in each case. When left rotor turns 300 degrees (Figure 2.13f), both tips appear in the upper part of the mixer and the folding occurs mainly near the top of the mixer. Although the repeating period is
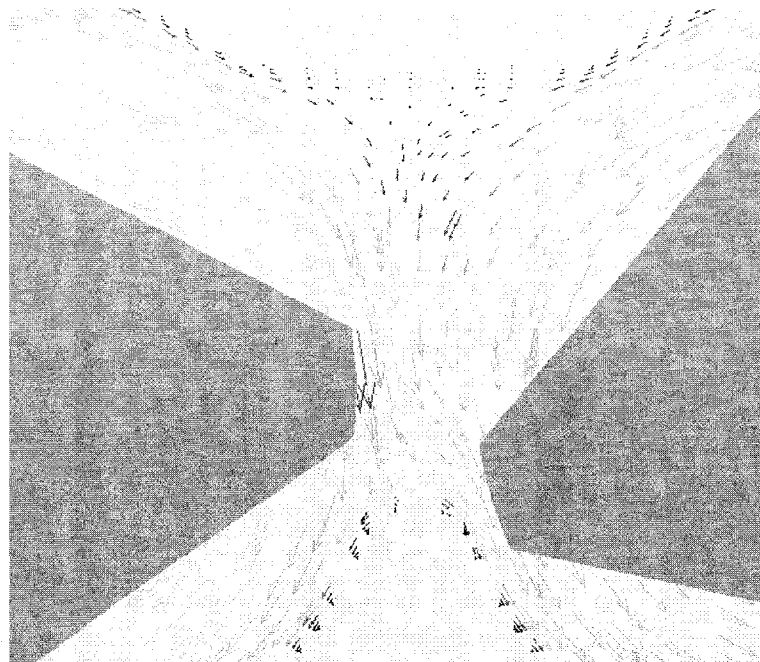
(a)

Figure 2.13: Transient velocity profiles of internal batch mixer at cross section C050 (scaled by the same legend bar shown in Figure 2.11). a-f shows velocity change at the center of MB during one turn of the left rotor: (a) θ=0; (b) θ=60°; (c) θ=120°; (d) θ=180°; (e) θ=240°; (f) θ=300°. (To be continued).
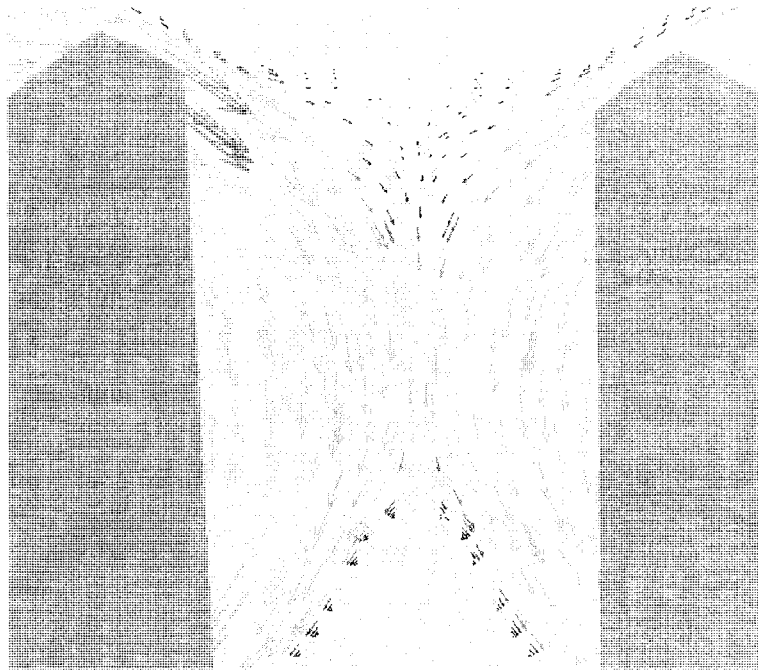
(b)
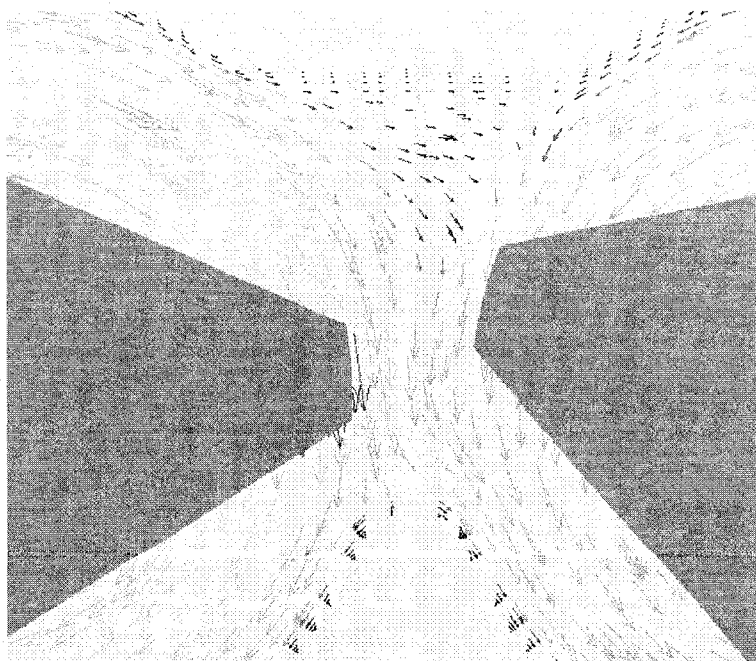
(c)

Figure 2.13 (Continued)
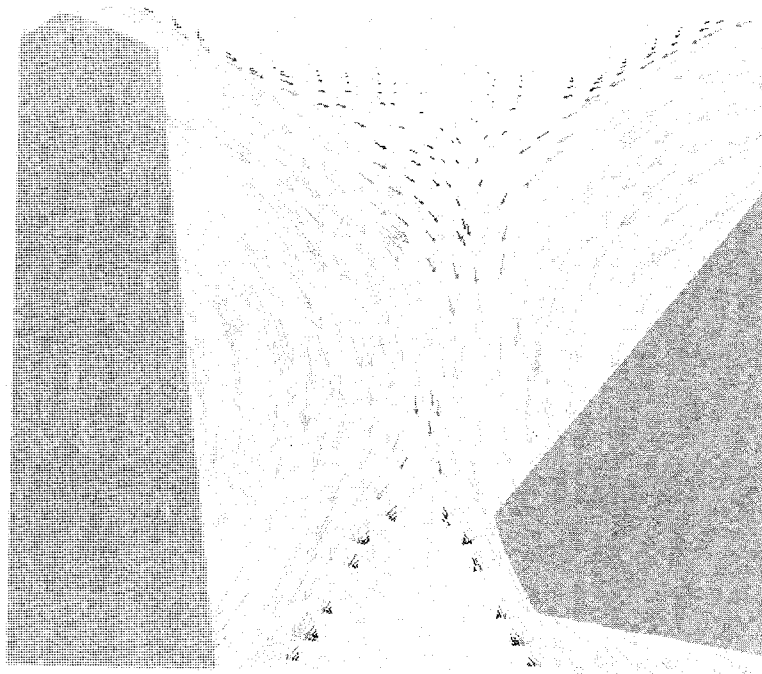
(d)
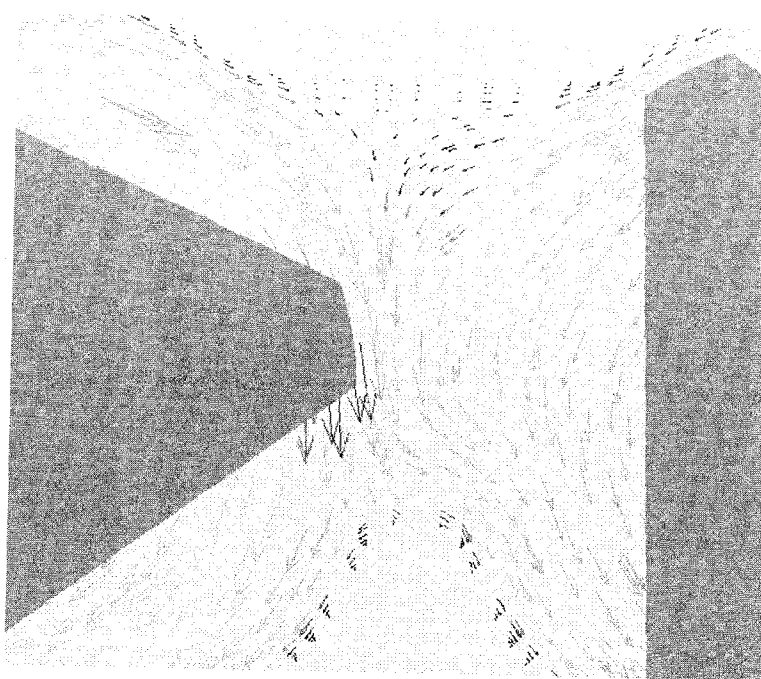
(e)

Figure 2.13 (Continued)
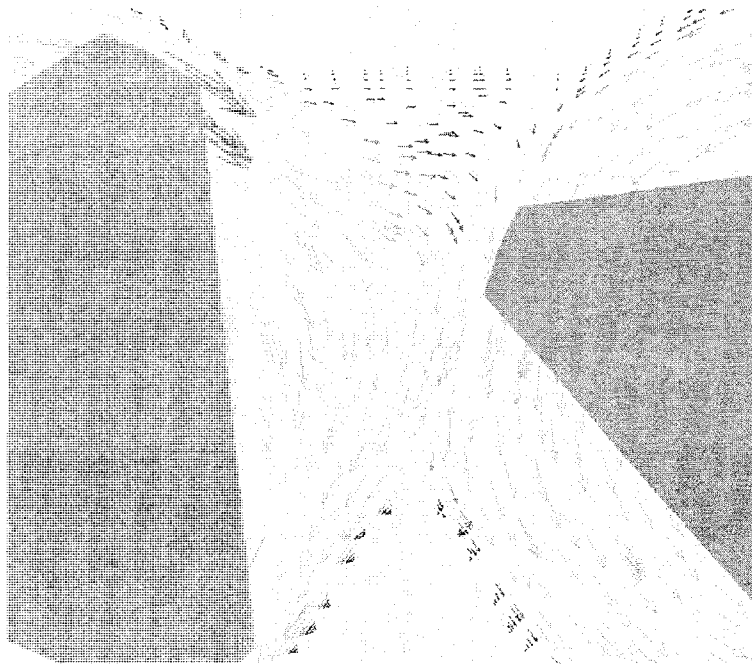
(f)

Figure 2.13 (Continued)

3.6s at a rotational speed of 50rpm, the positions of the tips of both rotors in this particular cross-section return to their original locations every 1.2s because there are three identical tips per rotor.

2.5 Summary

For both the PE and the PS melt, the mechanical power consumed was calculated from the experimental torque and has a good match with the value obtained from a 3-D CFD simulation. The predicted heat transfer coefficient from simulation increases with time. The observed wall temperature is about 1-2K higher than the pre-set value of 463K. Because of the increase in wall temperature, the temperature of the PS melt is higher than the predicted value. Natural air convection is sufficient to keep the mixer wall constant for the low viscosity material, but for high viscosity material, forced air convection is necessary to remove the heat produced by viscous heating so that a constant wall temperature can be maintained.

Simulation results give us a detailed picture of the temperature distribution and flow progress inside the mixers. The higher rotational speed of the left rotor results in a higher temperature and higher heat flux in the left chamber. The simulation results also verified that multiple flow modes co-exist in the mixer.

2.6 Reference

1. Bousimina M., Ait-Kadi A., and Faisant J. B., "Determination of shear rate and viscosity from batch mixer data", Journal of Rheology, 43 (2), 415, 1999.

2. Yamaguchi, M., Wagner, M.H., "Impact of processing history on rheological properties for branched polypropylene", Polymer, 47 (10), 3629, 2006.

3. Campanelli, J.R., Gurer, C., Rose, T.L., Varner, J.E., "Dispersion, temperature and torque models for an internal mixer", Polymer Engineering and Science, 44 (7), 1247, 2004.

4. Yamaguchi, M., Todd, D.B. , Gogos, C.G., "Rheological properties of LDPE processed by conventional processing machines", Advances in Polymer Technology, 22 (3), 179, 2003.

5. Sundararaj, U., Macosko, C.W., "Drop breakup and coalescence in polymer blends: The effects of concentration and compatibilization", Macromolecules, 28 (8), 2647, 1995.

6. Manas-Zloczower, I., "Studies of mixing efficiency in batch and continuous mixers", Rubber Chemistry and Technology, 67 (3), 504, 1994.

7. Palmgren H., "Processing conditions in the batch-operated internal mixer", Rubber Chemistry and Technology, 48, 462, 1974.

8. Li H. and Hu G., " A two-zone melting model for polymer blend in a batch mixer", Polymer Engineering and Science, 41(5), 763, 2001.

9. Soltani, S., Sourki, F.A., "Effect of carbon black type on viscous heating, heat build-up, and relaxation behavior of SBR compounds", Iranian Polymer Journal (English Edition), 14 (8), 745, 2005.

10. Herrera-Velarde J. R., Zenit R., Mena B., "Measurement of the temperature rise in non-Newtonian oscillatory pipe flows", Journal of Non-Newtonian Fluid Mechanics, 109, 157, 2003.

11. Wei D. W., Luo H. B., "Finite element solutions of heat transfer in molten polymer flow in tubes with viscous dissipation", International Journal of Heat and Mass Transfer, 46, 3097, 2003.

12. Goodrich J. E., Porter R. S., "A rheological interpretation of torque-rheometer data", Polymer Engineering and Science, 7, 45, 1967.

13. Blyler, L.L., Daane, J.H., "An analysis of Brabender torque rheometer data", Polymer Engineering and Science, 7 (3), 178, 1967.

14. Marquez, A., Quijano, J., Gaulin, M., "A calibration technique to evaluate the power-law parameters of polymer melts using a torque-rheometer", Polymer Engineering and Science, 36 (20), 2556, 1996.

15. Mallette, J.G., Soberanis, R.R., "Evaluation of rheological properties of non-newtonian fluids in internal mixers: An alternative method based on the power law model", Polymer Engineering and Science, 38 (9), 1436, 1998.

16. Bousmina M., Ait-Kadi A., Faisant J. B., "Determination of shear rate and viscosity from batch mixer data", Journal of Rheology, 43(2), 415, 1999.

17. Ait-Kadi A., Marchal P., Choplin L., Chrissemant A., Bousmina M., "Quantitative analysis of mixer-type rheometers using the coquette analogy", The Canadian Journal of Chemical Engineering, 80, 1166, 2002.

18. Clarke, J., Petera, J., "Modeling dispersive mixing of rubber compounds", Rubber Chemistry and Technology, 72 (5), 807, 1999.

19. Hutchinson, B.C.; Rios, A.C.; Osswald, T.A., "Modeling the distributive mixing in an internal batch mixer". International Polymer Processing, 14 (4), 315, 1999.

20. Nassehi, V., Ghoreishy, MHR, "Finite element analysis of mixing in partially filled twin blade internal mixers", International Polymer Processing, 13 (3), 231, 1998.

21. Ghoreishy, MHR; Nassehi, V., "Modeling the transient flow of rubber compounds in the dispersive section of an internal mixer with slip-stick boundary conditions", Advances in Polymer Technology, 16 (1), 45, 1997.

22. Valera, T.S., Demarquette, N.R., Toffoli, S.M., "Effect of filling factor on the determination of shear rate and viscosity from batch mixer", Journal of Polymer Engineering, 24 (4), 409, 2004.

23. Jongen T., "Characterization of batch mixers using numerical flow simulations", AIChE Journal, 46, 2140, 2000.

24. Gramann P. J., Mätzig J. C., Osswald T. A., "Simulating the non-isothermal mixing of polymer blend using the boundary element method", Journal of Reinforced Plastics and Composites, 12,787,1993.

25. Malkin, A. Y., Baranov A. V., Dakhin O. K., "Non-isothermal dispersive flow of a rubber mixture inside an internal rotor mixer", International Polymer Processing, 10 (2), 99, 1995.

26. Nassehi V., Salemi R., "Finite-element modeling of non-isothermal viscometric flows in rubber mixing", International Polymer Processing, 9 (3), 199, 1994.

27. Kim J. K., White J. L., "Non-newtonian and nonisothermal modeling of 3-D-flow in an internal mixer", International Polymer Processing, 6 (2), 103, 1991.

28. Palmgren, H, "Processing conditions in the batch operated internal mixer", Rubber Chemistry Technology, 48, 462, 1975.

29. Nakajima N., "Mechanism of mixing in internal mixer and energy-based modeling", Polymer International, 41, 23, 1996.

30. Churchill S. W., and Chu H. H. S., "Correlating equations for laminar and turbulent free convection from a vertical plate", International Journal of Heat and Mass Transfer, 18, 1323, 1975.

31. Gogos C. G., Tadmor Z., Kalyson D. M., Hold P., "Polymer processing: an overview", Chemical Engineering Progress, 6, 33, 1987.

CHAPTER 3

EVALUATION OF A NEW MINIATURE
MIXER FOR POLYMER MIXING

3.1 Introduction

With the increasing need to mix small amounts of material, miniature mixers with capacities of milliliters are needed to reduce the testing cost to screen new materials while still providing comparable mixing for polymer compounds. Generally newly designed small mixers should produce complex flow modes such as those generated in internal batch mixers and twin-screw extruders to provide both distributive and dispersive mixing for polymer blending and compounding. Though it would primarily be used in laboratories, the small mixer also should have a user-friendly interface and be easily operated and maintained.

One of the earliest miniature mixers with 1-10 gram capacities was developed by Maxwell and distributed by Custom Scientific Instruments Inc. as the MiniMax Molder [1]. The MiniMax Molder (shown in Figure 1.2a) primarily consists of a cylindrical rotor rotating in a cylindrical cup. Since only shear flow is generated in this parallel-plate mixer, the MiniMax Molder cannot provide enough distributive and dispersive mixing for polymer blending [2]. The mixing ability of the MiniMax Molder can be improved by periodically lifting the rotor and introducing a Teflon disk and steel balls into the mixer cup [2-5]. Another small scale mixer was developed by Scott et al [6], known as the re-circulating screw mixer (RSM). Instead of a cylindrical rotor, the screw of the RSM (shown

in 1.2b) is a small flighted screw with an axial hole drilled through the end of the screw to a location near the feed point on the screw. The mixer is just like a single screw extruder, however, the hole re-circulates the flow internally making the RSM a batch mixer. It was proven that the RSM accomplishes intensive mixing that is comparable to the mixing provided by a standard internal batch mixer for some polymer blend and composites systems [6]. Recently a new miniature mixer called the "Alberta Polymer Asymmetric Minimixer" has been developed by our research group [7] and has been proved to be an efficient mixer for polymer blends and nanocomposites compounding. There are also several miniature twin-screw extruders available on the market with capacities ranging from 5-15 cc. These are the DACA or DSM Micro-compounder (5cc and 15cc, shown in Figure 1.2c) [8], and HAAKE MiniLab II Micro Compounder (7cc) [9]. All three machines have a similar design except that the screws are horizontal of the HAAKE micro-compounder while they are vertical for the other two machines.

As introduced earlier in Chapter 1 and Chapter 2, the internal batch mixer is one of the most successful mixers used for laboratory use and screen testing. The large-scale internal batch mixer has been widely used in the rubber industry for incorporating carbon black into rubbers. Much research to date [10-12] and Chapter 2 of this thesis have shown that the internal batch mixer produces the complex flow modes and intensive mixing necessary for compounding the majority of polymer blends and composites. Within a mixing time of 10min, the

internal batch mixer produces similar mixing effects to the twin-screw extruder [13].

In this chapter, a miniature internal batch mixer (MBM, 3 mL), a scaled-down version of the standard internal batch mixer (BM, 69 mL), was used to provide compounding at the 2-3g scale. While sizing down equipment usually makes process control easier, scaling-up has always been a critical issue for polymer processing equipment especially because of the high viscosities of polymer. When we scale-up using a linear scale factor, the larger mixer under the same processing conditions tends to have a higher temperature due to viscous dissipation because the volume of the mixer, and thus the heat generated increases cubically while the cooling area increases only quadratically with the scale factor [14]. To achieve the same amount of mixing for a given material in two internal batch mixers of different size, it is recommended that the shear rate and the unit input energy be kept the same so that the batch temperatures follow the same path through the mixing cycles [15]. However, the above parameters are very hard to estimate for a specific mixing process because they are related to the processing conditions, geometric structure and the material properties. Some previous work tried to relate shear rate to input energy for Newtonian and Power-law flow using simplified 2-D geometries [16-19], but it is impossible to show the batch temperature path through the mixing cycles by analytical methods.

As an alternative method to experimental investigation, a couple of simulation studies have been done to investigate the effect of scaling-up the continuous mixers. Wang et al. [20] used a particle tracking technique based on the solved

flow field to calculate the temporal distributions of several mixing indexes and proposed the calculation of average agglomerate and agglomerate size distribution as a new dispersive mixing criterion for scale-up of mixing equipment. Dhanadekharan et al [21] performed a 3-D non-isothermal numerical simulation for single-screw extruders and applied the residence time distribution and specific mechanical energy as scale-up parameters. One of the advantages of numerical simulations is that various flow and heat transfer parameters can be easily obtained without simplifying the mixer geometry and non-Newtonian behaviors of polymer melts can also be incorporated into the model.

In the present study, the flow and heat transfer in the 3 mL MBM were simulated using a generalized Newtonian model and were compared with the flow and heat transfer in the 69 mL internal batch mixer presented in Chapter 2. The simulation results for melt temperature were compared to experimental data from the MBM at the same conditions. Under the same processing conditions used in Chapter 2, we verified that, the flow parameters (shear rate, shear stress, mixing index); power required per unit volume; and the passes of particle over the rotor tip region, stay unchanged for a linear sizing factor of 2.83 [15]. By numerical simulation, we also visualized the change of temperature and temperature distribution caused by viscous dissipation. Finally the 3 mL mixer and 69 mL mixer were used to prepare polymer blends and nanocomposites. The morphologies of the resulting blends and nanocomposites from both mixers were compared.

3.2 Design of the MBM

The miniature mixer shown in Figure 3.1 was built to have a volume of approximately 3 mL and is abbreviated as MBM. Both the mixing chamber and the rotors are scaled down from the 69 mL BM with a linear scale factor of 0.36. The detailed specifications of the two mixers are given in Table 3.1. Due to the slightly different scaling ratio of the screw tip radius and barrel radius, the tip clearance of the MBM is 0.5mm. As a result, the ratio of the screw tip radius over the tip clearance (r/h) for the MBM is 13, which is slightly higher than that of the BM. Under the same rotational speed and batch temperature, the higher r/h ratio will result in a higher shear rate and shear stress over the rotor tip region. Since the MBM is primarily used for incorporating nano filler into polymers, a higher shear stress over the rotor tip may be favorable to overcome the strong cohesive forces within nano-filler agglomerates.

Table 3.1: Dimensions of 3 mL and 69 mL mixers.

	3 mL MBM	69 mL BM	Scale ratio
Volume (mL)	3	69	$(0.352)^3$
Barrel radius R (mm)	7	19.75	0.354
Total barrel width W (mm)	29	81	0.358
Total channel depth D (mm)	16.5	47	0.351
Screw tip radius r (mm)	6.5	18	0.361
Tip clearance h (mm)	0.5	1.75	0.286
r/h	13	10.3	
Length of the vertical plate L (mm) outside barrel dimension	100	125	0.8
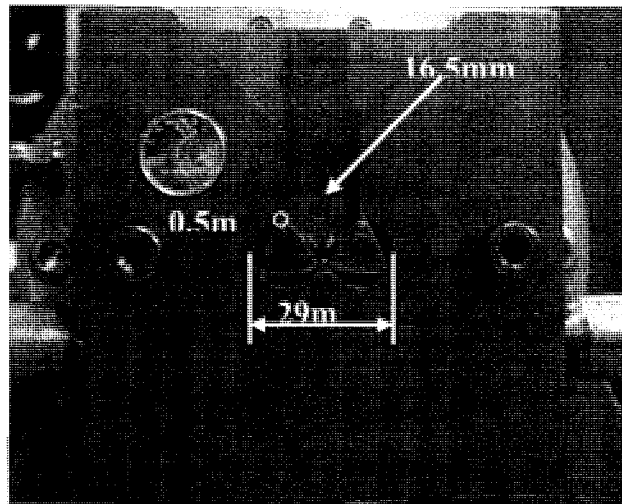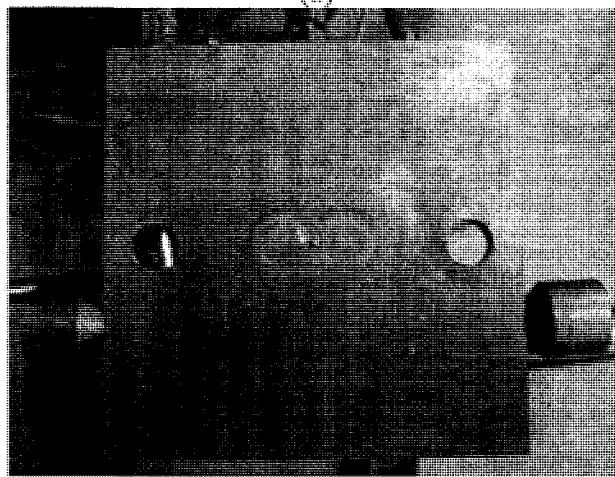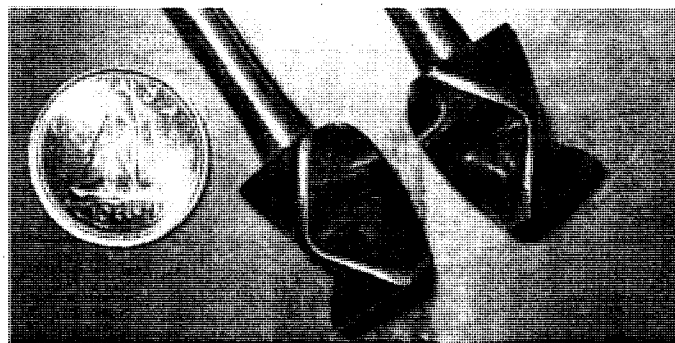
Figure 3.1: **Photograph and dimensions of the 3 mL MBM: (a) the back and middle sections of 3 mL MBM with roller blades installed; (b) Front section of MBM; (c) Rotors of the 3 mL MBM. In (a) and (b), a Canadian 10-cent piece (1.8mm diameter) is shown for comparison.**

The MBM is driven by a Haake system 90 torque rheometer and is attached to the back section of a Haake rheomix 600 batch mixer (69 mL BM). The speed and the barrel temperature are controlled by the same system as the 69 mL BM and have the same maximum limits. Unlike the 69 mL BM, the MBM does not have a built-in cooling system and is cooled down by the surrounding air, so a relatively large surrounding wall is built for the MBM to increase the mixer interface with surrounding air and improve the heat transfer efficiency. As shown in Table 3.1, the length of the vertical plate is 100mm for the MBM and 125mm for the BM. The scaling ratio of the length for the outside dimension of the barrel is 0.8 and is much larger than the scaling ratio of the dimensions as 0.36.

As shown in Figure 3.1b, a thermocouple was mounted in the middle of the MBM's front section and was inserted 2mm into the polymer melts to record the melt temperature. To investigate the temperature distribution inside the BM, we modified the 69 mL BM (see Chapter 2) to have five thermocouples protruding into the mixer chamber. It is impossible to do the same for the MBM because of the extremely small gap between rotors and wall, so we only recorded melt temperature at one point in MBM and studied the temperature distribution inside the mixer by simulation.

Another design modification is the feeding area. We used the same size of raw material when feeding the MBM as we feed BM. Because of the small surface of MBM, there is a relatively large inlet area to assist feeding. The comparison in Figure 3.2 shows that the feeding port of MBM has a relatively larger flat area on its top side, and after feeding the port to the mixer is sealed by a
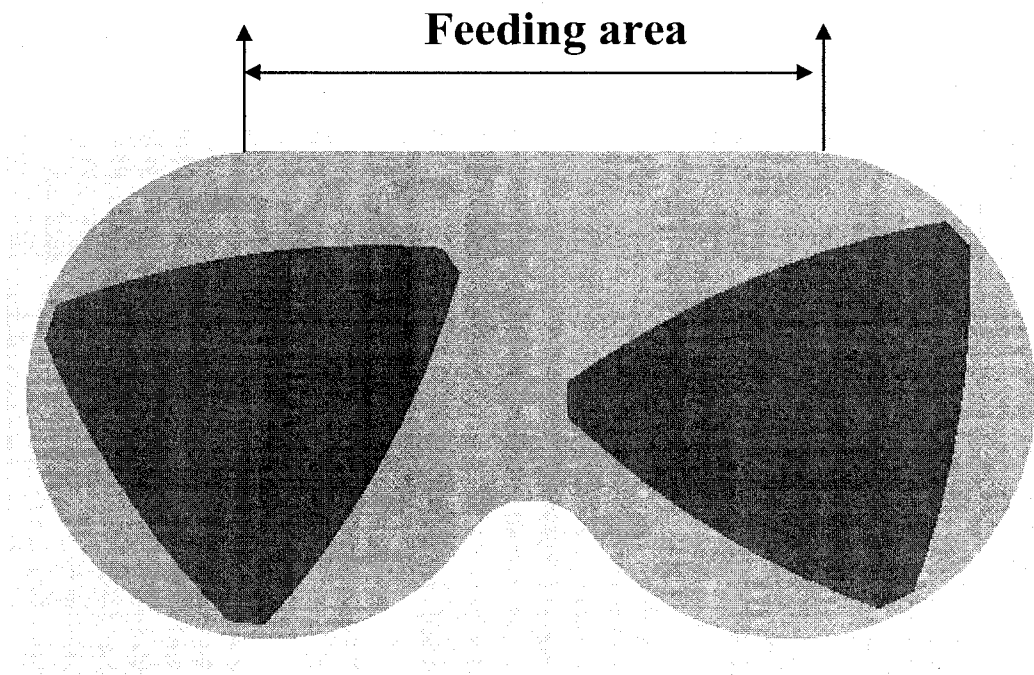
(a)
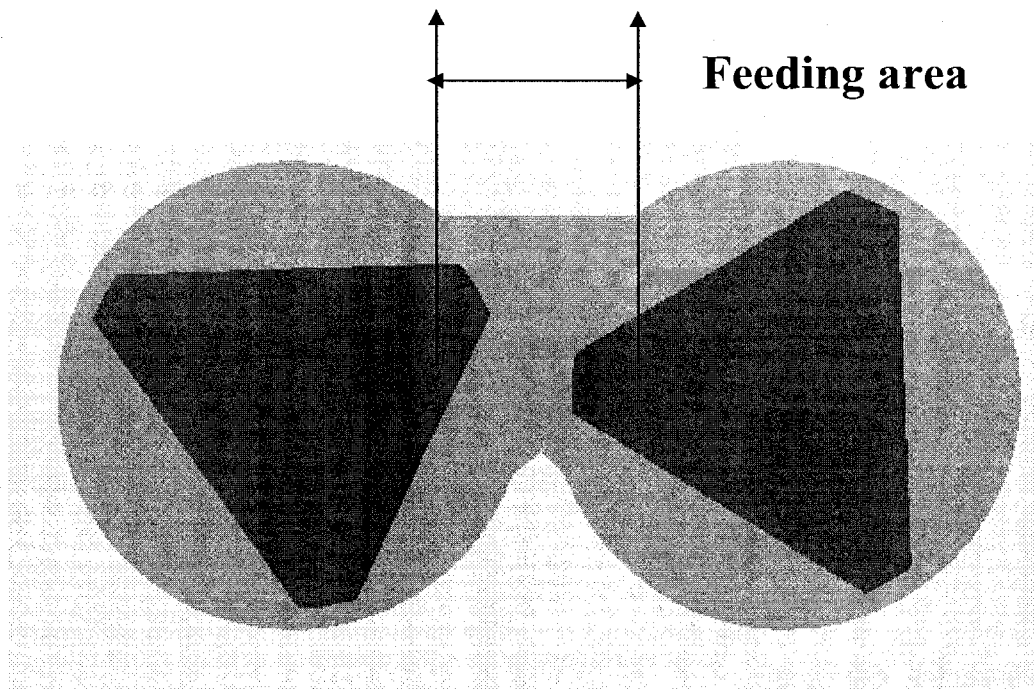
(b)

Figure 3.2: Cross-sections of feeding areas of: (a) MBM; (b) BM.

rectangle-shaped cap. The BM, by contrast, has a smaller feeding area relative to its size and the top of the mixer is not flat. The velocity of the flow under the flat area in MBM is relatively small because the polymer melt in this area is far away from the rotors. So the shear rate and shear stress in this region are expected to be close to zero. Using the same processing condition and same material, MBM may have a relatively smaller average shear rate and shear stress because of the larger proportion of low shear regions versus the total sample volume.

3.3 Computation Method

Gambit 1.3 was used to generate the meshes of MBM as shown in Figure 3.3. The mesh is composed primarily of tetrahedral mesh elements with small amount of hexahedral, pyramidal, and wedge elements where appropriate. The mesh size is 1mm and the boundary layer near the barrel wall has much finer meshes. The total number of mesh elements in the MBM is 61,900. With two irregular rotating rotors, the mesh superposition method is used for MBM to avoid re-meshing that is normally used during a transient simulation.
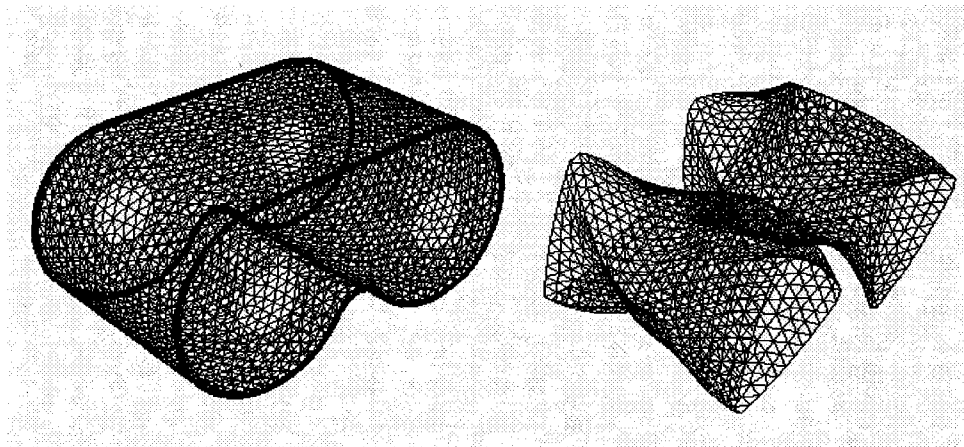
Figure 3.3: Mesh and simulation geometry of MBM.

The governing equations of continuity, motion and energy as shown in Equation 2.3-2.6 in Chapter 2 were solved numerically using the finite element code, Polyflow3.9 from Fluent Inc. The thermal boundary conditions (TBC) and flow boundary conditions (FBC) are shown in Table 3.2.

Table 3.2: Boundary conditions used in the simulations.

	FBC	TBC
Left rotor	-5.236 s^{-1}	insulated
Right rotor	3.4906 s^{-1}	insulated
Barrel wall	$V_n = 0$	
	$V_s = 0$	T=493 K

The combined Approximate Arrhenius law and Carreau-Yasuda law is used to characterize the viscosity change of PS versus shear rate and temperature:

$$\eta = [\exp(-0.006466(T - 463))] \bullet 8357.8\left[1 + (0.3347\dot{\gamma})^{0.6686}\right]^{\frac{0.3215-1}{0.6686}} \qquad (3.1)$$

Other properties of PS are summarized in Table 3.3. It should be noted that the PS used in this chapter is the same as the PS used in Chapter 2. The rotor properties were assumed to be the same as those of the stainless steel AISI 316.

Table 3.3: Properties of polymer and rotor.

	Density at 200 °C (kg/m^3)	Thermal capacity (J/kg/K)	Thermal conductivity (W/m/K)	Viscosity (Pa·s)
PS	882	2098	0.1231	Eq.3.1
Rotor	8000	400	15	Not applicable

The simulations were performed on an IBM RS/6000 Power 4 workstation with 8 GB memory. It took an average of three weeks to complete each run.

3.4 Experimental

3.4.1 Materials

The polymers and nano-filler used for this study are described in Table 3.4. Samples of polymer blends were prepared to evaluate the mixing performance of the MBM. The non-reactive and reactive polymer blend we chose are Polystyrene/Polyamide (PS/PA) and 5% Maleic anhydrate modified Polystyrene/Polyamide (PSMA/PA) respectively, each with an 80/20 weight ratio.

The nano-clay we used is Cloisite20A (C20A) supplied by Southern Clay Co. It is a natural montmorillonite modified with dimethyl dihydrogenated tallow. The interlayer space (or d-spacing) between clay platelets is 22.3Å as measured by XPS. The nano-clay is dispersed in LLDPE, HDPE, and PEMA at 5wt% to form nanocomposite materials.

Table 3.4: Polymer and nano-filler used in experiments.

Material (Abbreviation)	Source (Trade name)	$M_w \cdot 10^{-4}$ (g/mol)	Density (g/cc, 25°C)
Polystyrene (PS)	Dow Chemical (Styron 666D)	16	1.05
Polystyrene-5% maleic anhydride (PSMA)	Arco (Dylark 332)	Not available	Not available
Polyamide (PA)	DuPont (Zytel330)	Not available	Not available
Polyethylene: high variance in MW (LLDPE)	Nova PE (PF0118F)	10.56	0.918
Polyethylene: low variance in MW-PE (HDPE)	Nova PE (SP Sclair 2907)	Not available	0.96
5% Maleic Anhydride Grafted Polyethylene (PEMA)	DuPont (Fusabond 2650)	4.84	0.73
Montmorillonite Clay (C20A)	Southern Clays (Cloisite 20A)	Not available	1.77

3.4.2 Mixing

The 3 mL MBM and the commercial 69 mL BM were used in this study to prepare polymer blends and nanocomposites. The MBM and the BM were driven by the Haake Rheocord 90 Torque Rheometer for the experiments. The barrel temperature for all mixers was set to be 200°C. For both the MBM and the BM, the speed ratio of left rotor to right rotor is 3 to 2. For both mixers, the rotation speed is 50 rpm for polymer blending and 150 rpm for nanocomposites compounding. For all the blending experiments, the mixers were filled to 78% of the total volume.

PS and PSMA were dried for at least 12 h at 80°C in a vacuum oven. All other materials were dried for a minimum of 24 h at 100°C. The polymer blends were added together into the mixers and mixed at 50 rpm for 10 minutes mixing. For nanocomposites, the mixer rotation rates were set to 50 rpm for 5 minutes and then increased to 150 rpm for another 10 minutes. The initial 5 minutes period at 50 rpm reduces the stress on the drive while melting the solid polymer pellets. After the total mixing sequence was completed, the samples were then removed and immediately quenched in liquid nitrogen. The samples fractured in the liquid nitrogen and these surfaces were used for further analyses.

3.4.3 Characterization

The morphology of each sample was characterized using a Hitachi S-2700 Scanning Electron Microscope (SEM). The SEM images were collected by a PGT (Princeton Gamma-Tech) Imx system. All samples were coated with a thin layer of gold.

The morphologies of the nanocomposites were examined by TEM with a Philips Morgagni 268 microscope. The samples were embedded in epoxy resin and ultra-microtomed with an Ultracut diamond knife at room temperature to produce sections with a nominal thickness of about 100nm.

The intercalation and exfoliation of nano-clay by polymer were determined using X-ray diffraction with a Rigaku diffractometer (Co K_α radiation, λ=0.1789nm) at room temperature. A disc-shaped sample with a diameter of 25mm was prepared using compression molding at about 200°C, and the sample was scanned in 2θ range from 1 to 11° at a scanning rate of 1° per min.

Differential scanning calorimeter (DSC) analysis was performed on a TA Instrument Model DSC2910. The samples were initially held at isothermal conditions for a minute, and were then heated from 35 to 180°C at a rate of 20°C/min. The melting temperature, crystallization temperature, and enthalpy of fusion were obtained using the TA2200 software package.

3.4.4 Temperature and torque measurement during a transient process

The Haake Rheocord 90 Torque Rheometer fitted with the mini-batch mixer was used for the transient experiment. The experimental set-up is shown in Figure 3.1. The barrel temperature was preheated to 190°C. The speed of left rotor (left as seen from front of the mixer) is 50 rpm and the right one rotated at 2/3 of left rotor speed (33 rpm). 2.65 g of polystyrene (PS, Dow Chemical, M_w=200K) was added to initially fill the mixer. A thermocouple was mounted in the center of the front plate (as shown in Figure 3.1b) to measure the melt temperature. When the melt temperature reached thermal steady state, the motor was stopped and the temperature slowly decreased to the barrel temperature. After the temperature was constant for 5 minutes, the motor was restarted, and the melt temperature was recorded every second using an OPTO 22 data-acquisition system.

3.5 Results and discussion

3.5.1 Simulation results

The same transient process as described in Chapter 2 for the BM was simulated for the MBM to study the effects of viscous dissipation on the temperature and velocity fields.

3.5.1.1 Heat transfer

Figure 3.4 showed the power and heat transfer rate change during the transient process. The power (P) calculated from the experimental torque matched well with the simulated value for heat generation by viscous dissipation. The heat generation rate of the MBM filled with PS from simulation oscillated around a constant value of 1.4 W. This meant that after reaching thermal steady state, the temperature inside MBM did not change much, and thus, it had a fairly constant value of heat generation. It took about 15 seconds for the MBM to reach thermal steady state.
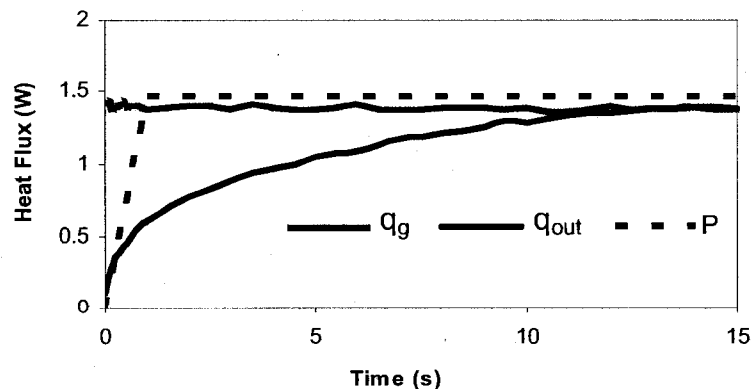
Figure 3.4: Dissipated power and heat flux across the wall for MBM.

To keep the barrel temperature constant during this transient process, the heat generated in the polymer melt and transferred to the barrel needed to be removed from the barrel instantly. In Chapter 2, we found that the cooling by natural convection was not sufficient to keep the barrel temperature of the 69 mL BM constant. When the mixer was scaled down by a scaling ratio L, the generated heat scales by L^{-3} while the wall surface area scaleed by L^{-2}. Due to the smaller amount of generated heat and the relatively larger heat transfer surface area, the temperature increase was relatively small and the temperature difference between the barrel and the polymer melt was also small. Therefore cooling by natural convection should be enough to remove the heat generated by polymer melt. To verify the heat removal capacity by natural convection, the overall heat transfer coefficient during the transient process was calculated using Equation 2.10 and the overall natural convection heat transfer coefficient was calculated using Equation 2.11. As shown in Figure 3.5, the instantaneous heat transfer coefficient (h_{ist}) was always lower than the natural convection transfer coefficient ($h_{natural}$) for the whole transient process. Therefore, the heat removed by the surrounding air was always higher than the heat transferred out from the polymer melt while the heaters inside the wall can supply enough heat to keep the wall temperature constant. This indicated that the barrel temperature can be well controlled for the MBM.
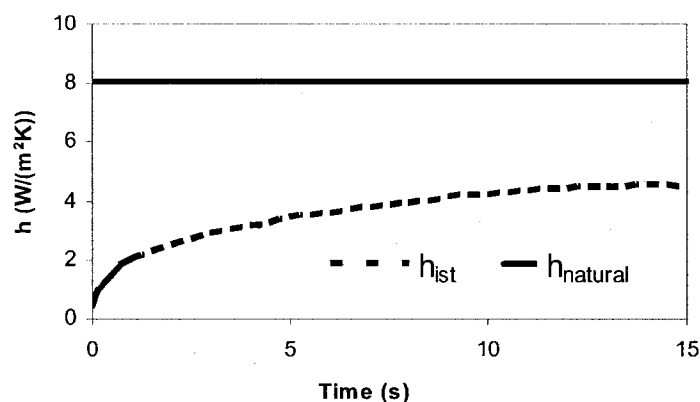
Figure 3.5: Overall heat transfer coefficient during the transient process.

Figure 3.6 showed the heat flux at the wall as a function of circumferential distance at three different times. The heat flux was calculated using Equation 2.15. The heat flux direction was perpendicular to the wall and flowed out of the mixer as indicated by the black arrows. The starting point (distance = 0) of the circumferential distance in the plot was the grey point shown on the circumference and the heat flux was plotted in the direction indicated by the white arrow tangent to the circumference. For the MBM, the heat flux around the left chamber oscillated around 600 W/m^2 after thermal steady state, which was double the value of the heat flux in the right chamber, due to the higher speed of left rotor. The viscous dissipation was roughly proportional to the square of the shear rate. Since shear rate was proportional to rotation rate, it was reasonable that the heat flux in the left chamber was double that in the right chamber. At the top of the middle part of the MBM, the heat flux was quite small and even close to zero. It was easy to see that both the velocity and the shear rate in this region were very small, hence the polymer melt was quiescent and not much energy was dissipated.
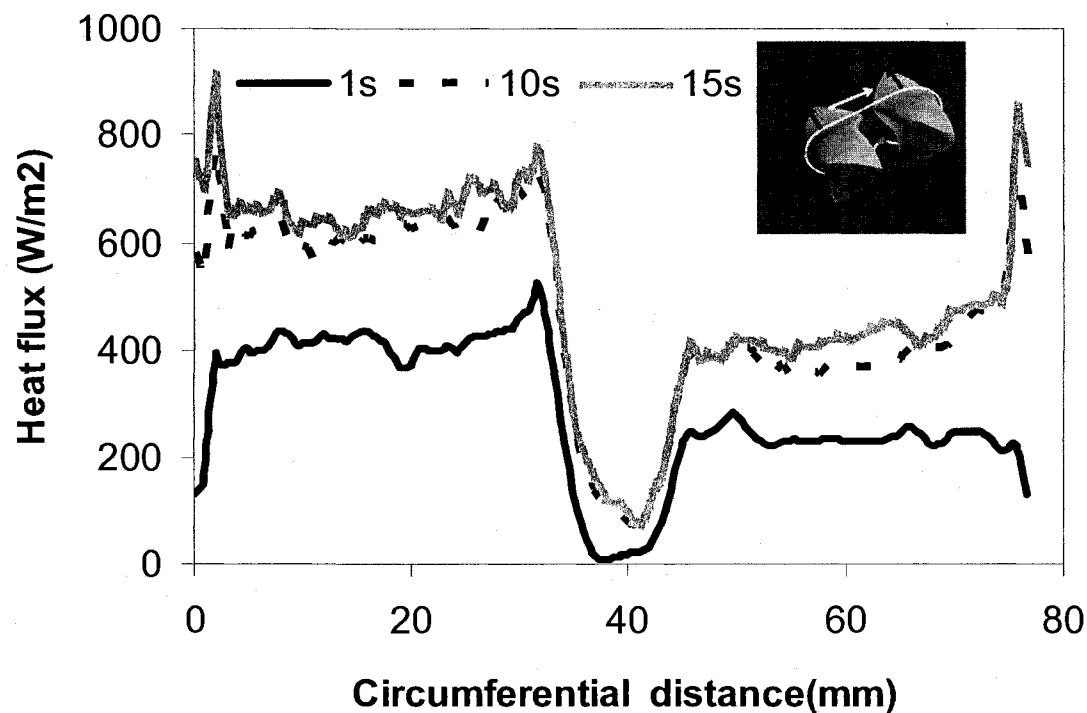
Figure 3.6: Heat flux as a function of the circumferential distance along the barrel wall at the center of the mixers. The curves started from the grey point in the center bottom; white arrow indicated direction of circumferential distance plotted on x-axis; and the heat flux direction is perpendicular to the outer surface as shown by the black arrow.

3.5.1.2 Temperature profile

Point temperature was taken from experiment to verify the validity of the heat transfer simulation. A thermocouple was mounted in the front part of the mini-batch mixer and was inserted 2 mm into polymer melt to measure the melt temperature. The location of the thermocouples was shown by the black circles in Figure 3.1b. We obtained the temperature from the same point in the mixer from the simulation. Figure 3.7 showed the comparison of the temperature increase until time obtained from both simulation and experiment as a function of time.

We can see the simulation data matched the experimental data very well. It took about 15s for polymer melt to reach a thermal steady state in MBM and the temperature increased less than one degree. The temperature oscillation seen in the simulation data was due to the different position of rotors during the process. The amount of viscous dissipation changed based on rotor position and hence, so did the melt temperature. We would see a similar oscillation in the experiment if there was better temperature resolution and faster temperature response for the thermocouple used in the experiment.
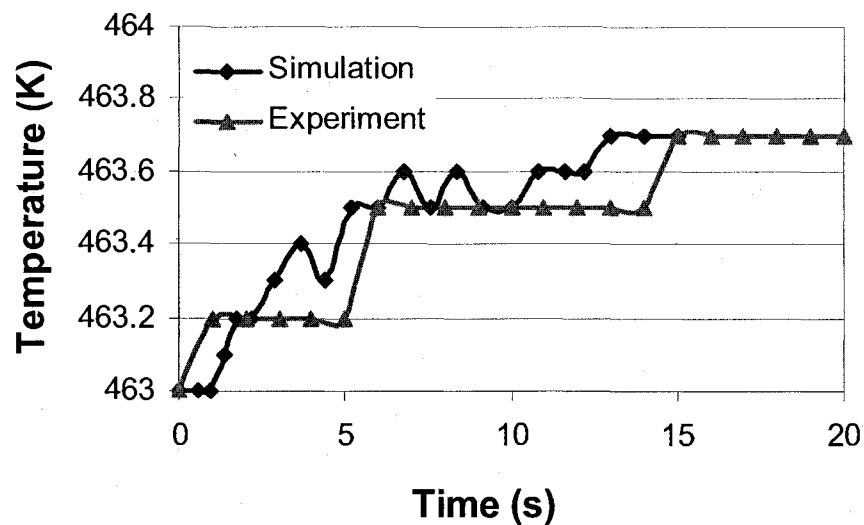
Figure 3.7: The temperature increase for the MBM as function of time. The simulation data and the experimental data are compared for melt temperature at a point in mixer.

To study the effect of location, the three cross-sections shown in Figure 3.8 were chosen as representative of the MBM to show the spatial distributions of temperature and velocity.
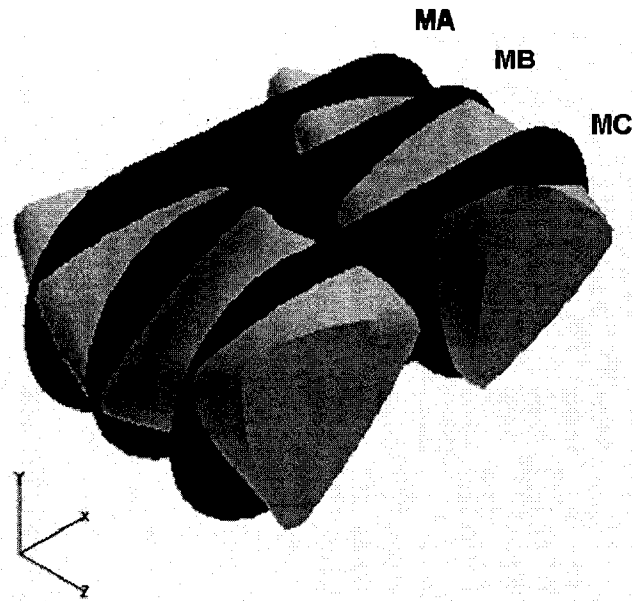
Figure 3.8: Three representative cross-sections for MBM: MA: close to the back plate of MBM; MB: in the center of MBM; MC: close to the front plate of MBM.

Figure 3.9 a-c showed the temperature distribution for cross-section MB at different times. The initial temperature of MBM was 463K. We can see that the melt temperature of the material near the left rotor increaseed faster than that near the right rotor due to a higher rotation speed of left rotor. In Figure 3.9a, after 1s mixing, there was a slight temperature increase in the minimum gap region between the tip of the left rotor and the barrel while the rest of the mixer was still roughly at the initial temperature. As time increases, more energy was dissipated and the temperature continued to increase. Meanwhile some of the material from left chamber (hot side) was transferred to the right chamber (cold side) and this intermixing promoted the temperature increase of material in the right chamber. As shown in Figure 3.9b, the temperature around the left rotor increased about 1K
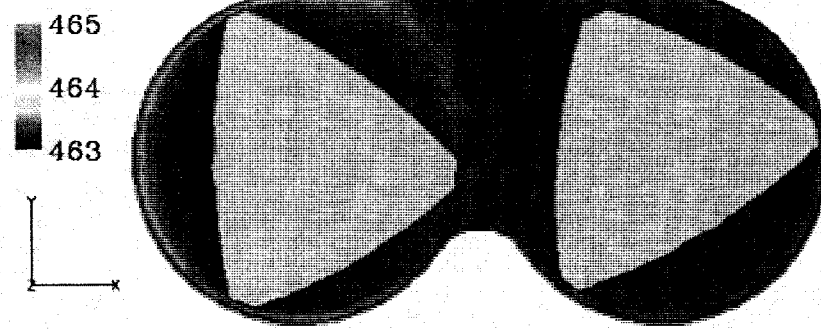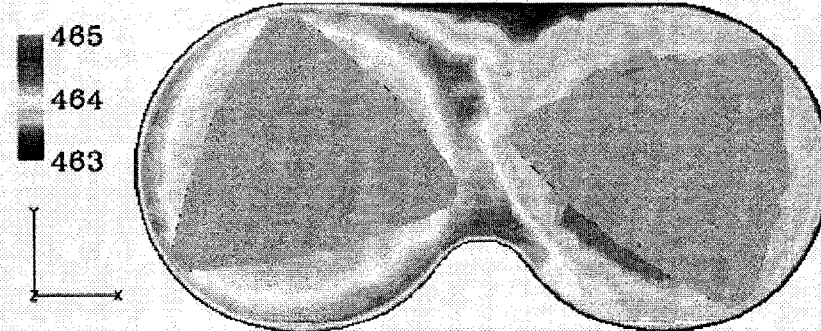
Figure 3.9: Temperature distribution of MB at different time: (a) t=1s; (b) t=10s; (c) t=15s; Minimum temperature 463K and maximum temperature 465K.

at 10s and temperature around the right one increases about 0.5K. Finally, when the total heat transfer across the wall equaled the generated dissipated power as shown in Figure 3.9c, the melt had a stable temperature and the thermal steady state was achieved. As shown in Figure 3.9c, the temperature in the whole flow domain was quite uniform and the average temperature increase was about 1K. The mixer did not have an equilibrium temperature at any point since the rotation of the rotors caused the temperature at a particular point to vary with time (see Figure 3.6 and 3.7).

Figure 3.1o compared the steady state temperature distribution at different axial locations MA and MC. Figure 3.10 showed that there were some hot spots existing in the MBM but with a much lower temperature compared to APAM. The highest temperature regions in MBM appeared near the left rotor which had a higher rotation speed and these high temperature regions were mostly in the area between the tips of the rotor and the barrel. The temperature distribution varied along the axial direction of MBM and with the rotation cycle due to the different rotor configurations at different times. The heat generated inside MBM was very small because the low sample mass and relatively lower shear rate resulted in a lower temperature increase (about 1K).
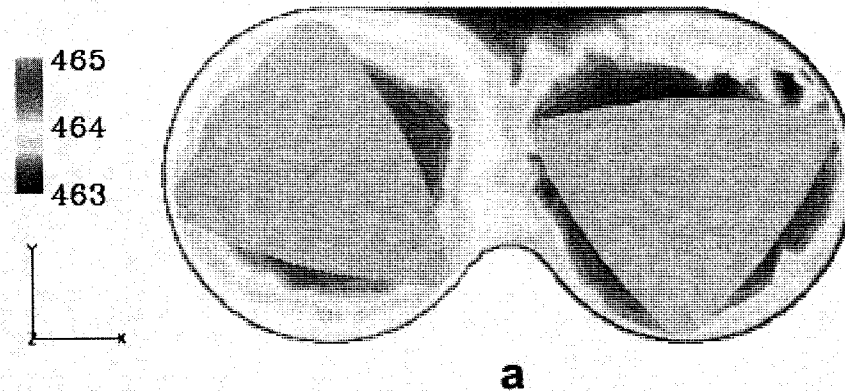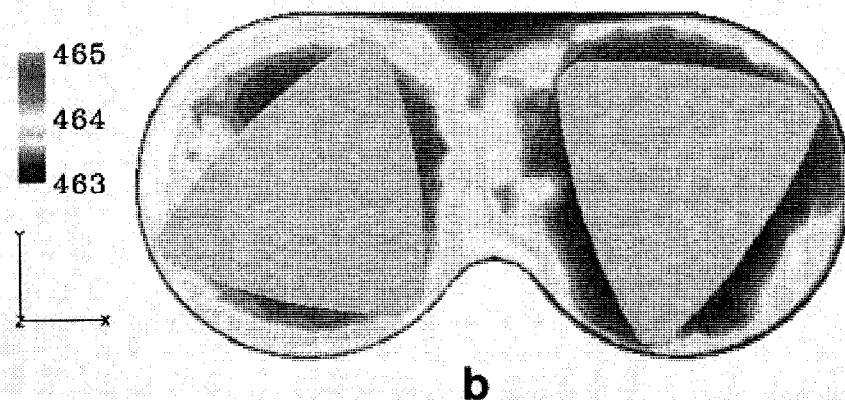
Figure 3.10: Temperature (K) distributions (Minimum temperature: 463K; Maximum temperature: 465K) for cross-sections MA and MC at thermal steady state: (a) MA; (b) MC

3.5.1.3 Velocity profile

As discussed in the literature [7, 22-25], the combined flow modes in an internal batch mixer played a very important role in determining the dispersion and distribution of the minor phase throughout the primary phase. Shear flow was the best understood among flow modes and provided the necessary shear stress to break up the droplets or clusters of particles for polymer compounding. It is also widely known that elongational flow is more efficient for promoting the dispersion of the minor phase than shear flow. Other flow modes such as folding

and splitting also played important roles in determining the final morphology of the polymer blends or composites.

Breuer et al [7] illustrated the various flow modes existing in an internal batch mixer according to literature and experience. They stated that shear flow dominates in most of the regions in the internal batch mixer while elongational flow exists at the narrow regions around the tips of the rotors. In the intermeshing area between the two rotors, flows from both sides of the rotor joined together and then splited. By simulation, we can actually see the distribution of various modes inside the mixer as shown in Figure 3.11. The arrows in the figure showed the flow direction and the length of the arrow indicated the magnitude of the velocity. The highlighted areas showed the locations of each flow mode in the mixer.
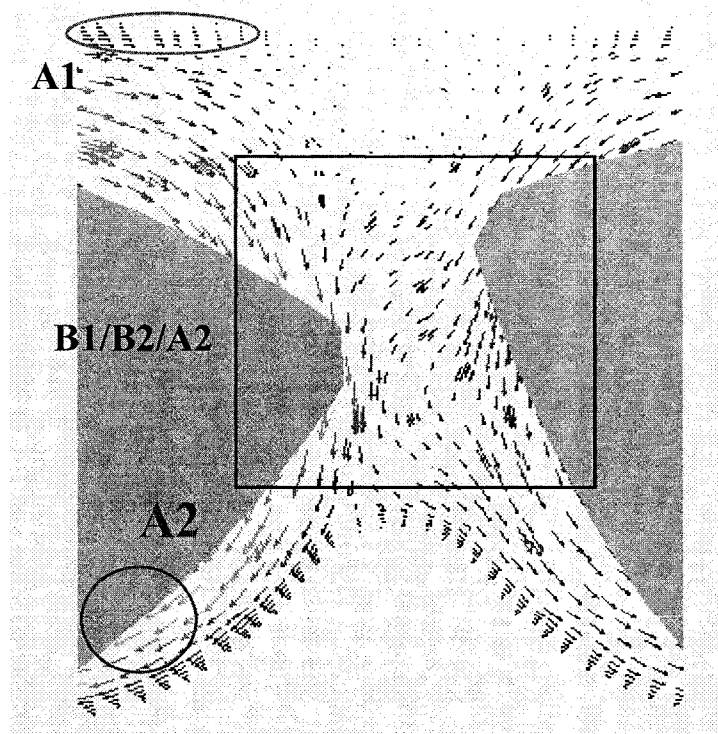
Figure 3.11: Flow modes in MBM: A1: shear flow; A2: elongational flow; B1: folding; and B2: splitting and joining of streams.

The rotational speed ratio of the left rotor to right rotor was 3 to 2 in the MBM. Due to the different rotors' speeds, the velocity profile of the MBM varied with both space and time. Figure 3.12 showed the velocity maps at three typical cross-sections MA, MB and MC from the front view. The magnitude of the velocity was scaled by the arrow length. The scale on the legend bar indicated the numerical value of the velocity vector. Figure 3.12 showed the radial velocity profiles of MBM at three typical cross sections, corresponding to the same locations in Figure 2.12. The maximum velocity was 0.036 m/s for the MBM compared to the maximum velocity 0.1m/s for the BM. The flow modes occurring in the MBM were much the same as in 69 mL BM in terms of the change with time and space except that the magnitude is different. In addition the MBM near top of the mixing chamber had a relative larger flat area where the melt had very small velocity.
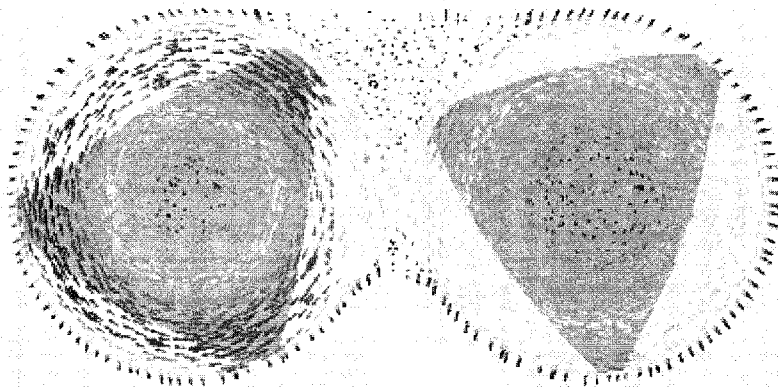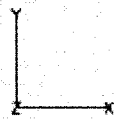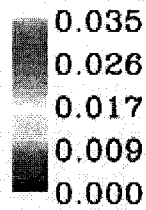
(a)
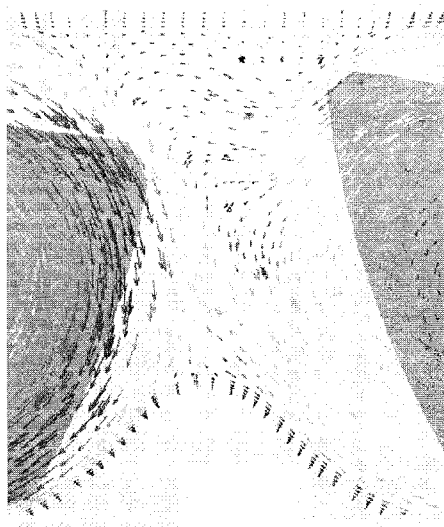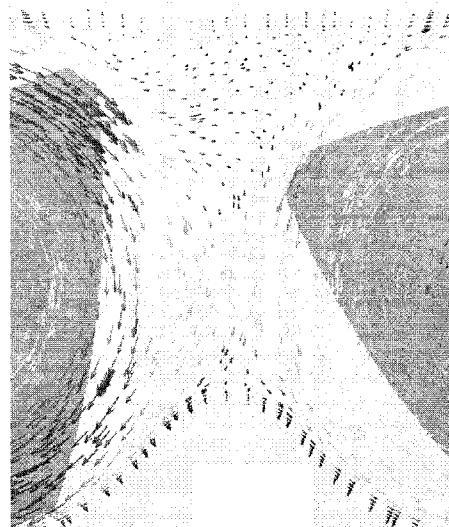
(b)   (c)

Figure 3.12: The radial velocity profiles of MBM at three typical cross sections. The magnitude of the velocity (m/s) can be determined by both the arrow size and the legend bar. The coordinate origin is set at the center of the mixer with positive Z in the direction toward the front of the mixer. (a): the overall velocity profile for cross-section MB; (b): the enlarged image of cross-section MA; (c): the enlarged image of cross-section MB; (d) the enlarged image of cross-section MC.

(d)

Figure 3.12 (Continued)

3.5.1.4 Flow index

The average shear rate and sometimes even shear rate distribution in the mixing equipment were important parameters when it came to evaluate the intensity of mixing and compare results from different types of mixers. In this chapter, we used our numerical method to get average shear rate and shear rate distribution of MBM and BM, and then compared the average shear rate of MBM and BM to the values obtained from empirical equations developed for similar mixers.

Using the shear-thinning viscosity of polystyrene at 190°C, the average shear rates of MBM and BM were 21 s^{-1} and 23 s^{-1} respectively at a rotation speed of 50rpm for left rotor and 33 rpm for right rotor in both mixers. Figure 3.13 showed the overall shear rate distribution of the two mixers and Figure 3.14 showed the shear rate space distribution in the typical cross-sections of the two
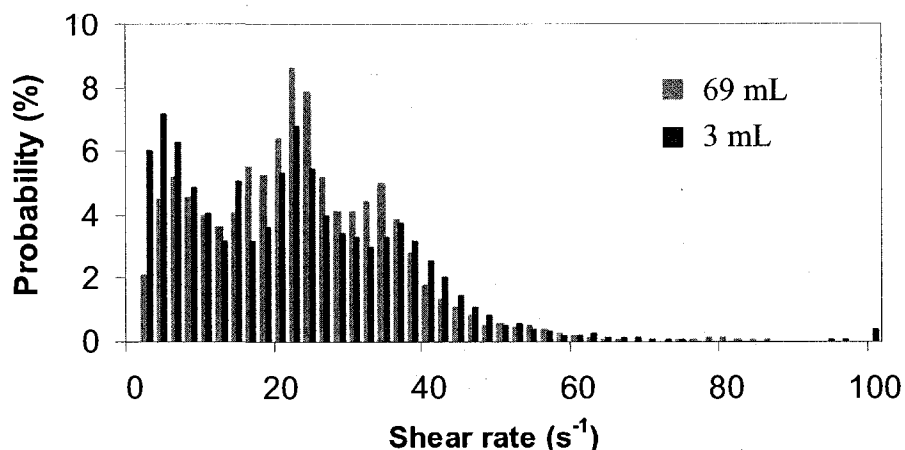
Figure 3.13: Shear rate space distributions of 69 mL BM and 3 mL MBM, the average shear rates of BM and MBM are 23s^{-1} and 21s^{-1} respectively.

mixers. It was found that MBM had a similar shear rate distribution with that of BM and there were four peaks in the distribution curves for both of them. The first peak around 6 s^{-1} corresponded to the areas near to the flat top surface and some small areas very close to the rotors. Since MBM had a larger portion of areas near the top flat surface, it had a larger portion of low shear rate around 6s^{-1}. The other shear rate peaks were around 30 s^{-1} which corresponded to the gaps around the tips of left rotor, and 20 s^{-1} which corresponded to the gaps around the tips of right rotor. For both MBM and BM, only a very small portion of the mixers had a shear rate over 50 s^{-1} although their maximum shear rates were up to 100 s^{-1}.

(a)

(b)
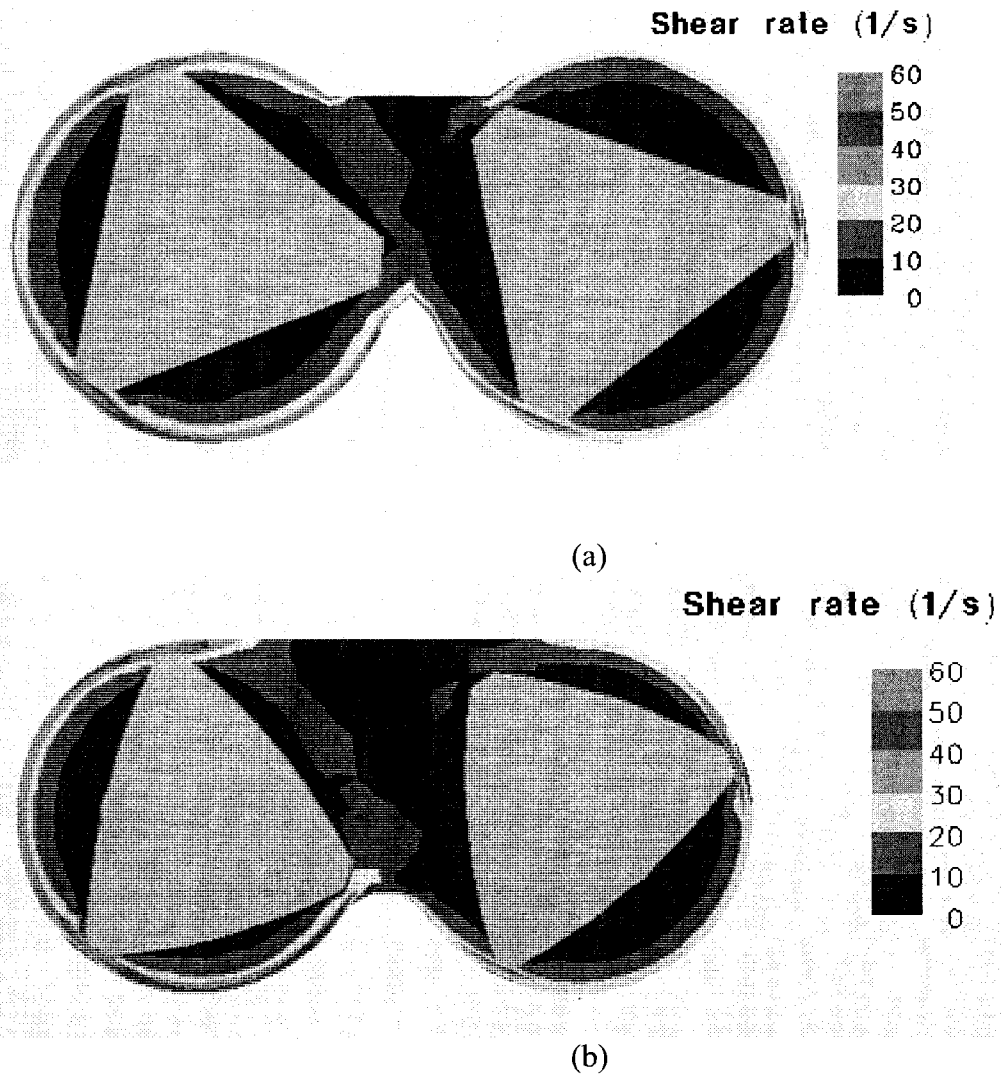
Figure 3.14: Shear distributions of MBM and BM at the center cross-sections: (a) 69 mL BM; (b) 3 mL MBM

Due to the similar configuration between the 3 mL MBM and the 69 mL BM, we used the same calculation as reported by Yang et al [26] to correlate the rotation speed of MBM with shear rate. Based on their 2-D analysis, the maximum and minimum shear rate were 1.80N and 0.22N, where N was the rotation speed. Therefore, in our case, the respective values were 90 s^{-1} and 11 s^{-1}

at a rotational speed of 50 rpm. Considering that we used different polymer material, these values were in a reasonable range and comparable to our simulation results.

Figure 3.15 showed the shear rate distribution inside MBM after thermal steady state was reached. Around the circumferences of section MA, MB and MC, the shear rate changed with varying clearance, and whether it was the right or left side of the mixer due to the different speeds of two rotors. The highest shear rate in MBM was 110 s^{-1} and was always located near the tips of left rotor in the narrow gap between left rotor and barrel wall.
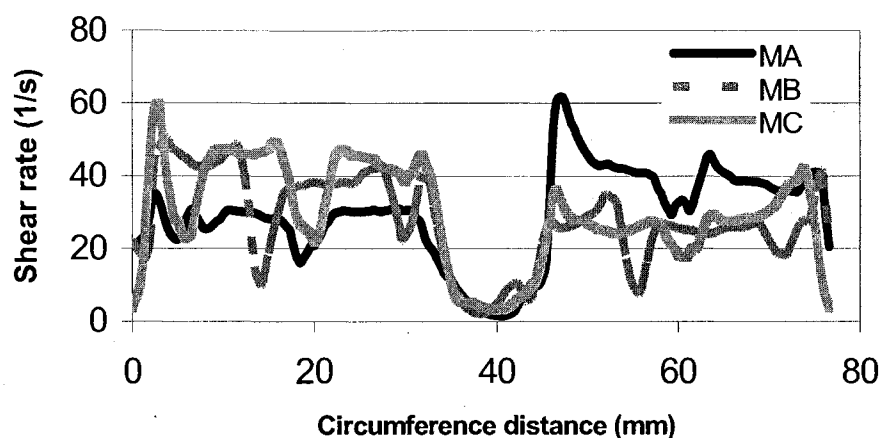
Figure 3.15: Shear rate distributions at cross sections of MBM. Shear rate change along the circumference of the cross-sections MA, MB and MC of MBM when thermal steady state is reached.

When mixing polymer blends, the minor component was usually dispersed as drops or filaments in a polymer matrix [27]. The breakup of these droplets or filaments was governed by the balance of the cohesive forces within these droplets and the shear stress exerted by the external flow field. Hence, the magnitude and distribution of the shear stress had a decisive impact on the shape and size of the dispersed phase. The shear stress calculated by simulation ranges

from 0 to 92 kPa for MBM. Figure 3.16 showed the shear stress distribution at the center cross-sections of BM and MBM respectively. For both mixers, we can see that the whole flow domain was clearly divided into two zones in terms of the magnitude of hydrodynamic force: one "strong" zone was near the smallest gap with a very high shear stress which had a low volume, and the other "weak" zone was the rest of the mixer with relatively low stress but encompasses most of the volume of the mixer. The strong zone only occupied a small portion of the whole space for both mixers.
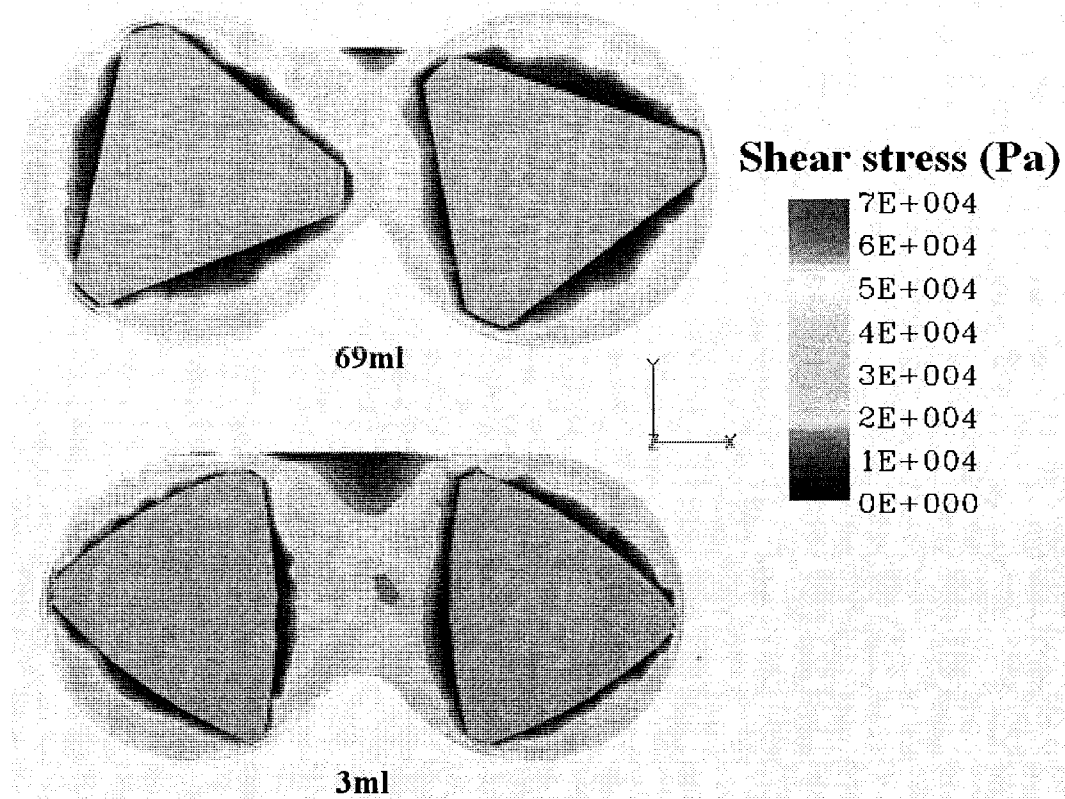
Figure 3.16: Shear stress (Pa) distributions at the center cross-sections for 69 mL BM and 3 mL MBM.

Manas-Zloczower [25] defined a parameter, mixing index (MI), which was usually called flow strength or flow number to quantify the dispersion:

$$MI = \frac{|D|}{|D| + |\omega|}$$

(3.2)

where $|D|$ and $|\omega|$ were the magnitudes of the rate of strain and vorticity tensors respectively. MI was the relative portion of the magnitude of the rate of strain versus the sum of the magnitude of the rate of strain and the magnitude of the vorticity tensor. For pure solid rotation, the magnitude of the rate of strain was zero because there was no strain change and therefore MI was zero. For shear flow, the magnitude of the rate of strain equalled the magnitude of the vorticity tensor and MI equalled 0.5. The magnitude of the vorticity tensor was zero for elongational flow and MI equalled 1. Since MI was an indicator of flow type, it became an indirect parameter to characterize dispersive mixing. This parameter was used by Manas-Zloczower group [28, 29] to compare the dispersive mixing efficiency of different mixing equipment and processing conditions.

Figure 3.17 showed MI distributions of BM and MBM at the centered xz cross-sections from top view. The blue, green and red color indicated solid rotation (0), shear flow (0.5) and elongational flow (1) respectively. For both mixers, the rotors experienced the pure rotation all the time. Elongational flow existed in the middle part between the two rotors while shear flow dominated in the rest of the chamber. Simulation showed that MBM had comparable amount of elongational flow as BM.
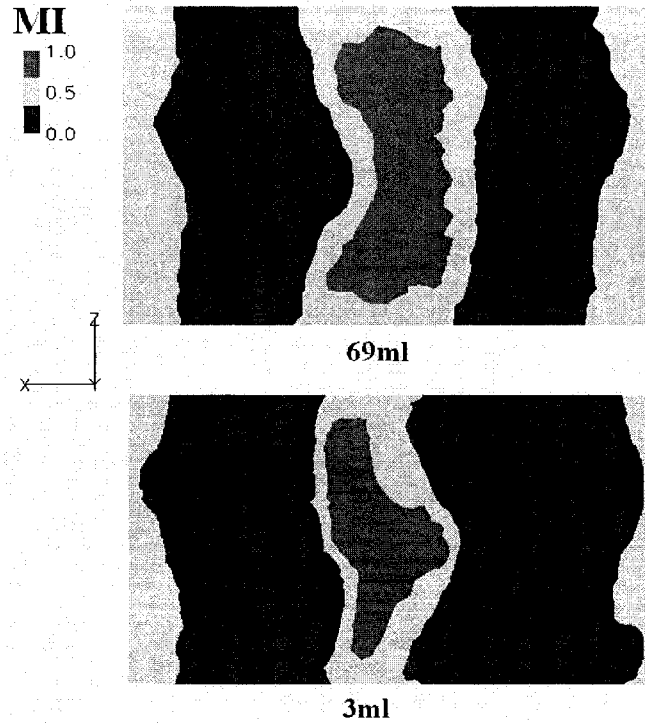
Figure 3.17: MI distribution for 3 mL MBM and 69 mL BM at centered xz cross-sections
from top view.

The thermal characteristics and flow parameters of MBM and BM were

summarized and compared in Table 3.5.

Table 3.5: Summary of thermal and flow parameters.

	69 mL BM	3 mL MBM
Time to reach thermal steady state (s)	80	15
Average steady-state temperature difference (K) due to viscous dissipation.	3	1
Average consumed power (W)	30	1.5
Maximum velocity (m/s)	0.1	0.36
Average shear rate (s^{-1})	23	21
Average shear stress (kPa)	34	30

3.5.2 Experimental results

3.5.2.1 Morphology of polymer blends

Sundararaj et al [13] investigated the morphology evolution of PS/PA in the BM and found that the particles of PA dispersed phase were all spherical and the sizes of the particles ranged from approximately 0.5 to 5 microns after 7mins mixing. The same processing conditions were used for BM and MBM to blend PS and PA with a weight ratio of 80:20. Figure 3.18 showed the morphology of PS/ PA (80:20) system at a constant rotation speed of 50 rpm for 10 minutes. PA was dispersed in the continuous phase of PS as spherical particles and the phase domains were relatively uniform throughout the blend. For both mixers, the diameter of the dispersed phase was several microns, which indicated that MBM had a comparable mixing efficiency to the BM for PS/PA immiscible blends.

Figure 3.19 showed the morphology of PSMA/PA blends. Because of the adhesion at the interface created by the reaction between the functional group of MA from PSMA and the functional group of NH_2 from PA, the interfacial stress between the two phases was greater and the dispersed particles were much finer compared to the morphology of PS/PA. The diameter of the dispersed particles was well below 1 micron for both mixers. Both mixers produced a very similar morphology for non-reactive and reactive blends.
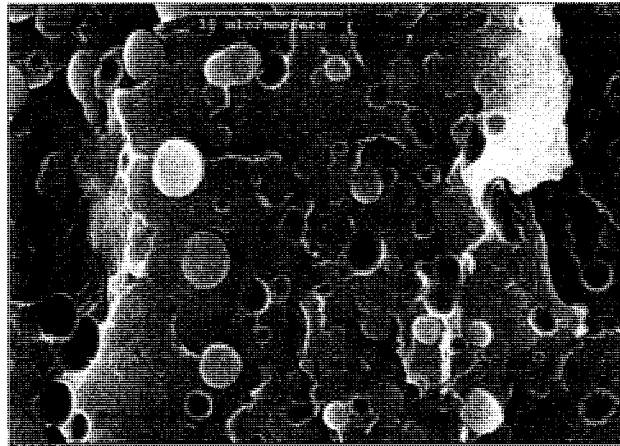
(a)
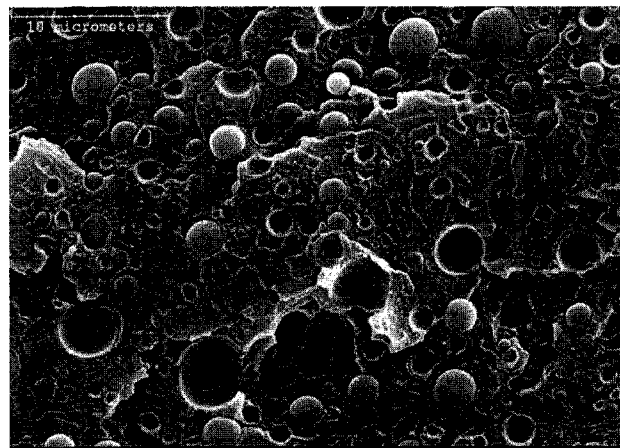
(b)

Figure 3.18: Morphology of PS/PA blends mixed by the miniature mixers at 50 rpm: (a) BM; (b) MBM.

(a) BM
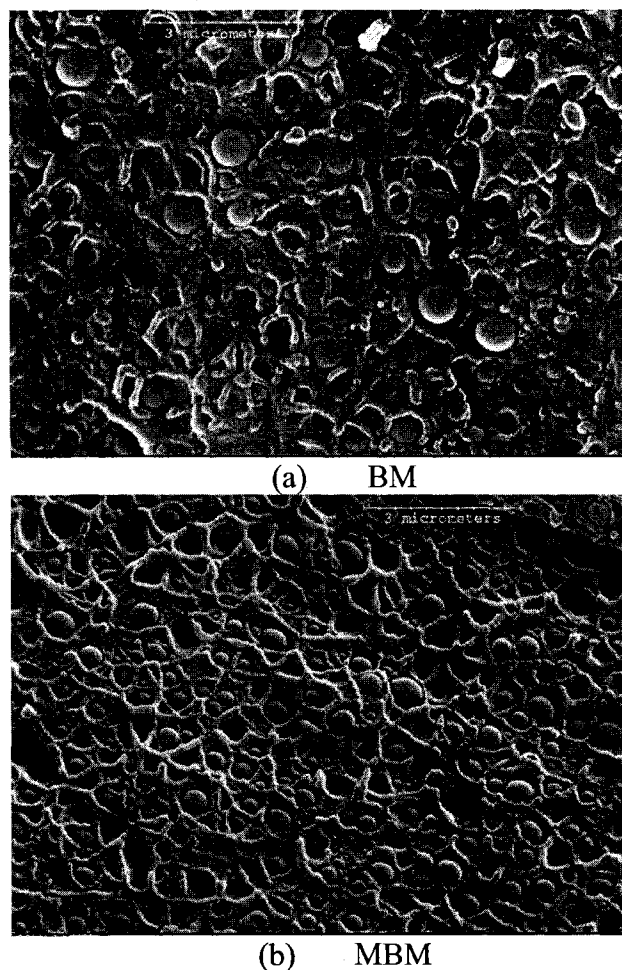
(b) MBM

Figure 3.19: Morphology of PSMA/PA blends mixed at 50 rpm by: (a) BM; (b) MBM.

3.5.2.2 Polymer nanocomposites processing in BM and MBM

Polymer nano-composites are drawing more and more attention due to their outstanding performance and potential for advanced application. Currently there are several methods used to produce these polymer nanocomposites: melt mixing, in-situ polymerization and solution processing. Among these methods, melt mixing is the preferred procedure because it is simple and most environmentally friendly. The objective of melt-mixing is to produce enough shear force to break the nano-aggregates and sufficient extensional flow to accelerate dispersion and

orientation. As illustrated in Figure 3.20, incorporating nano fillers into polymers by melt-mixing may result in no dispersion, partial dispersion or complete dispersion depending on the mixing efficiency. Nano fillers tend to have much larger cohesive forces because of the smaller size and the relatively large aspect ratio, so high shear stress and a high fraction of elongational flow are needed to disperse the clay throughout the polymer phase.
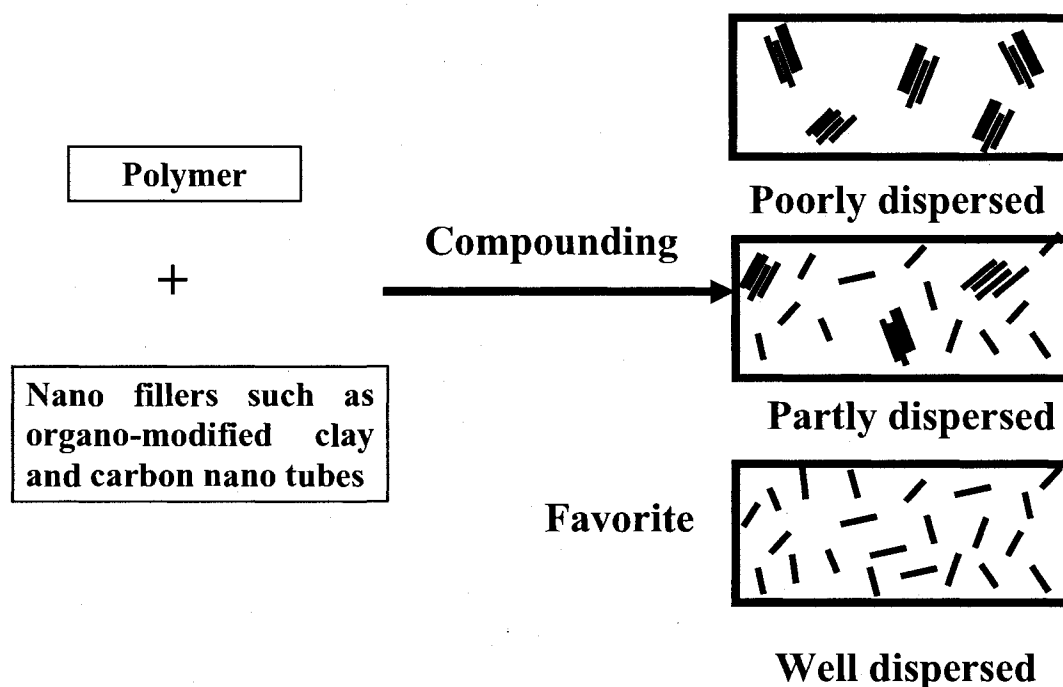
Figure 3. 20: Direct compounding of polymer nanocomposites.

Mixing equipment such as the batch mixer and the twin-screw extruder were previously used to disperse organoclay and carbon nanotubes into polymer matrix and the effects of processing conditions on the morphology were discussed. The main objective of creating the 3 mL MBM was to use it for processing specially polymer nanocomposites. Because of the geometrical similarity with the 69 mL

BM, the 3 mL MBM is expected to produce a comparable mixing effect to the BM.

In this chapter, both the BM and the MBM were used to mix PE and PEMA with clay C20A. Figure 3.21 shows XRD patterns of PE/C20A with the 5wt% of C20A content. The XRD patterns indicate the order of silicate layers in C20A. The interlayer space (or d-spacing) between the silicate platelets can be obtained by Bragg's law:

$$2d \sin \theta = \lambda \qquad (3.3)$$

where λ is a constant wavelength and is 0.1789 nm. The pure C20A consists of a high ordered arrangement of silicate layers and has a broad intensity peak at a 2θ value of $4.6°$, corresponding to a d-spacing of 2.23 nm. This is slightly lower than the reported value of 2.42 nm [30]. When mixing polymer with clay, the polymer molecules penetrate into the clay interlayer and swell the interlayer distance. For PE/C20A mixed with 69 mL BM, the clay peak shifts to about $4.0°$ indicating that the d-spacing increases to 2.56 nm. In comparison, the XRD pattern of PE/C20A mixed by 3 mL MBM shows a lower angle of $3.2°$ and a corresponding d-spacing of 3.2 nm.
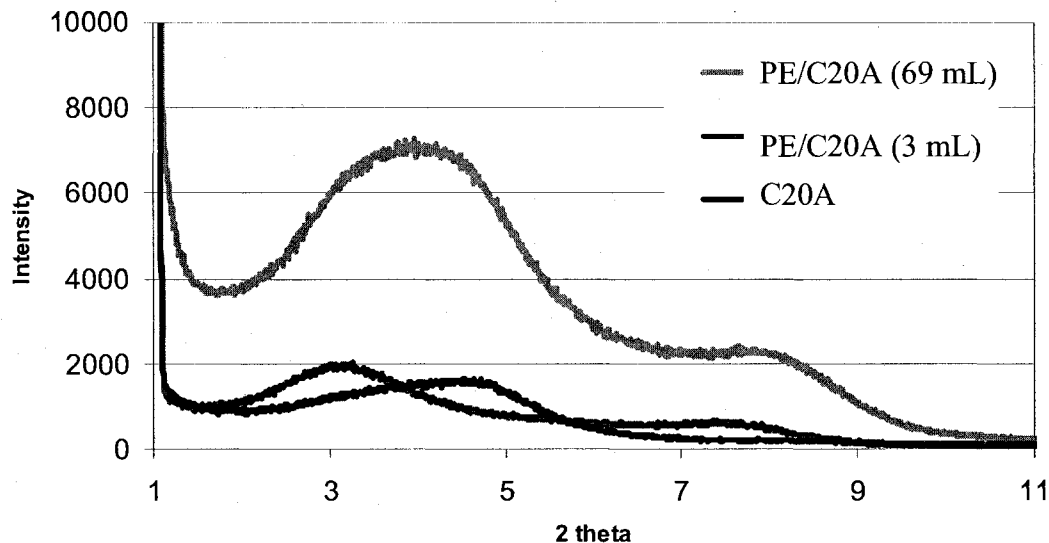
Figure 3. 21: XRD patterns of C20A and PE/C20A (95:5) nanocomposites mixed by 3 mL MBM and 69 mL BM.

Figure 3.22 shows the backscattered SEM images of the PE/C20A nanocomposites at 3000X magnification. For the backscattered images, clay appears as the lighter (white) phase while the polymer matrix appears as the darker phase. The SEM images of PE/C20A mixed by both the MBM and the BM show a fair amount of large clay agglomerates and some tactoids throughout the polymer matrix. The size of the clay agglomerates ranges from 0.5 to 10 micron. Generally, the PE/C20A nanocomposite mixed by the MBM has a slightly finer structure than that mixed by the BM.

(a)

(b)

Figure 3. 22: SEM micrograph of PE/C20A (95:5) mixed with (a) 69 mL BM and (b) 3 mL MBM.

Because of the nonpolar characteristics of PE, it is very difficult to disperse the silicate layers in PE. Researchers [31-33] have been using maleic anhydride grafted polyethylene as a compatibilizer to improve the dispersion of the silicate layers throughout the PE matrix. While keeping the content of C20A at 5wt%, we

added 30wt% of PEMA into PE and C20A to form PE/PEMA/C20A (65:30:5) nanocomposites.

As shown in Figure 3.23, the characteristic peak of the clay in PE/PEMA/C20A (65:30:5) disappears for both mixers. The disappearance of the characteristic peak generally indicates a complete exfoliation or very high intercalation of the silicate layers in polymer matrix.
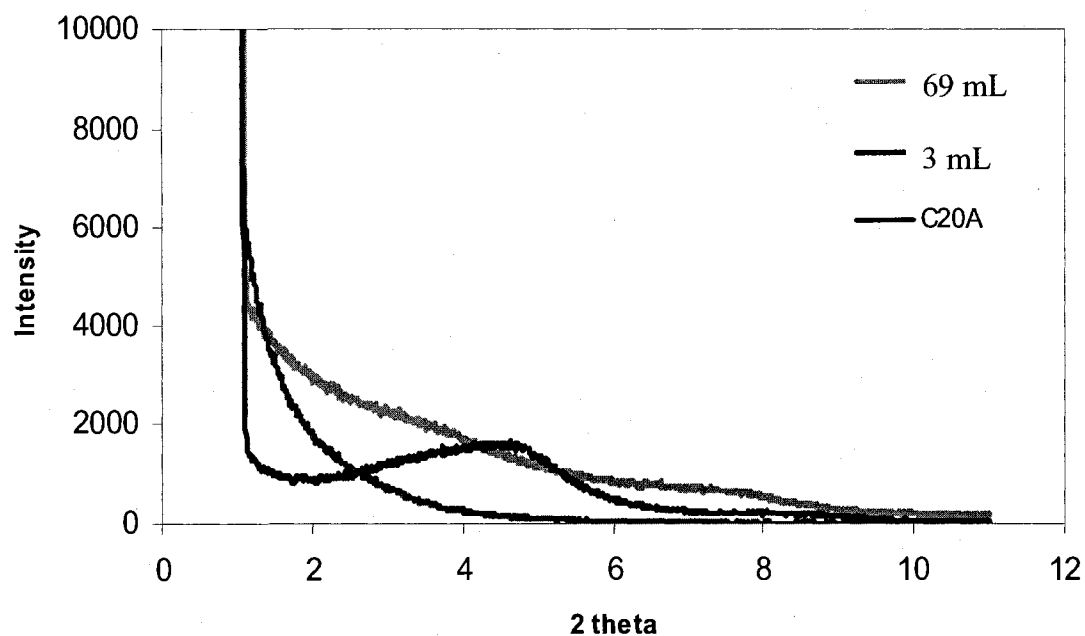
Figure 3. 23: XRD patterns of C20A and PE/PEMA/C20A (65:30:5) nanocomposites mixed with 3 mL MBM and 69 mL BM.

To verify the extent of the clay exfoliation in PE/PEMA, the backscattered (BSE) and the secondary images (SE) were taken at 3000X magnification. It is necessary to compare BSE with SE to have a better understanding of the morphology because some lighter regions in the BSE correspond to fractures on

the surface. After comparing the BSE and SE shown in Figure 3.24, we found

that the brightest regions in BSE are the fractures and the relatively darker fine

particles with the diameter below 0.1 micron are clay. Although the XRD

patterns show good exfoliation in PE/PEMA/C20A nanocomposites, there are still

(a)

(b)

(c)

(d)
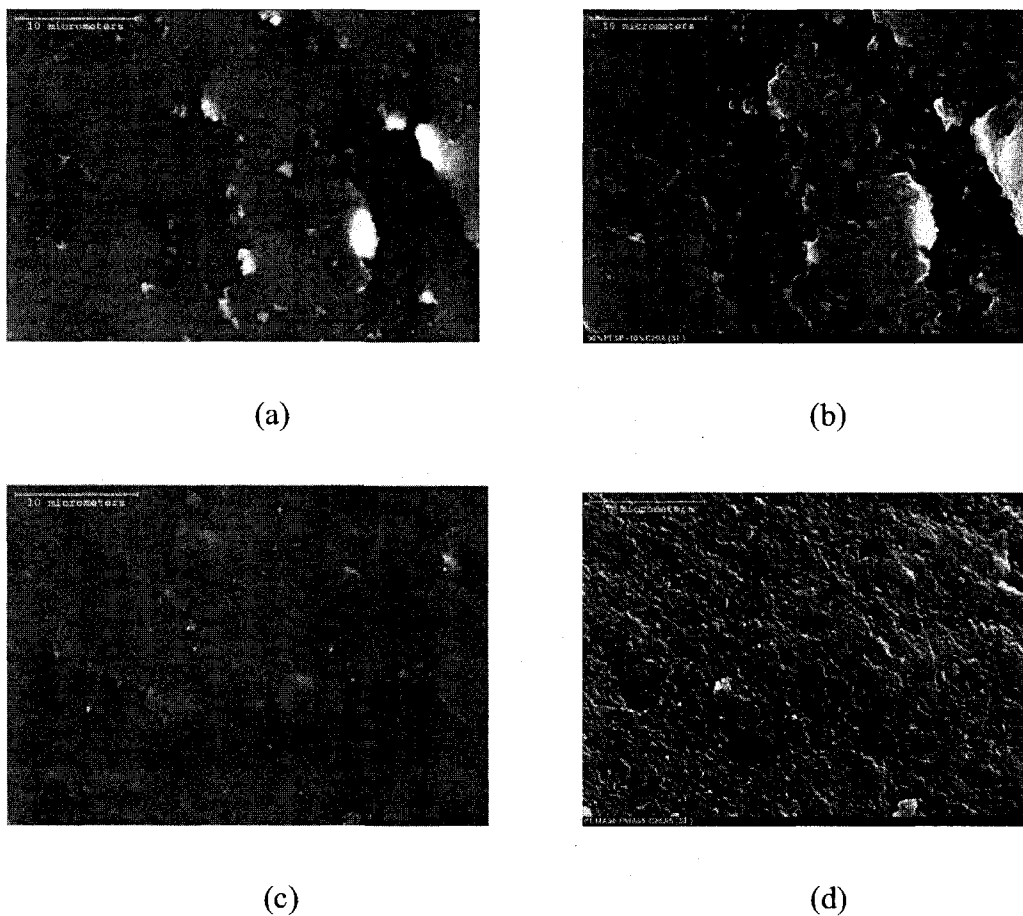
Figure 3. 24: SEM micrograph of PE/PEMA/C20A (65:30:5) mixed by 69 mL BM and 3 mL MBM: (a) BSE for 69 mL; (b) SE for 69 mL; (c) BSE for 3 mL; (d) SE for 3 mL.

clay tactoids scattered throughout the polymer matrix. Again the 3 mL MBM

shows a better degree of exfoliation compared to the 69 mL mixer.

Figure 3.25 shows the XRD patterns of PEMA/C20A (95:5). As expected, there is no characteristic peak of C20A for PEMA/C20A nanocomposites prepared in both mixers.
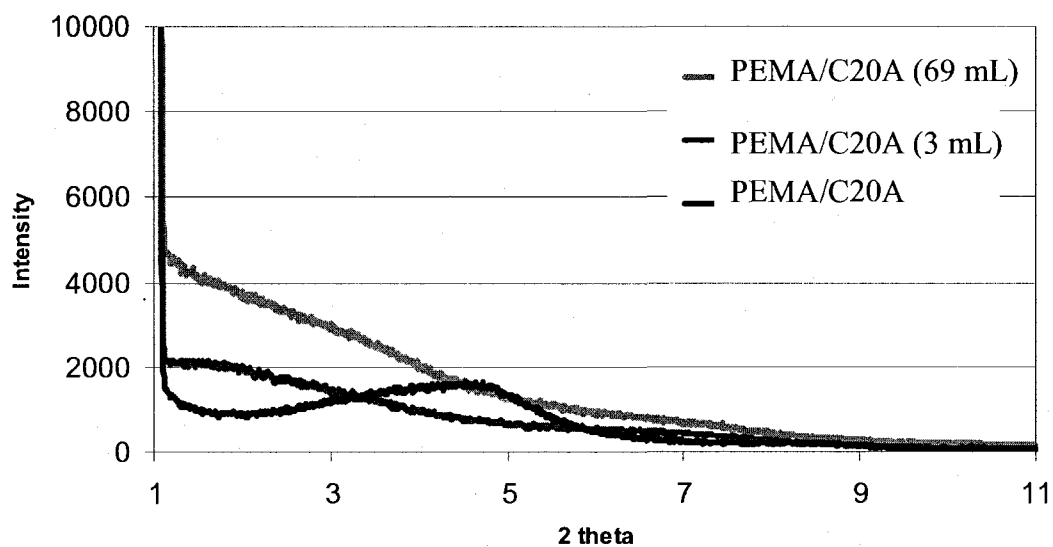
Figure 3. 25: XRD patterns of C20A and PEMA/C20A (95:5) nanocomposites for 3 mL MBM and 69 mL BM.

When looking at the corresponding SEM images shown in Figure 3.26, we found an overall well exfoliated structure but there are still a few large clay agglomerates in the PEMA matrix.

(a)

(b)

(c)

(d)
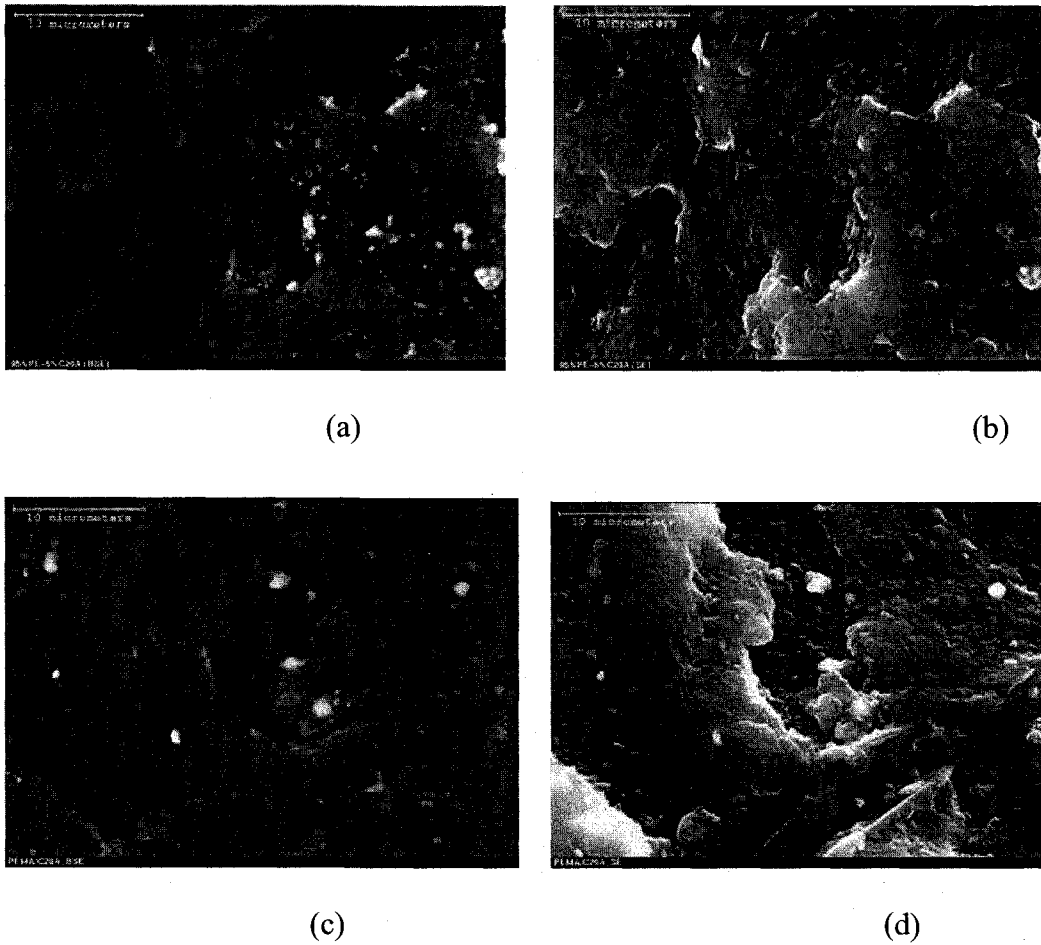
Figure 3. 26: SEM micrograph of PEMA/C20A (95:5) mixed by 69 mL BM and 3 mL MBM:
(a) BSE for 69 mL; (b) SE for 69 mL; (c) BSE for 3 mL; (d) SE for 3 mL.

Differential scanning calorimetry (DSC) was used to determine the crystallinity of the above nanocomposites by the following equation:

$$Crystallinity = \frac{\Delta H_m}{\Delta H_o}$$

(3.4)

where ΔH_m is the heat of melting calculated by integrating the melting transition peak [34] and ΔH_o is the heat of fusion of orthorhombic polyethylene, 290 J/g [35]. The exfoliated silicate layers increase the crystallinity of PE by acting as a bonding agent between molecules of the polymer matrix [36]. The crystallinity of

each nanocomposite is calculated by Equation 3.4 and summarized in Table 3.6 along with the d-spacing of each sample. Overall the crystallinity of the nanocomposites increases with the content of PEMA and it is seen that the nanocomposites mixed by MBM have a slightly greater degree of exfoliation.

Table 3.6: Summary of d-spacing and crystallinity for all samples.

PE	PEMA	Clay	Mixer size (ml)	d-spacing (Å m)	Crystallinity
95	0	5	69	26.5	0.29
65	30	5	69	exfoliated	0.38
0	95	5	69	exfoliated	0.59
95	0	5	3	31.2	0.29
65	30	5	3	exfoliated	0.33
0	95	5	3	exfoliated	0.51

3.6 Conclusions

A 3 mL internal batch mixer miniature mixer was developed by scaling down a large 69 mL laboratory batch mixer. The new mixer was used to mix polymer blends and nanocomposites. Numerical simulation of the transient non-isothermal case for both the MBM and the BM shows that the MBM has a similar velocity profile to the BM in terms of time and space. For the MBM, the point temperature from simulation agrees very well with that found from experiment. This indicates that our numerical models are valid and can be used for further study on different types of mixers, and in particular, to optimize mixer designs. The heat transfer via natural convection is sufficient to keep the barrel temperature of the MBM constant without any cooling system. The temperature increase in the MBM due to viscous dissipation is about 2 to 3K and this will not cause any serious thermal degradation. The MBM's average shear rate of 21 s^{-1}, which is very close to the average shear rate of BM which is 23 s^{-1}. This combined with a similar shear rate distribution and similar mixing index distribution to the BM, indicates that the MBM has a mixing performance comparable to the BM.

The MBM was tested for its ability to process polymer blends and polymer nanocomposites. Under the same processing condition and materials, MBM produced a similar and, in many cases, an even finer dispersed morphology than the BM did, especially for nanocomposites. By direct melt-mixing in the MBM and the BM, an exfoliated structure was obtained for PE/clay nanocomposites by adding 30wt% of PEMA.

Overall, the MBM shows a very good mixing performance for compounding polymer blends and nanocomposites and has a strong potential to be used as a miniature mixer to compound polymers with high-cost nanofillers for evaluation purposes.

No Text

No Text

3.7 Reference

1. Maxwell B., "Miniature Injection Molder Minimizes Residence Time", *SPE Journal*, **28**, 24, 1972.

2. Sundararaj U. and Macosko C. W., "Milligrams to Kilograms: An Evaluation of Mixers for Reactive Polymer Blending", *Polymer Engineering and Science*, **35**, 100, 1995.

3. Marechal P., Chiba T., Inoue T., "Melt Blending of dissimilar polymers by a small scale mixer: mixing with steel balls", *Polymer Networks and Blends*, **7**, 61, 1997.

4. Maric M. and Macosko C. W., "Improving polymer blend dispersions in Mini-Mixers", *Polymer Engineering and Science*, **41**, 118, 2001.

5. Yang B., Sato M., Kuriyama T., Inoue T., "Improvement of a gram-scale mixer for polymer blending", *Journal of Applied Polymer Science*, **99**, 1, 2006.

6. Scott C. E. and Macosko C. W., "The recirculating screw mixer: a new small-volume mixer for the polymer laboratory", *Polymer Engineering and Science*, **33**, 1065, 1993.

7. Breuer O., Sundararaj U., and Toogood R. W., "The design and performance of a new miniature mixer for specialty polymer blends and nanocomposites", *Polymer engineering and Science*, **44**, 868, 2004.

8. http://www.daca.com/productsdaca/mcpage.html

9. http://www.thermo.com/com/cda/product/detail/1,1055,21955,00.html

10. Cho JW, Kim PS, White JL, Pomini L, "Flow visualization in an internal mixer using an adjustable rotor system - Comparison of double flighted and four flighted rotors", *Kautschuk Gummi Kunststoffe*, **50 (6)**, 496, 1997.

11. Wang T. H., Manas-Zloczower I., "Two-dimensional dynamic study of the distributive mixing in an internal mixer", *International Polymer Processing*, **IX**, 3, 1994.

12. Yang H. H., Manas-Zloczower I., "3-D flow field analysis of a Banbury Mixer", *International Polymer Processing*, **7 (3)**, 195, 1992.

13. Sundararaj U., Macosko C. W., "Morphology development in polymer blends", *Polymer Engineering and Science*, **32**, 1814, 1992.

14. Mckelvey J. M., *"Polymer processing"*, New York, 1962, Ch. 12.

15. Palmgren H., "Processing condition in the batch-operated internal mixer", *Rubber Chemistry and Technology*, **48**, 462, 1974.

16. Goodrich J. E. and Porter R. S., "A rheological interpretation of torque-rheometer data", *Polymer Engineering and Science*, **7**, 45, 1967.

17. Bousmina M., Alt-Kadi A., and Faisant J. B., "Determination of shear rate and viscosity data from batch mixer data", *Journal of Rheology*, **43**, 415, 1999.

18. Alt-Kadi A., Marchal P., Choplin L., Chrissemant A., and Bousmina M., "Quantitative analysis of mixer-type rheometers using the coquette analogy", *The Canadian Journal of Chemical Engineering*, **80**, 1166, 2002.

19. Valera T. S., Demarquette N. R., and Toffoli S. M., "Effect of filling factor on the determination of shear rate and viscosity from batch mixer", *Journal of Polymer Engineering*, **24**, 409, 2004.

20. Wang W. and Manas-zloczower I., "Temporal distributions: the basis for the development of mixing indexes for scale-up of polymer processing equipment", *Polymer Engineering and Science*, **41**, 1068, 2001.

21. Dhanasekharan K. M. and Kokini J. L., "Design and scaling of wheat dough extrusion by numerical simulation of flow and heat transfer", *Journal of Food Engineering*, **60**, 421, 2003.

22. Taylor G.I., "The formation of emulsions in definable fields of flow", *Proceedings of the Royal Society of London. Series A, Mathematical and Physical Sciences*, **146 (858)**, 501, 1934.

23. Stone H. A., Bentley B. J., Leal L. G., "An experimental-study of transient effects in the breakup of viscous drops", *Journal of Fluid Mechanics*, **173**, 131, 1986.

24. Utracki L. A., Shi Z. H., "Development of polymer blend morphology during compounding in a twin-screw extruder: 1. Droplet dispersion and coalescence - a review", *Polymer Engineering and Science*, **32 (24)**, 1824, 1992.

25. Manas-Zloczower I., "Analysis of mixing in polymer processing equipment", *Rheology Bulletin*, **66 (1)**, 5, 1997.

26. Yang LY, Bigio D, Smith TG, "Melt blending of linear low-density polyethylene and polystyrene in a Haake internal mixer. II: morphology-processing relationships", *Journal of Applied Polymer Science*, **58**, 129-141, 1995.

27. Janssen JMH, Meijer HEH, "Dynamics of liquid-liquid mixing: a 2-zone model", *Polymer Engineering and Science*, **35 (22)**, 1766, 1995.

28. Yang H. H., Manas-Zloczower I., "3-D flow field analysis of a Banbury mixer", *International Polymer Processing*, **VII**, 195, 1992.

29. T. Li, I. Manas-Zloczower, "Flow field analysis of an intermeshing counter-rotating twin screw extruder", *Polymer Engineering and Science,* **34**, 551, 1994.

30. http://www.scprod.com/product_bulletins/PB%20Cloisite%2020A.pdf.

31. Wang KH, Choi MH, Koo CM, Choi YS, Chung IJ, "Synthesis and characterization of maleated polyethylene/clay nanocomposites", *Polymer*, **42 (24)**: 9819, 2001.

32. Ryu S. H., Chang Y. W., "Factors affecting the dispersion of montmorillonite in LLDPE nanocomposites", *Polymer Bulletin*, **55**, 385, 2005.

33. Zhang M. Q., Sundararaj U., "Thermal, rheological, and mechanical behaviors of LLDPE/PEMA/Clay nanocomposites: effect of interaction between polymer, compatibilizer, and nanofiller", *Macromolecular Materials and Engineering,* **291**, 697, 2006.

34. Turi, E., "Thermal Characterization of Polymeric Materials", 2nd Ed., Academic Press, San Diego, CA , pp.277-279, 1997.

35. Stephens, C.H, Yang H., Islam M., Chum S. P., Rowan S. J., Hiltner A., and Baer E., "Characterization of Polyethylene with Partially Random Chlorine Substitution", *Journal of Polymer Science: Part B: Polymer Physics*, **41**, 2062 2003.

36. Callister W.D., "Materials of Science and Engineering an Introduction", 6th Ed., John Wiley & Sons, New York, NY pp.495-496 , 2003.

CHAPTER 4

EVALUATION AND MODIFICATION ON A
NEW MINIATURE MIXER-APAM

4.1. Introduction

The Alberta Polymer Asymmetric Mini-mixer (APAM) was developed by researchers from our group [1] and geometrically consists of a unique, asymmetric-shaped rotor fitted within a heated cup, resulting in a varying clearance between the tips of the rotor and the barrel wall. The small gap in the mixer provides a very high shear stress zone and the varying gap distance promotes folding and reorientation of polymer melt. The mixer requires only a small amount of material, ca. 1-1.5g. APAM has been proved to be effective in producing well dispersed polymer blends [1-3] and been used for making small amounts of polymer nanocomposites [4] and testing new mixing protocols [5].

In this chapter, we further investigate the effect of the rotation speed on morphology development of polymer blends and nanocomposites mixed by APAM. This is done by evaluating morphologies for non-reactive polymer blends, reactive polymer blends, polymer nanocomposites, and simulation results for key processing and mixing parameters.

Due to the high cost and long time required, it is impractical to use only experimental methods to test APAM. The complex geometry of the mixer also prohibits us from using analytical methods. Therefore, numerical simulation is an alternate approach that was efficient and economical to optimize the processing

equipment design. In previous work for static mixers, Yao and Manas-Zloczower [6] investigated the influence of design on the mixing performance using numerical simulation. Similarly, Heniche et al. [7] studied the effects of blade shape on static mixing. Regalia [8] applied numerical methodology to design new tangential rotors for internal mixers. Wang and Manas-Zloczower [9] used several mixing indexes to characterize the scale-up of a single screw extruder. Dhanasekharan [10] performed a non-isothermal simulation to scale up a extrusion process for wheat dough. Other work by Ishikawa [11] numerically analyzed the effects of the screw clearances on dispersive mixing for a twin screw extruder.

To meet different capacity requirements and to supply enough materials for characterization and mechanical testing, alternate designs of the APAM are needed. The simplest way to have a larger capacity is to increase the radius of the outer cup while keeping the size of the rotor fixed. This modification will increase the clearances between the tips of the rotor and the cup wall. Another common way is to scale each mixer dimension. Both methods will change the geometric structure of the mixer and affect the mixing performance.

The tip clearance refers to the narrow region between the tips of the rotor and the barrel wall and determines the maximum shear stress that the mixer can apply. The smallest tip clearance inside a mixer generally produces the highest shear stress being applied on materials. On the other hand, the narrowest region only allows a small amount of material to pass through, which prevents material from being well mixed and homogenous. The high shear rate in a tip clearance that is

too narrow may cause relatively high temperature in the local area due to viscous heating. A suitable tip clearance must be small enough to generate high enough stress to break up droplets or agglomerates and yet large enough to allow a fair amount of material to pass through.

In this paper, we use Polyflow 3.9, a finite element method (FEM) based software, to investigate the changes in flow and thermal fields with increasing tip clearances inside APAM.

4.2. Mixer design and Computational method

APAM is composed of an asymmetric rotor and a cylinder cup. The detailed geometric information about the rotor is contained in a previous publication [1]. Figure 4.1 shows a cross-section of APAM with the varying clearances and photography of APAM. The height of the outer cup is 25mm and the radius of the cup is 6.5mm.

Figure 4.2 illustrates the modification plan. The derivatives of APAM, APAM_APAM_Rev1 and APAM_APAM_Rev2, were obtained by increasing the radius of the outer cup from 6.5mm to 6.75mm and 7mm respectively while keeping all other dimensions same as the original APAM. As a result, the tip clearances of APAM_Rev1 and APAM_Rev2 increase to 0.5mm and 0.75mm respectively.

(a)

(b)
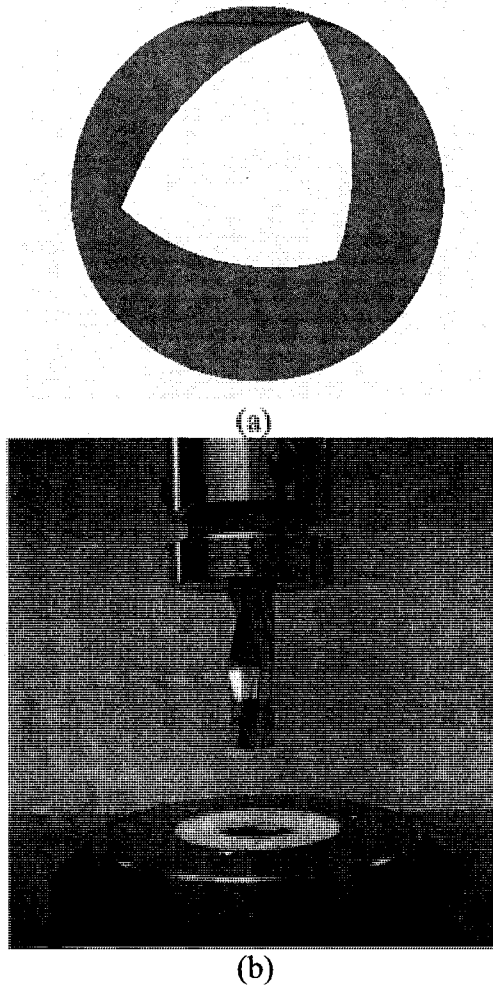
Figure 4.1: Photograph of APAM mixer: (a) Cross-section of the mixer showing the varying clearances; (b) Photograph of APAM.
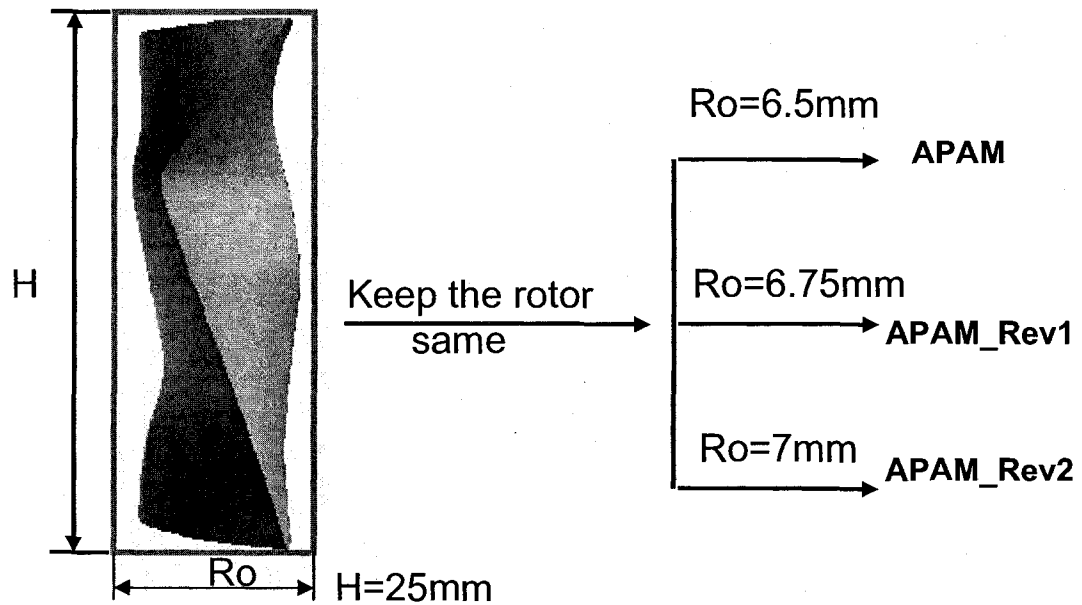
Figure 4.2: Illustration of APAM modification.

To compare the results from these mixers more easily, a dimensionless axial distance (z-axis) is defined as the ratio of the distance from the top to a particular position over the height of the mixer.

Gambit 1.3 was used to generate the meshes of the geometries. The mesh is composed primarily of tetrahedral mesh elements with small amount of hexahedral, pyramidal, and wedge elements where appropriate. The mixers' volume, minimum clearance size and total number of mesh elements are listed in Table 4.1.

Table 4.1: Summary of simulation set up.

	R_i/R_o	Volume (mL)	Minimum gap size (mm)	No. of elements
APAM	0.9615	2.2	0.25	45461
APAM_Rev1	0.9259	2.4	0.5	60055
APAM_Rev2	0.8928	2.7	0.75	65731

The governing equations of continuity, motion and energy were solved numerically using the finite element code, Polyflow3.9 from Fluent Inc. The rotating reference frame method is used in the modeling such that the barrel is rotated clockwise at 50 rpm and the irregular rotor is static. In this way, the numerical mesh is fixed with time and no mesh superposition technique is required. Non-slip boundary conditions are used at the solid surfaces in our simulations for all mixers. For all mixers, the cup wall is set at a constant temperature of 463 K and the rotor is assumed to be insulated. All simulations are performed using the same material properties and under the same processing conditions.

The Generalized Newtonian model is used to characterize the viscous behavior of polystyrene:

$$\eta(\dot{\gamma}, T) = \eta(\dot{\gamma})G(T) \tag{4.1}$$

where $\eta(\dot{\gamma})$ is the viscosity at a reference temperature of 190°C:

$$\eta(\dot{\gamma}) = 8357.8\left[1 + (0.3347\dot{\gamma})^{0.6686}\right]^{\frac{0.3215-1}{0.6686}} \tag{4.2}$$

and $\dot{\gamma}$ is shear rate.

The temperature effect was characterized by approximate Arrhenius law:

$$G(T) = \exp[-0.06466(T - T_a)] \tag{4.3}$$

where T is the temperature and T_a is the reference temperature, which is 190°C in our case. No elastic effect is considered in this model.

The simulations were performed on an IBM RS/6000 Power 4 workstation with 8GB memory.

4.3 Experimental

4.3.1 Materials

The polymers and nano-filler used for this study are described in Table 4.2.

Samples of polymers blends were prepared to evaluate the mixing performance of

APAM.

Table 4.2: Polymer and nano-filler used in experiments.

Material (Abbreviation)	Source (Trade name)	$M_w \cdot 10^{-4}$ (g/mol)	Density (g/cc, 25°C)
Polystyrene (PS)	Dow Chemical (Styron 666D)	16	1.05
Polystyrene-5% maleic anhydride (PSMA)	Arco	Not available	Not available
Polyamide (PA)	DuPont (Zytel330)	Not available	Not available
Polyethylene: low variance in MW-PE (HDPE)	Nova PE (SP Sclair 2907)	Not Available	0.96
5% Maleic Anhydride Grafted Polyethylene (PEMA)	Dupont (Fusabond 2650)	4.84	0.73
Montmorillonite Clay (C20A)	Southern Clays (Cloisite 20A)	Not available	1.77

4.3.2 Mixing and characterization

The compositions, mixing temperature, and rotational speeds of polymer

blends and nanocomposites are given in Table 4.3. The APAM mixer was used to

mix polymer blends and nanocomposites under different rotational speeds.

Table 4.3: The compositions of polymer blends and nanocomposite with mixing conditions.

Compositions	Composition Ratio	Temperature ($^{\circ}$C)	Rotation speed (rpm)
PS/PA	80/20	200	50 100 150
PSMA/PA	80/20	200	50 100 150
HDPE/C20A	95/5	200	70 100 150
PEMA/C20A	95/5	200	70 100 150

A small amount of each nanocomposite sample was hot pressed to a 25 mm discs for XRD measurements. The techniques for TEM and XRD were described in Chapter 3.

4.4. Results and discussion

4.4.1 Morphology change with rotation speed for APAM

Figure 4.3 shows the variation in morphology of uncompatibilized PS/PA blends with different rotational speeds after 10 minutes of mixing. At the lowest rotational speed used, 50 rpm, although most of the dispersed particles are spherical, some unstable shapes are also present. For example, the drops at the top center of the micrograph in Figure 4.3a are breakup. This result indicates that the steady state morphology was not reached after 10 minutes of mixing at 50rpm.

Under the same processing conditions and mixing time, the number of unstable

shapes seen in samples processed in an internal batch mixer is much less [12].

(a)   (b)

(c)
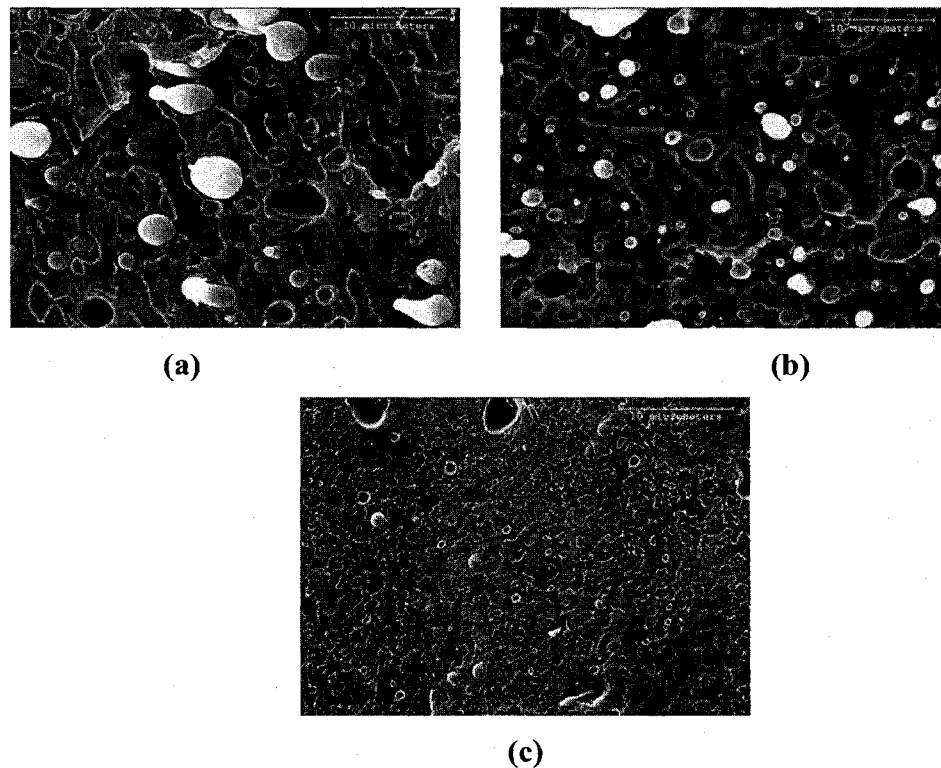
Figure 4.3: Morphology variation of PS/PA (80:20) with different rotational speeds after 10 minutes mixing at 200°C: (a) 50 rpm; (b) 100 rpm; (c) 150 rpm.

For the same polymers under the same processing conditions, Breuer et al [1]

also found the co-existence of spherical, ellipsoidal and cylindrical phase

morphology after 10 minutes mixing in APAM at 100 rpm. But in our case, we

found that the unstable shapes are almost non-existed after 10 minutes mixing at

100 rpm. By increasing the rotational speed, the dispersed phase became finer

and the unstable shapes disappeared. Although the structure is much finer at 150

rpm, a few lager particles are still observed. Up to 150 rpm, we did not see any

extended structure due to the rotation speed increase.

Figure 4.4 shows the morphology variation in the reactive PSMA/PA blend using different rotational speeds. PSMA is a styrene-maleic anhydride (MA) copolymer with 5wt% content of MA. During mixing with PA, the MA groups in PSMA chemically reacts with the amine groups from PA, and stabilizes the interface between the two phases. So the PSMA/PA blend (Figure 4.4) has a much finer structure compared to the PS/PA blend (Figure 4.3). According to Sundararaj et al [13], the size of the dispersed phase for a similar reactive system mixed by an internal batch mixer is independent of the dispersed phase concentration and the average size of the dispersed particles is about 0.2 micron. In our case, the size of the dispersed particles is slightly larger but on a similar scale. The morphology does not change much with increasing rotational speed.

(a)

(b)

(c)
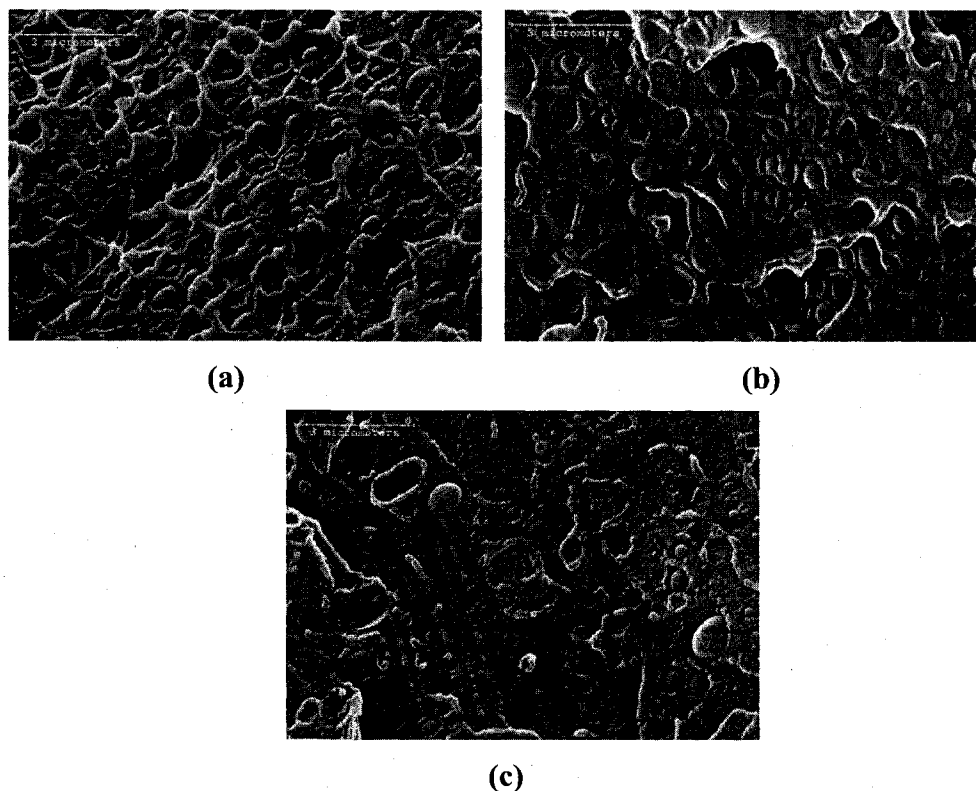
Figure 4.4: Morphology change of PSMA/PA (80:20) with different rotational speeds: (a) 50 rpm; (b) 100 rpm; (c) 150 rpm.

Since this small scale mixer was mainly designed for mixing polymer nanocomposites, the PE/C20A and PEMA/C20A systems were used to test the effect of the rotation speed on polymer/nano-clay mixing in APAM. The C20A is an alkylammonium modified montmorillonite and has a larger d-spacing than unmodified montmorillonite. Because of PE's low hydrophilicity, melt-mixed PE/Clay nanocomposites often exhibit no increase in d-spacing or perhaps only slight intercalation. Figure 4.5 shows the XRD patterns of the C20A and the PE/C20A nanocomposites with different rotational speeds. As expected, no exfoliation is indicated by the XRD pattern of the PE/C20A nanocomposites mixed by APAM with rotational speeds up to 150 rpm. The inter-layer spacing of the C20A increases slightly with the rotational speed. The d-spacing change with rotational speed is summarized in Table 4.4.
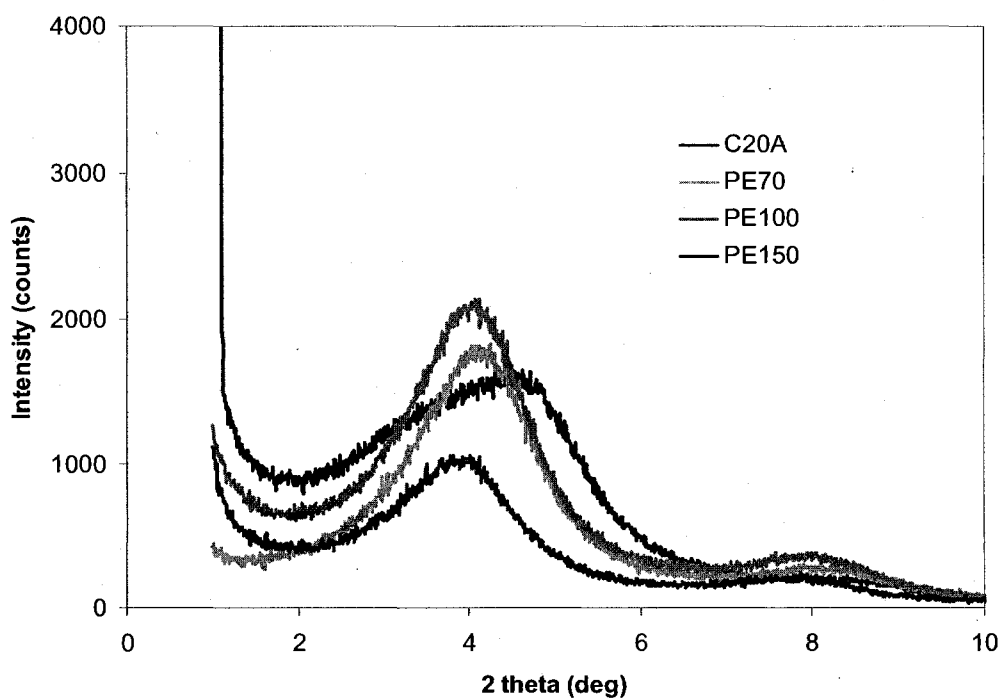
Figure 4.5: XRD Patterns of C20A and PE/C20A (95:5) nanocomposites prepared at different rotational speeds (70, 100 and 150 rpm).

Table 4.4: The change of C20A's d-spacing in PE with rotation speed.

	C20A	70 rpm	100 rpm	150 rpm
2θ (deg)	4.6	4.26	4.12	4.03
d (nm)	2.23	2.41	2.49	2.54

Figure 4.6 shows the morphology change of the PE/C20A nanocomposites with increasing rotational speed. At 70 rpm, most of the silicate layers are stacked together as shown in the upper left corner of Figure 4.6a. The diameter of the larger stacks is about 100 nm. Although no exfoliation is shown up to 150 rpm, the average size of the stacks decreases with increasing speeds.

(a)

(b)

(c)
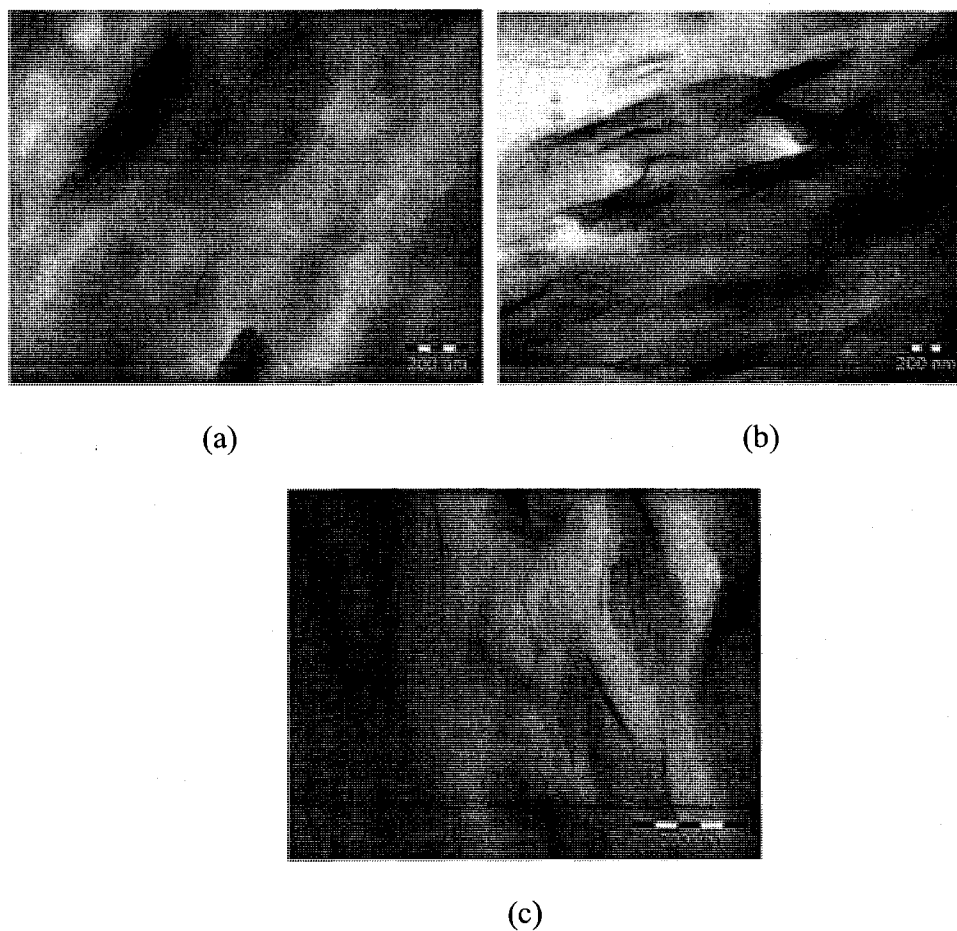
Figure 4.6: Morphology change of PE/C20A (95:5) with different rotational speeds: (a) 70 rpm; (b) 100 rpm; (c) 150 rpm.

PEMA has maleic anhydride groups incorporated along the polyethylene chains and this should increase the compatibility between the hydrophobic polyethylene and the hydrophilic silicate surface [14-17]. The HDPE modified with 5 wt% of maleic anhydride was mixed with C20A by direct melting mixing in APAM. Figure 4.7 shows the TEM images of PEMA/C20A with different rotation speeds.

(a)

(b)

(c)
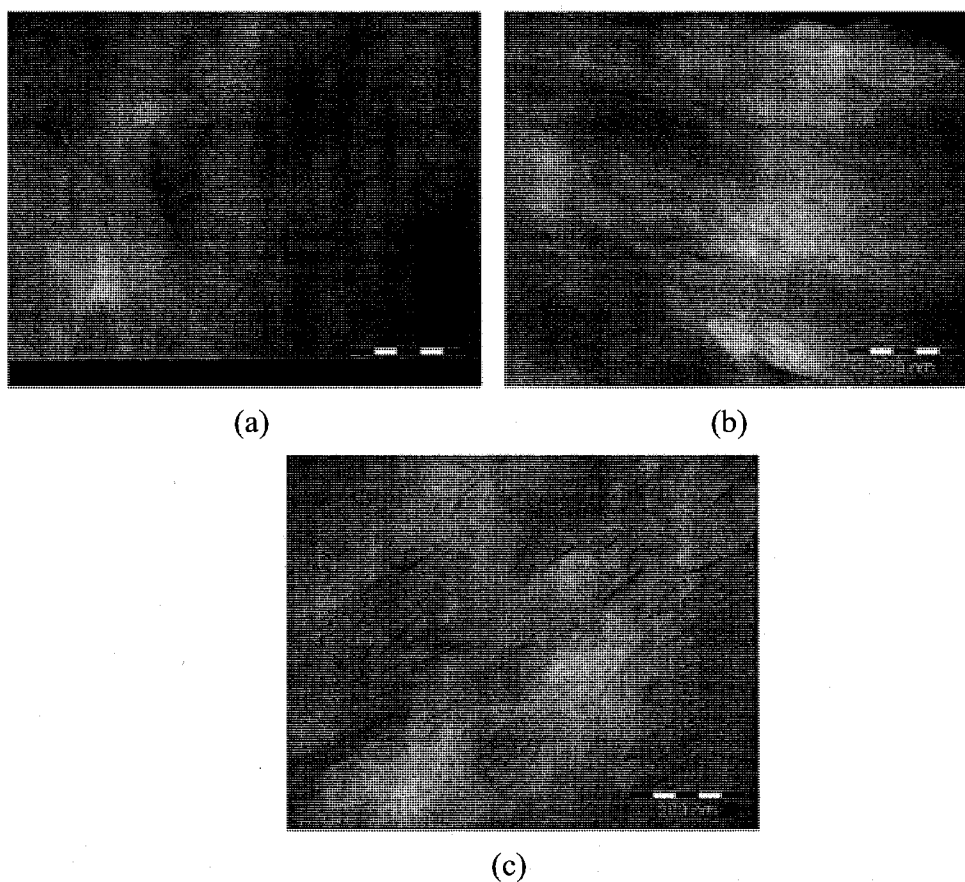
Figure 4.7: Morphology change of PEMA/C20A (95:5) with different rotational speeds: (a) 70 rpm; (b) 100 rpm; (c) 150 rpm.

Figure 4.8 shows the XRD patterns of the same nanocomposites. PEMA/C20A exhibits a combined intercalation and exfoliation at 70 rpm and 100 rpm. At 150 rpm, C20A is almost completely exfoliated through the PEMA matrix.
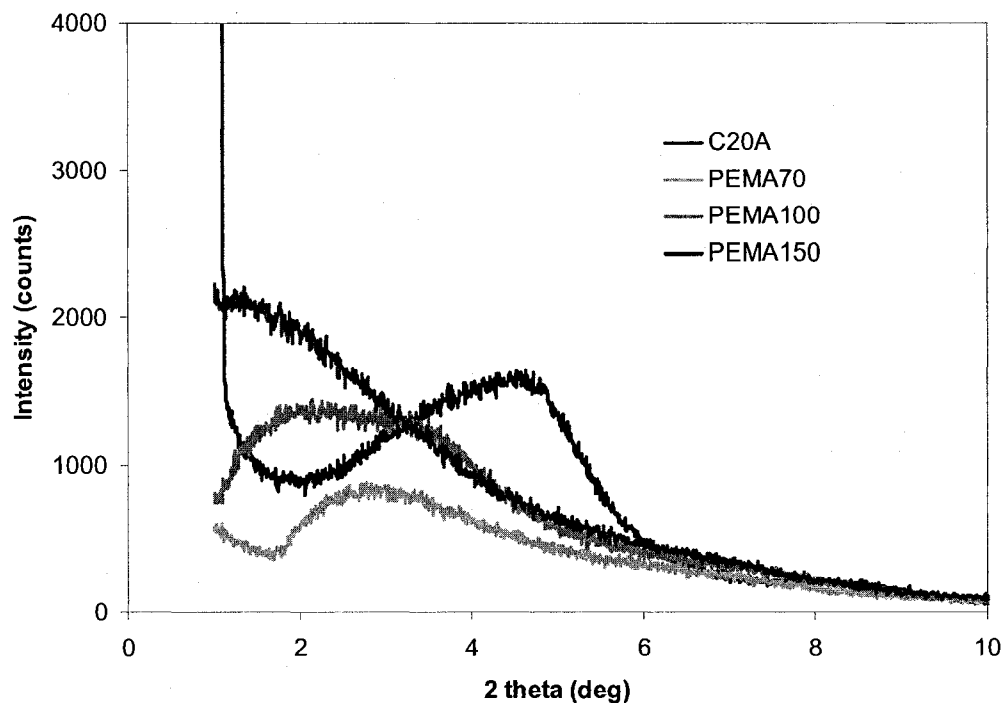
Figure 4.8: XRD patterns of PEMA/C20A (95:5) at different rotational speed (70, 100, 150rpm).

4.4.2 Shear rate and MI change with rotational speed

The average shear rate of APAM is 32 s^{-1} at a rotation speed of 50 rpm. Figure 4.9 shows that a relatively large portion of shear rate is around 10 s^{-1} and appears in the area near the rotor. With its asymmetric rotor design, APAM has three different clearances between the tips of the rotor and wall. With the varying clearance along the rotor axis, the shear rate in this region also varies over a wide range. The maximum shear rate appears in the smallest gap and is already more than 200 s^{-1} at 50 rpm. The high shear rate in the narrow gap allows the liquid drops or solid aggregates to be broken up when they pass through this region, producing a finer dispersion. Local shear rate is around 30 s^{-1} in the intermediate

gap and 20 s^{-1} in the largest gap. Figure 4.9 a, b and c show that the average shear rate of APAM increases linearly with rotational speeds.
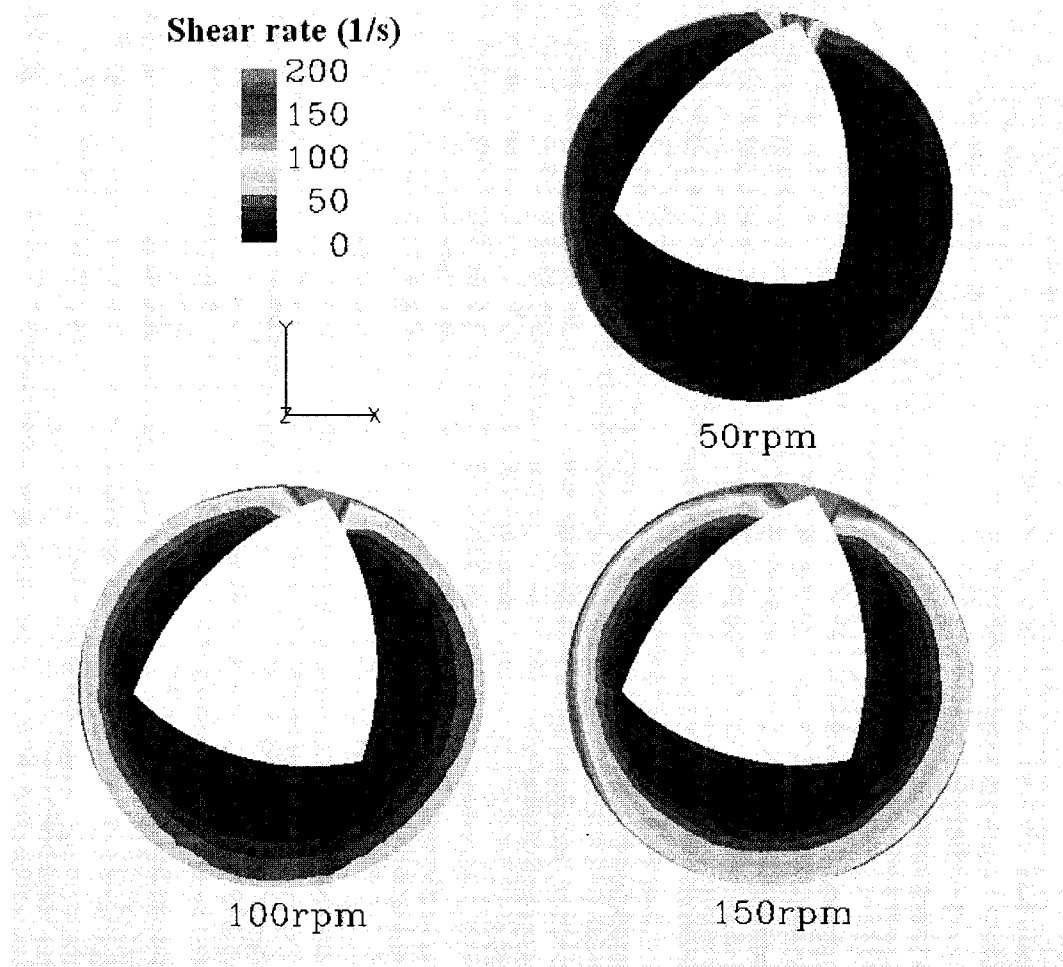
Figure 4.9: The shear rate distribution with rotational speeds: (a) 50rpm; (b) 100rpm; (c) 150rpm.

As defined in equation 3.1, mixing index (MI) is another important factor to characterize dispersive mixing. In Chapter 3, it was shown that MI is zero for pure solid rotation, one for elongational flow and 0.5 for shear flow. Figure 4.10 shows MI distributions of APAM at one particular cross-section for different rotational speeds. The distribution of flow patterns inside APAM does not change with rotational speeds. Overall, shear flow (MI = 0.5) is dominant in

APAM and there is not much elongational flow. This explains that the morphology (Figure 4.3a) of PS/PA blend mixed by APAM shows slightly more unstable shapes than what was seen in the morphology (Figure 3.18b) of the same blend processed by MBM. This is despite the fact that APAM has a larger average shear rate and a larger maximum shear rate than MBM.
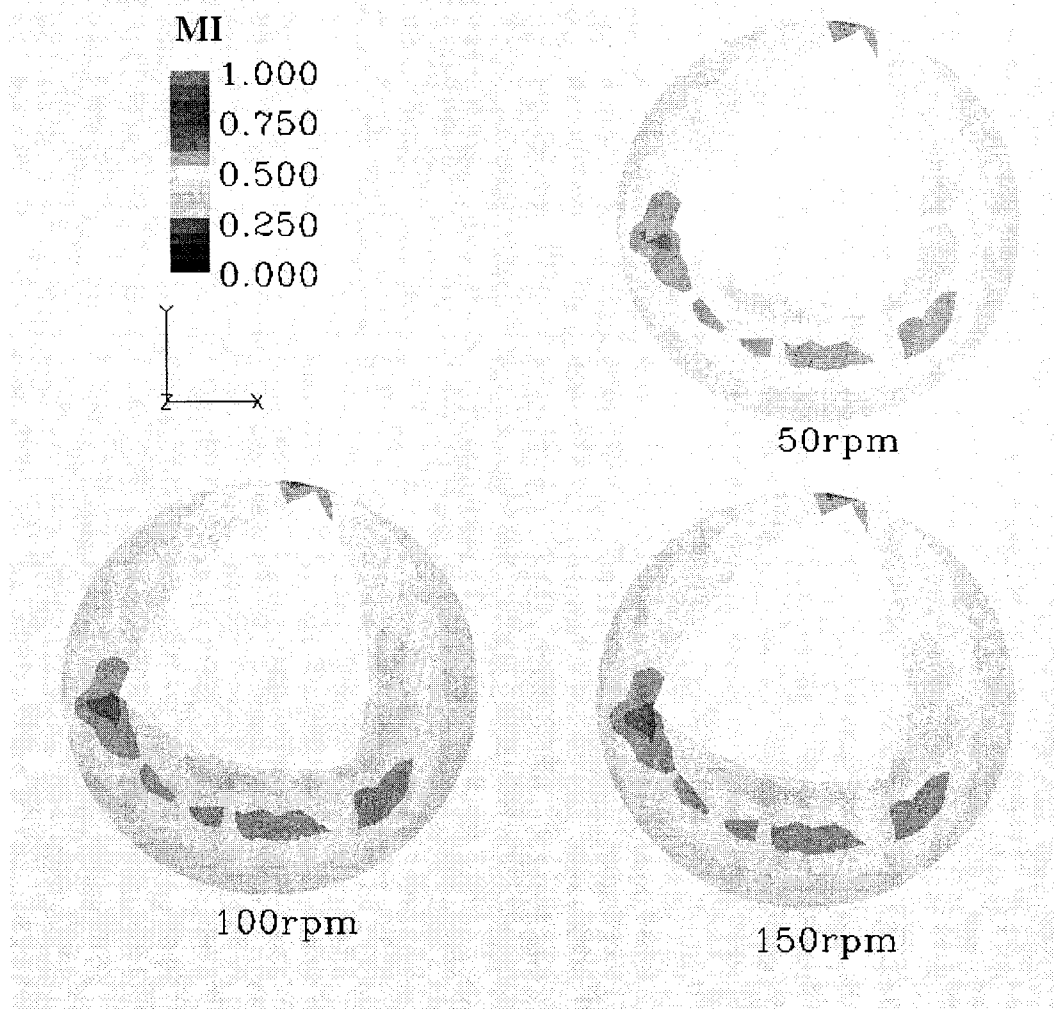
Figure 4.10: The mixing index (MI) distribution with rotational speeds: (a) 50 rpm; (b) 100 rpm; (c) 150 rpm. MI is 0 for solid rotation, 0.5 for shear flow and 1 for elongational flow.

4.4.3 Non-isothermal modeling of APAM

Figure 4.11 shows the radial velocity component of APAM at a typical cross section along z-direction from the top view. The velocity magnitude is represented by both the size of the arrows and by the color scale. G1, G2 and G3 represent the three small gaps between these tips of rotor and barrel wall with increasing distance. G1 is the smallest gap and G3 is the largest one while G2 is in between. The flow mainly rotates along the rotor with a small amount of axial flow. We find that relatively large velocity appears near the asymmetric rotor and goes to zero at the wall, where shear flow dominates the whole flow domain.
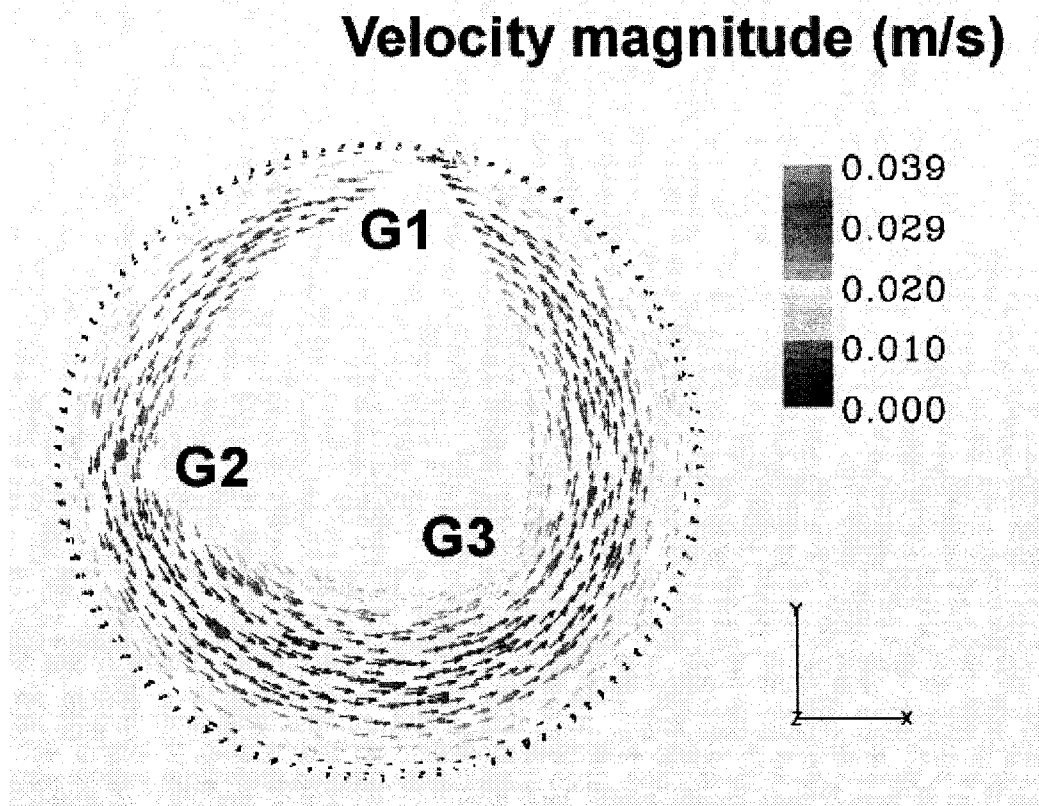
Figure 4. 11: Velocity profiles of APAM in a typical axial cross-section. Both the arrow size and the scale legend bar show the velocity magnitude; G1: the smallest gap; G2: the intermediate gap; G3: the largest gap.

As a comparison, the velocity contours of the APAM, APAM_Rev1 and APAM_Rev2 are shown in Figure 4.12. The magnitude of the velocity in the flow domain of APAM_Rev1 and APAM_Rev2 decreases with increasing tip clearances. All of the mixers have a very similar velocity profile except for the velocity magnitude.

Velocity (m/s)

APAM

0.040
0.030
0.020
0.010
0.000

Rev1

0.039
0.029
0.019
0.010
0.000

Rev2

0.037
0.028
0.019
0.009
0.000
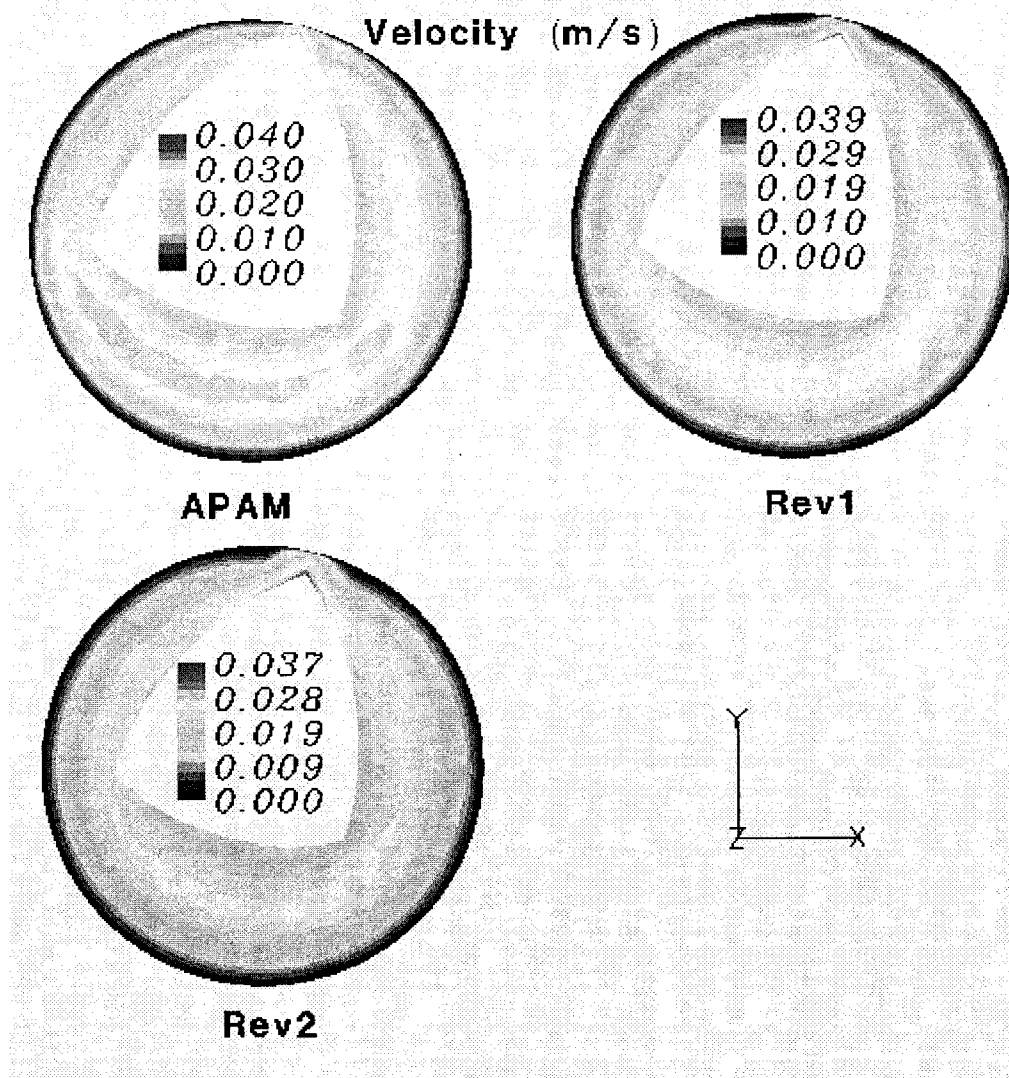
Figure 4.12: Velocity profiles of APAM and its derivatives.

The axial component of velocity inside the mixers is shown in Figure 4.13. The irregular shape of the rotor creates the axial flow in the narrow region

between the rotor and wall. These figures show the perspectives of the axial flow

distribution in the shells located between the tips of the rotor and the barrel wall.

We can see the magnitude of the axial velocity is much smaller compared to the

radial one and that most of the axial flow is focused along the minimum clearance.

Due to the configuration of the rotor, the flow in the top part of the mixer is

mainly upward along the minimum clearance while the flow goes down in the

surrounding area; and the flow in the lower part along the minimum clearance is

mainly downward with the flow in the surrounding area and the bottom going up.

These axial flows allow for reorientation in the axial direction.
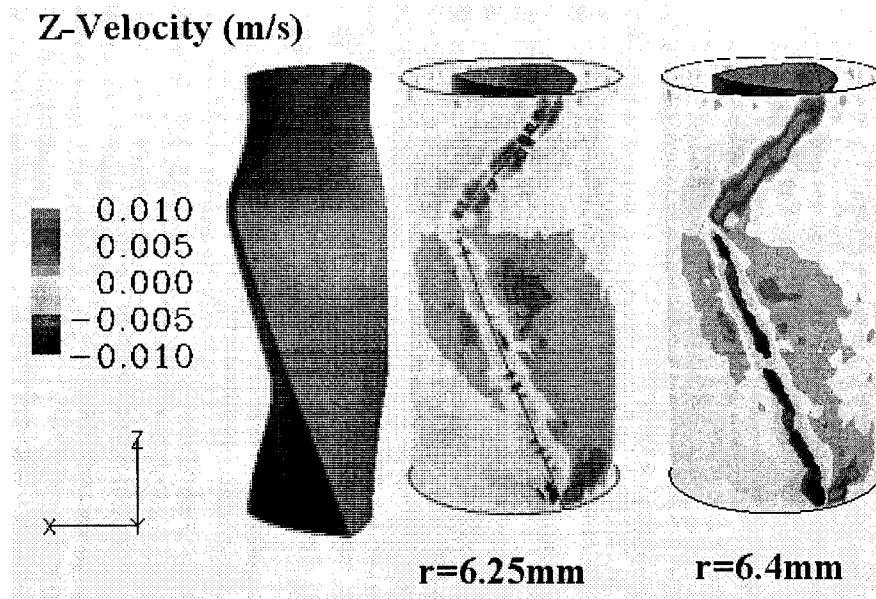
(a) APAM

Figure 4.13: Velocity contours at the iso-surface are scaled by z-component of the velocity (m/s) for different barrel radii: (a) APAM; (b) APAM_Rev1; (c) APAM_Rev2. The coordinate origin is set at the center of the mixer and the iso-surface function is $x^2 + y^2 = r^2$.

r=6.25mm   r=6.5mm   r=6.7mm

(b)

r=6.25mm   r=6.5mm

r=6.75mm   r=6.9mm
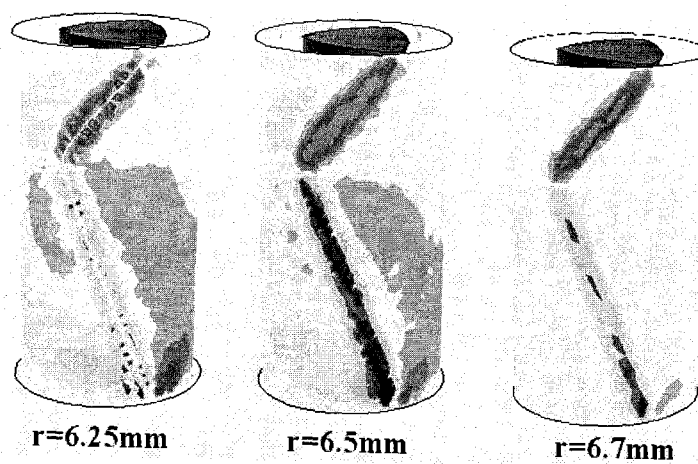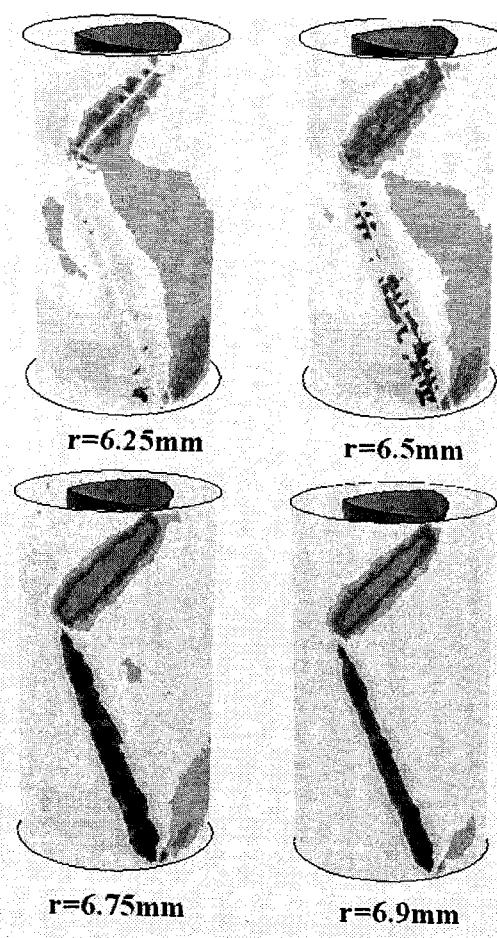
(c)

Figure 4.13 (Continued).

In batch mixers, axial flow is important because it creates reorientation which promotes uniform mixing. As illustrated in Figure 4.14, the axial flow exists in the narrow region between the rotor and the mixer wall. For batch mixers, the net axial flow is always zero because the system is closed. However, we may use the axial flow intensity across the radial plane to identify the axial mixing intensity inside the mixers. To calculate the amount of axial flow at each time step, the axial flow percent (%) (AFP) is defined as:

$$AFP = \frac{\int |V_z| dA_{xy}}{V} \times 100\%$$

(4.4)

where V_z is the axial component of velocity, A is cross sectional area perpendicular to the axial or z-direction, and V is the total volume of the mixer.
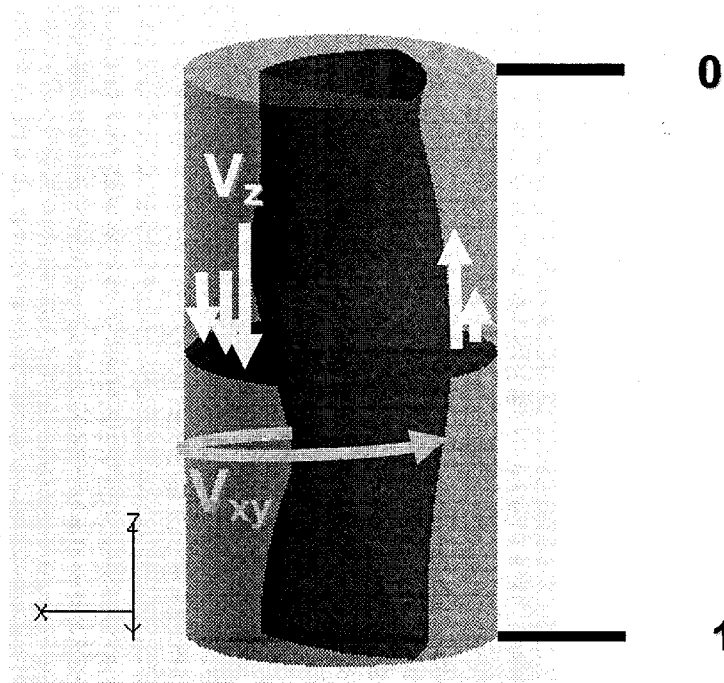
Figure 4.14: Illustration of the calculation of AFP.

The results for all mixers are plotted in Figure 4.15. In batch mixers with a single rotor, most of the flow is tangential and axial flow occurs only where the clearances change. The amount of the axial flow is proportional to the ratio of the radii of rotor and the cup. From Figure 4.15, we can see that axial flow exists in all of the mixers and varies at different locations. For all mixers, there is more axial flow in their middle part. The APAM_Rev1 and APAM_Rev2 modifications of APAM increases the gap distances between the tips of the rotor and the cup wall; therefore this decreases the amount of the axial flow rate.
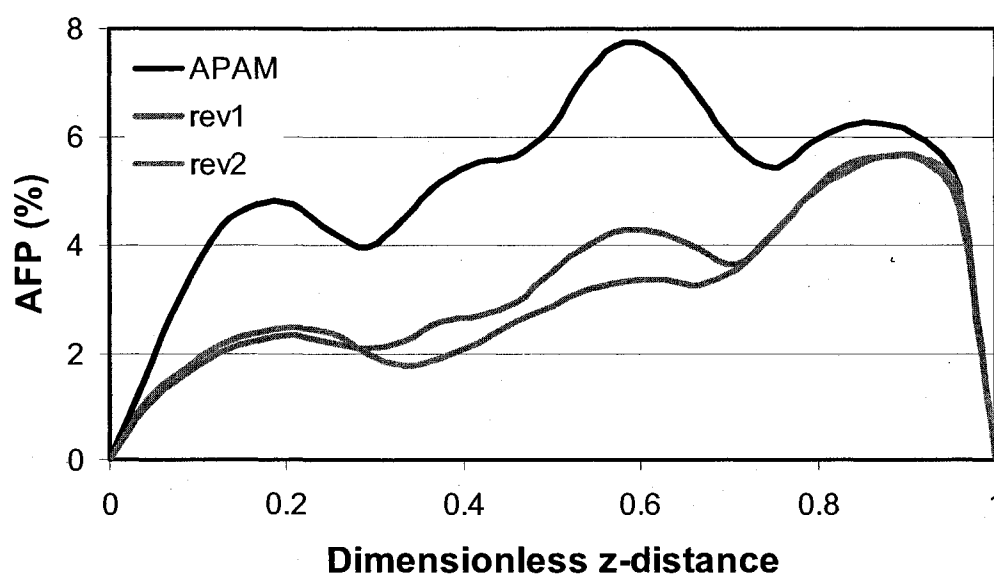
Figure 4.15: The percentage of the axial flow rate at the cross-sections along z-direction.

4.4.4 Thermal field development

The non-isothermal process was simulated for APAM and its modified versions accounting for viscous dissipation. The heat transfer simulation in this study was carried out with polystyrene (PS) melt at an initially homogenous

temperature of 463K and with mixer barrel temperature also at 463K. The heat transfer rate q (W) across the barrel wall was calculated and plotted as a function of time as shown in Figure 4.16 a, b and c for APAM, APAM_Rev1, and APAM_Rev2 respectively. Initially the polymer melt temperature is the same as the barrel wall temperature and the heat transfer rate across the barrel wall is zero. When the mechanical energy is converted to internal energy, the melt temperature increases and consequently a temperature gradient is established and this temperature gradient becomes larger and larger with time. Due to the higher temperature of polymer melt, heat is transferred from the melt to the barrel wall. When the heat transfer rate out of the mixer equals the viscous dissipated power, a stable temperature field is set up and a thermal steady state is reached. Under the same processing conditions and using the same material, the geometry of the mixers changes the magnitude of the dissipated power and the time required to reach a thermal steady state.

As shown in Figure 4.16a, the dissipated power produced by APAM is initially 1.67 W and finally decreases to 1.57 W at thermal steady state. With a 0.25 mm increase of the tip clearance for APAM_Rev1, the generated power decreases as shown in Figure 4.16b. The power is initially 1.44 W at time zero and decreases to 1.35 W at thermal steady state. It takes about 28 s for both APAM and APAM_Rev1 to reach thermal steady state. When the tip clearance was further enlarged to 0.75mm for APAM_Rev2, the initial dissipated power decreases to 1.35 W and the steady-state power goes down to 1.13 W as shown in

Figure 4.16c. It takes about 110 s for APAM_Rev2 to reach thermal steady state, which is much longer than the time required for APAM and APAM_Rev1.
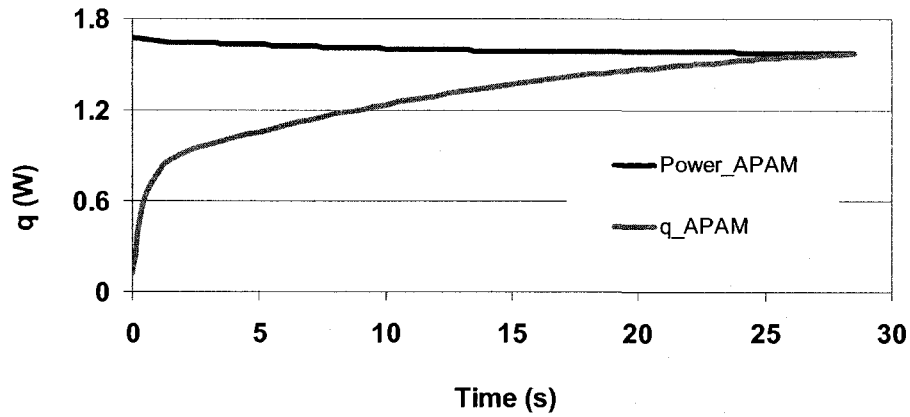
(a)
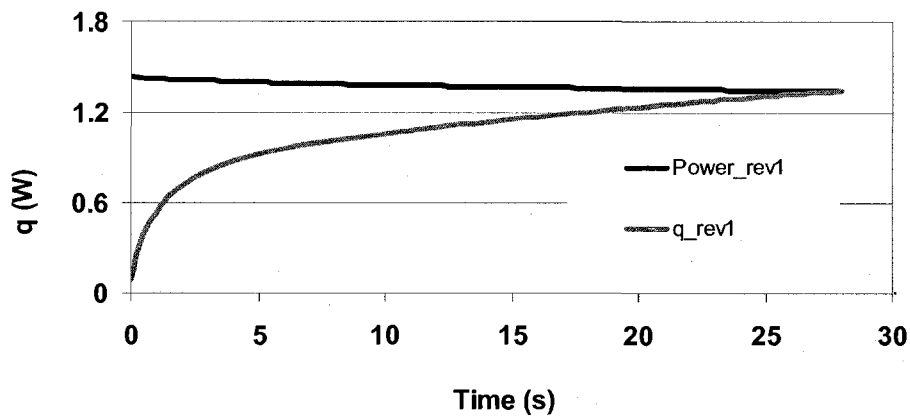
(b)
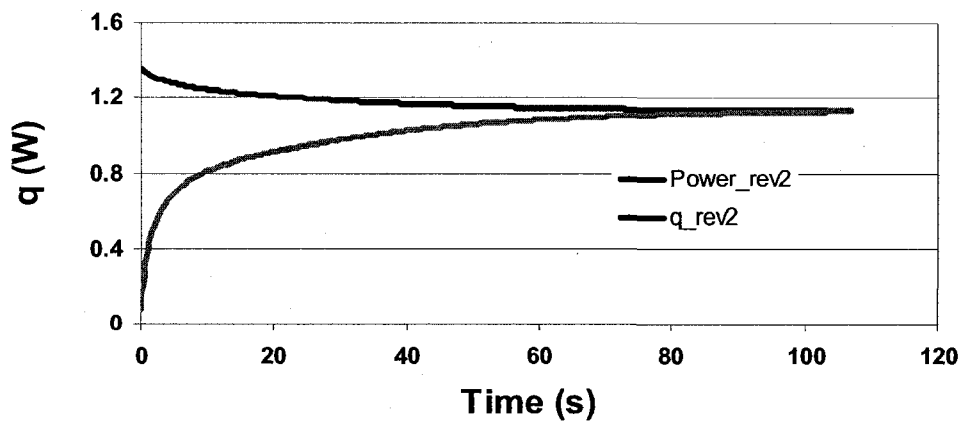
(c)

Figure 4.16: Power and heat transfer evolution for (a) APAM; (b) APAM_Rev1; (c) APAM_Rev2.

When increasing the tip clearance of the mixer by increasing the cup's radius, the volumes of APAM_Rev1 and APAM_Rev2 are slightly enlarged shown in Table 4.1. The mixers' specific generated powers at full-load capacities are calculated and listed in Table 4.5 together with the time required to reach thermal steady state. With increasing tip clearance, we can see that less mechanical power is required and it takes longer time for APAM_Rev1 and APAM_Rev2 to reach thermal steady state. The overall dissipated power is proportional to the square of the overall shear rate, therefore it requires less power for APAM_Rev1 and APAM_Rev2 to process polymer melt. On the other hand, increasing radius of the outer cup enlarges the heat transfer area and makes the temperature of polymer melt increase slowly.

Table 4.5: The total consumed time and dissipated power at thermal steady state (SS).

	APAM	APAM_Rev1	APAM_Rev2
Total time (s)	28	30	110
Volume (mL)	2.2	2.4	2.7
Specific generated power (W/g) at 0 s	0.76	0.6	0.5
Specific generated power (W/g) at SS	0.71	0.56	0.42

The APAM also depends on the natural air convection to remove the heat transferred from the polymer melt to the mixer wall. Because all of the mixers' external walls are circular cylinders, they can be treated as vertical plates if the following condition is satisfied:

$$\frac{D}{L} \geq \frac{35}{Gr_L^{1/4}}$$

(4.5)

where D is the diameter of the mixer outer wall, L is the total height and Gr_L is

the Grasgof number. Otherwise, the flat plate results should be multiplied a factor

F accounting for the curvature [18]. Based on the air properties at the average

temperature of T_w (463K) and T_∞ (298K), the Gr_L is 11400 for all of the three

mixers because they have the same height of 25mm. So to treat the walls as

vertical plates, the ratio of the diameter versus the height for each mixer should

meet the ctriteria:

$$\frac{D}{L} \geq 1.9 \tag{4.6}$$

As shown in Table 4.6, the D/L ratios for all mixers are well below 1.9. So the

external overall natural heat transfer coefficient for each mixer can be obtained by

multiplying the result from the Churchill-Chu equation (equation 2.11) with the

factor F read from ref. 10. The results are listed in Table 4.6. For all mixers, it is

Table 4.6: The overall free convection heat transfer coefficient for each mixer.

	APAM	APAM_Rev1	APAM_Rev2
D/L	0.52	0.54	0.56
F	1.16	1.17	1.18
$\bar{h}_L$	13.92	14.04	14.16
$A_s * 10^3$ (m^2)	1.02	1.06	1.1
T_w-T_∞ (K)	165	165	165
q'_natural (W)	2.34	2.46	2.57
q'_simu (W)	1.57	1.35	1.13

found that the heat removed by free convection is always much larger than the

heat transferred from polymer melt. Therefore no forced cooling is needed to keep

the wall temperature constant. Increasing radius of the mixing cup increases the external overall heat transfer coefficient and moreover less heat is generated inside the mixer due to less shear heating.

4.4.5 Transient temperature increase

Figure 4.17a-c shows the temperature distribution of the typical radial cross-section in the center of APAM (a), APAM_Rev1 (b), APAM_Rev2 (c) at three different times. The initial temperature for all mixers is 463K throughout their whole flow domain. When the rotors start to rotate, the melt temperature gradually increases. Initially, the generated energy accumulates in the region of the smallest gap because the largest shear rate occurs at this area. With time, the temperature distribution tends to be more uniform. For APAM, the average temperature increase is about 4K. There are some hot spots in APAM due to the very high shear rate in some regions followed by low shear regions where the material re-circulates. For APAM_Rev1, the temperature increases slower and takes a little longer to reach thermal steady state. Comparing APAM and APAM_Rev1, the final temperature distribution of APAM_Rev1 seems more uniform, which indicates a suitable adjustment to geometry could give a more uniform temperature distribution. However, when the radius of the mixing cup is increased further as for APAM_Rev2, the average temperature increase is much higher and takes much longer time to reach thermal steady state. Because the tip clearance of APAM_Rev2 is too large compared to the rotor radius, the velocity inside the mixer is relatively small. Although less heat is generated inside the

mixer, the slow movement of the material impedes heat convection and causes

relatively higher temperature in some areas.

(a) APAM

(b) APAM_Rev1

(c) APAM_Rev2
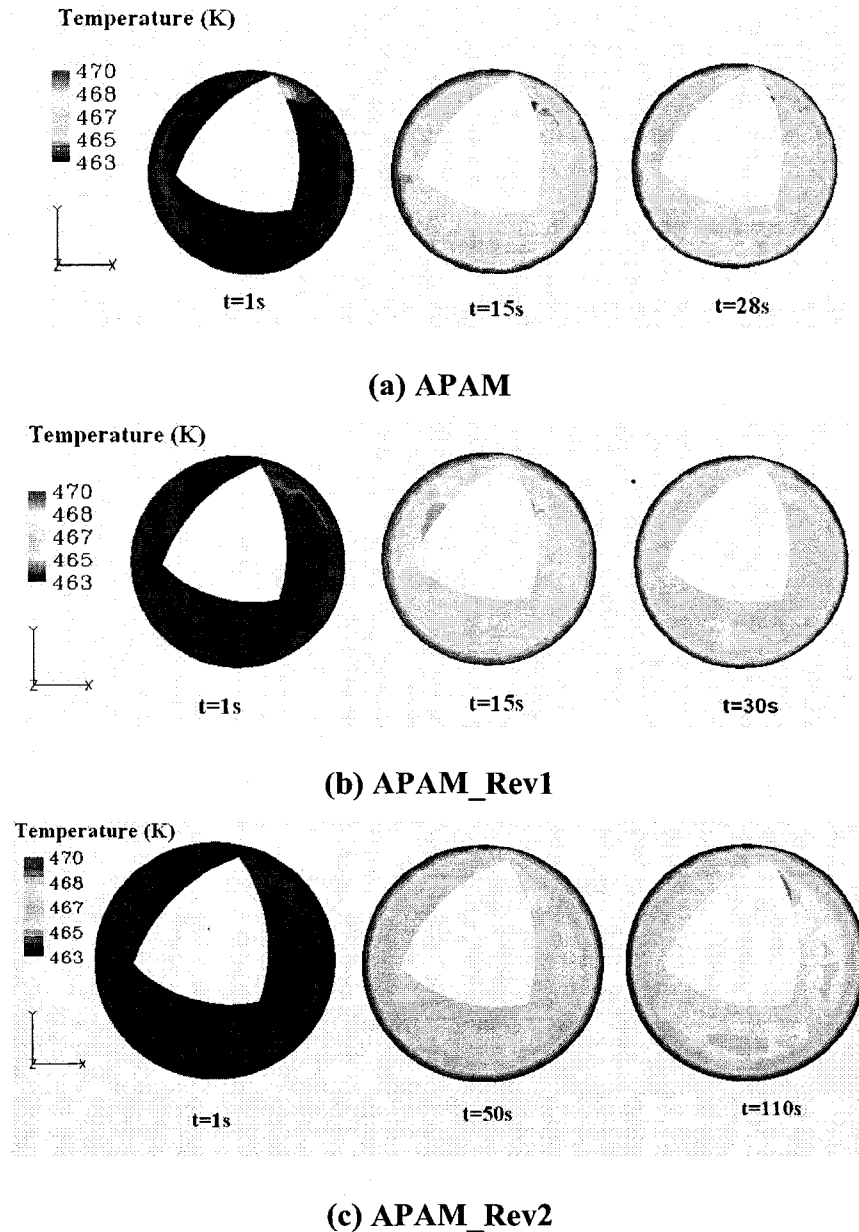
Figure 4.17: Transient temperature increases at the center cross section.

4.4.6 Area-average temperature at steady-state

To study the temperature rise due to viscous dissipation, we plot the average

temperature at a cross-section versus the dimensionless axial distance in Figure

4.18. For all mixers, the top surface along with the rotor is assumed to be insulated; therefore the highest average temperature appears near the top of the mixer and the lowest temperature goes to the pre-set boundary temperature at the bottom. The final average temperature for APAM, APAM_Rev1 and APAM_Rev2 are less than five degrees higher than the initial temperature of 463K. With slightly increased volume for APAM_Rev1 and APAM_Rev2, the average temperature increase is a little bit higher as well.
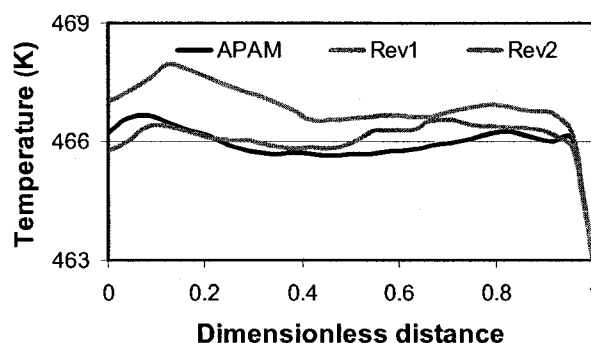
Figure 4.18: Average temperatures at cross sections in thermal steady state.

Figure 4.19 shows the heat flux at the wall as a function of circumferential distance at three different times for each of the mixers. The heat flux is calculated by the following equation:

$$q'' = \left\| -k\nabla T_{T=T_w} \right\|$$

(4.7)

The heat flux direction is perpendicular to the wall and flows out of the mixer as indicated by the arrows. Zero circumferential distance in the plot is located at the point shown on the circumference and the heat flux is plotted in the direction indicated by the arrow tangent to the circumference. For APAM, the extremely high shear rate in the minimum gap G1 results in high viscous dissipation in that area. Due to the low thermal conductivity of polymer, the generated heat cannot
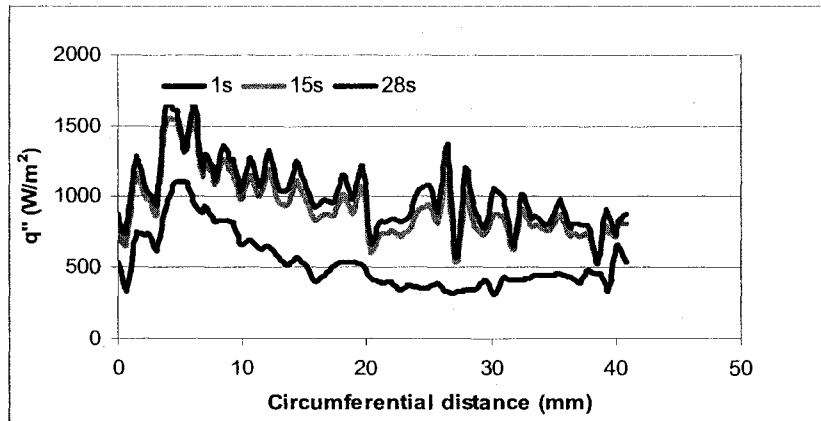
(a)
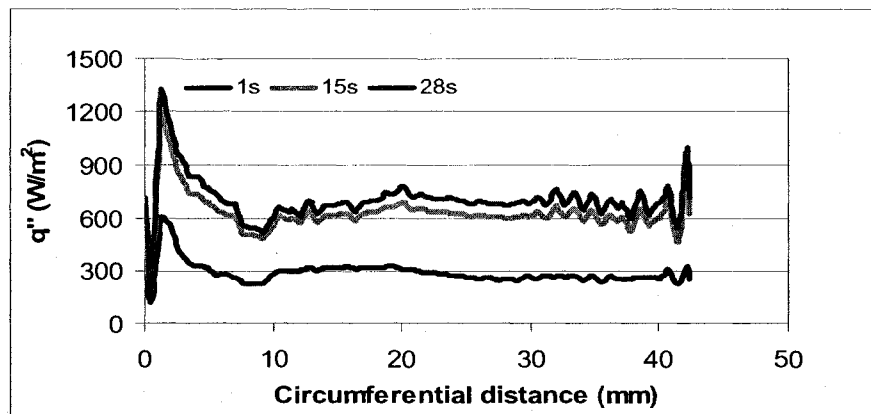
(b)
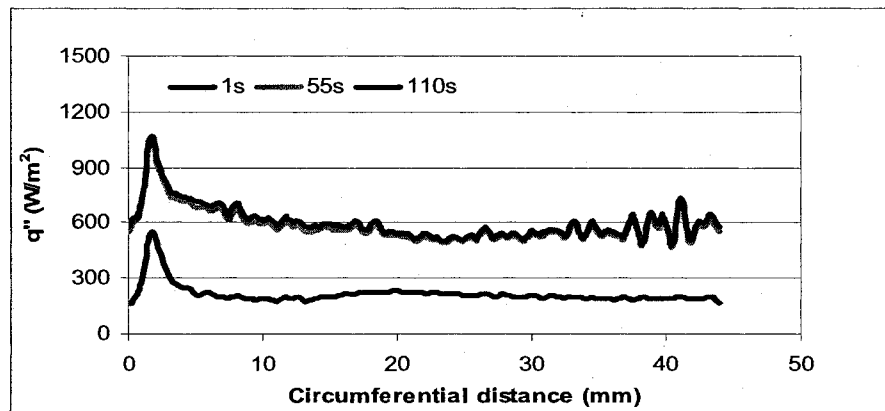
(c)

Figure 4.19: Heat fluxes across the mixer wall for (a) APAM; (b) APAM_Rev1; (c) APAM_Rev2.

be transferred out quickly and the temperature of polymer at zone G1 increases. So the heat flux in this region is always much higher than the other areas. Meanwhile, as temperature increases, the heat flux across the wall also increases. After 15 s, the heat flux does not change much with time and a thermal steady state is reached. The heat flux at the wall at thermal steady state ranges from 400 W/m2 to 1700 W/m2 depending on the position. The heat flux at different locations in APAM is more erratic than these in APAM_Rev1 and APAM_Rev2. This is partially due to the small gap that does not allow for quick heat transfer.

4.4.7 Shear rate distributions

The flow information obtained from the simulation is listed in Table 4.7. For the APAM_Rev1 and APAM_Rev2 mixers, the increased distance from the tips of the rotor to the cup wall allows more material passage and does not affect the polymer melt velocity much. Their overall average shear rate and shear stress decrease a little compared to the values of APAM.

Table 4.7: Overall flow information.

	APAM	APAM_Rev1	APAM_Rev2
Maximum velocity (m/s)	0.066	0.069	0.069
Average shear rate (1/s)	35.1	32	30.5
Average shear stress (kPa)	32.8	29	27.4

Figure 4.20 shows the shear rate space distribution at the center cross section of each mixer from a top view. Inside all mixers, only a small amount of area has a shear rate over 100s^{-1}. So the shear rate range is displayed from 0 to 100s^{-1} to

show shear rate range contours more clearly. For all cases, the highest shear rate

always appears in the minimum clearance area and the lowest one is located near

the surface of the rotor. The increased distance from the tips of the rotor to the

cup wall lowers the shear rate slightly for the modified mixers.
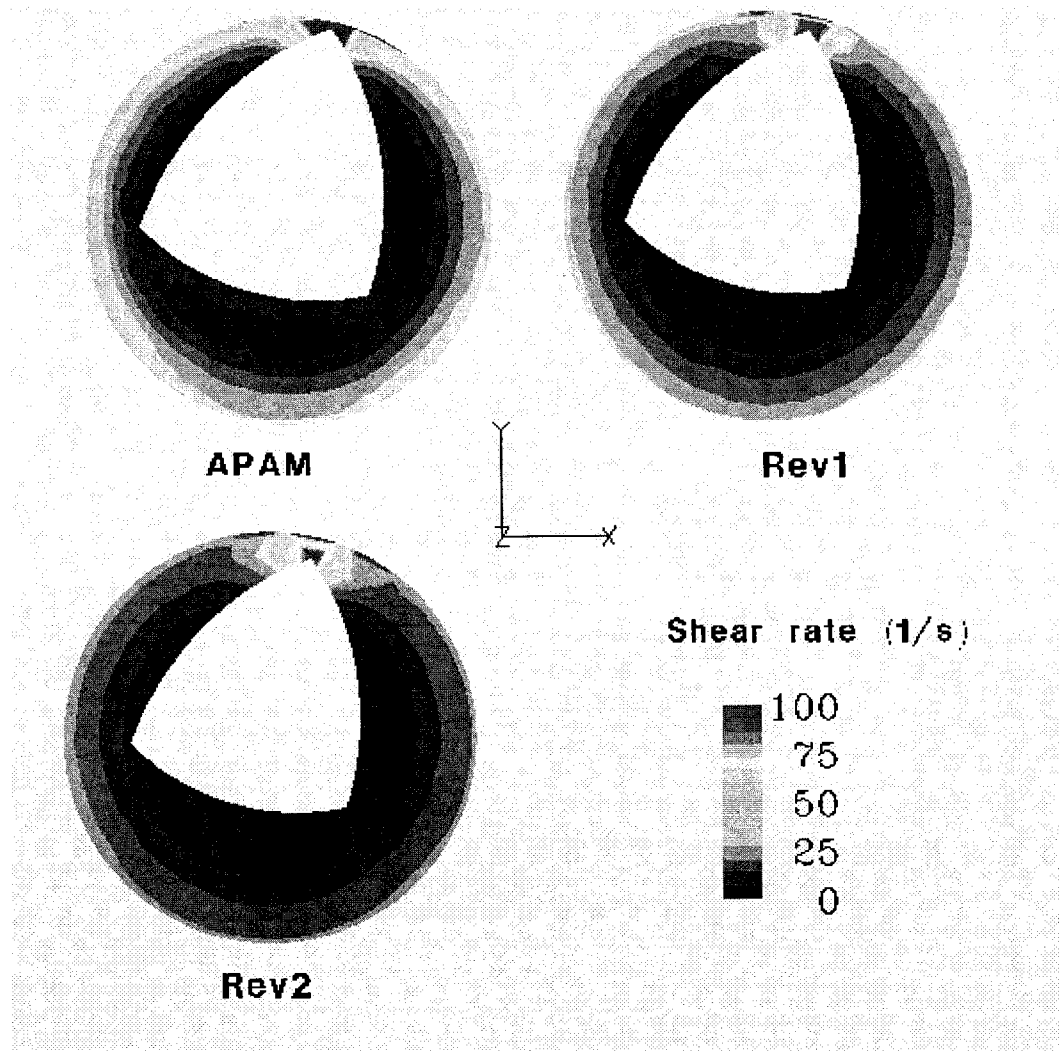
Figure 4.20: Shear rate distributions for all mixers.

One of the distinctive characteristics of the APAM is that it can produce very

high shear rate in a small mixer. There are three different gaps inside APAM: the

smallest one imposes the largest shear rate to stretch the minor component and the

larger clearances allow more materials passage and allow for relaxation and breakup of the minor component. While the overall average shear rate does not change much for the modified mixers, it is important to study how much the shear rate varies in the smallest gap area. In every cross-section along the axial direction, we found the maximum shear rate around the rotor surface and around the cup surface, and plotted them versus the dimensionless axial distance in Figure 4.21a and Figure 4.21b respectively. For all mixers, the maximum shear rate around the rotor surface oscillates but has an increasing trend along the axial direction from top to bottom and reaches the highest value near the bottom, where the rotating rotor is limitlessly close to the static bottom of the outer cup. The maximum shear rate around the rotor surface of the APAM_Rev1 and APAM_Rev2 is one half and one third respectively of its counterpart of APAM at each cross-section. For the scaled APAM, the curve of the maximum value around the rotor surface versus the axial distance is slightly higher than that of APAM. Comparatively, the maximum shear rate around the radial circumference of the outer cup does not change much along the axial direction except in the positions near the top and bottom. The increased size of the gaps does not change the maximum value around the cup surface very much compared to the effects on the maximum value around the rotor surface.
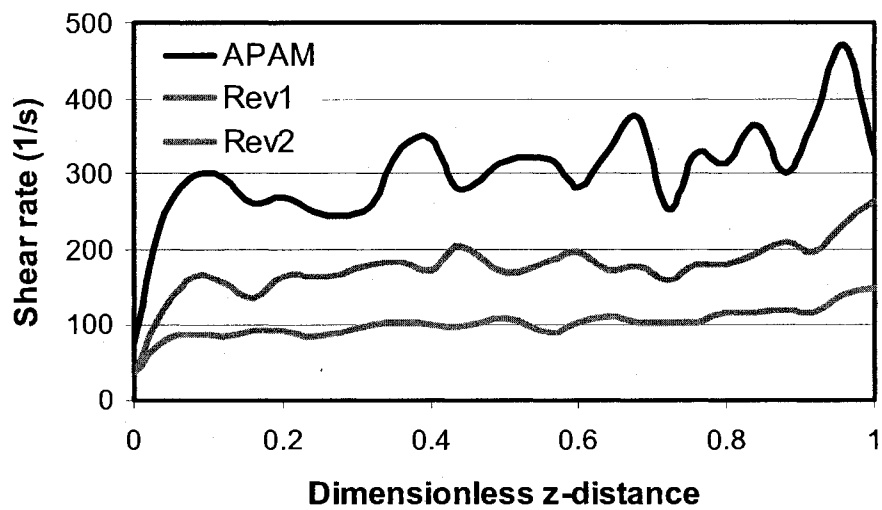
(a)
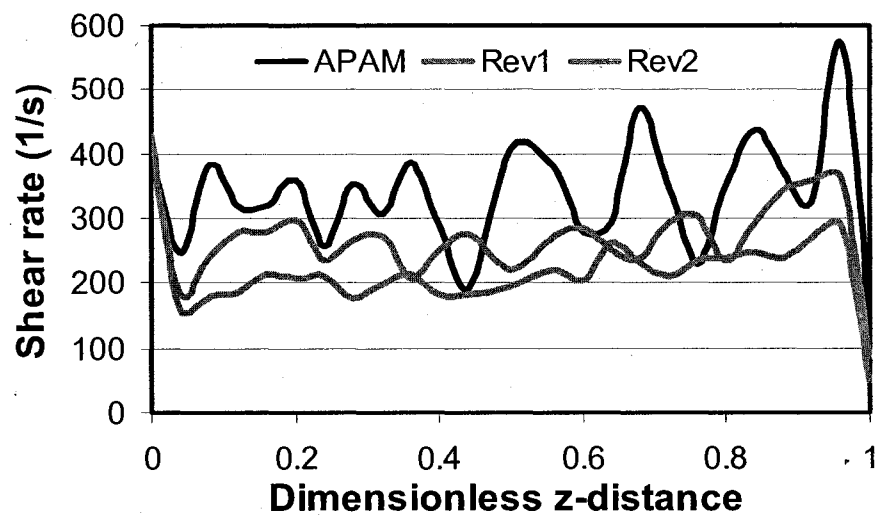
(b)

Figure 4.21: The change of maximum shear rate: (a) around the rotor surface versus axial direction; (b) the cup surface versus axial direction.

4.5 Summary

The simulation results for the revised APAM's show that shear rate and dissipated power decrease with larger gap distance. APAM_Rev1 is better than the original APAM design in that the final temperature distribution is more uniform while the overall average shear rate and velocity, and the time to steady state are similar to APAM. For all mixers, the free air convection on the external wall of the mixers is sufficient to remove the viscous heat generated in polymer melt and no extra forced cooling is needed. According to the simulation, the future scale-up design of APAM should be based on a mixer similar to APAM_Rev1.

4.6 Reference

1. Breuer, O., Sundararaj, U., Toogood R, "The Design and Performance of a New Miniature Mixer for Specialty Polymer Blends and Nanocomposites", *Polymer Engineering and Science*, **44 (5)**, 868, 2004.

2. Breuer, O., Chen HB., Lin B., Sundararaj U., "Simulation and Visualization of Flow in a New Miniature Mixer for Multiphase Polymer Systems", *Journal of Applied Polymer Science*, **97**, 136, 2005.

3. Bai Y., Sundararaj U., Nandakumar K., "CFD Study of Flow Pattern and Hear Transfer in Miniature Mixers Using a Generalized Newtonian Fluid", *SPE ANTEC Proceedings*, Boston , 409, 2005.

4. Lin B, Sundararaj U, Potschke P., "Melt mixing of polycarbonate with multi-walled carbon nanotubes in miniature mixers", *Macromolecular Materials andEengineering*, **291 (3)**, 227, 2006.

5. Lin B, Sundararaj U, Guegan P, "Effect of mixing protocol on compatibilized polymer blend morphology", *Polymer Engineering and Science*, **46 (5)**, 691, 2006.

6. Yao CH., Manas-Zloczower I., Influence of Design on Dispersive Mixing Performance in an Axial Discharge Continuous Mixer-LCMAX 40, *Polymer Engineering and Science*, **38 (6)**, 936, 1998.

7. Heniche M., Tanguy P. A., Reeder M. F., Fasano J. B., "Numerical Investigation of Blade Shape in Static Mixing", *AICHE Journal*, **51(1)**, 44, 2005.

8. Regalia R., Developments of Tangential Rotors Using Numerical and experimental Methodologies, *Plastics, Rubbers and Composites*, **34 (2)**, 59-69, 2005.

9. Wang W., Manas-Zloczower I., "Temporal Distributions: The Basis for the Development of Mixing Indexes for Scale-up of Polymer Processing Equipment", *Polymer Engineering and Science*, **41 (6)**, 1068, 2001.

10. Dhanasekharan K. M., Kokini J. L., "Design and scaling of wheat dough extrusion by numerical simulation of flow and heat transfer", *Journal of Food Engineering*, **60**, 421, 2003.

11. Ishikawa T., Nagano F., Kajiwara T., Funatsu K., "Tip clearance effect on mixing performance of twin screw extruders", *International Polymer Processing*, **21 (4)**, 354, 2006.

12. Sundararaj U., Macosko C. W., Rolando R. J., Chan H. T., "Morphology development in polymer blends", *Polymer Engineering and Science,* **32(24)**, 1814, 1992.

13. Sundararaj U., Macosko C. W., "Drop breakup and coalescence in polymer blends: the effects of concentration and compatibilization", *Macromolecules,* **28**, 2647, 1995.

14. Wang K H, Choi M H, Koo C M, Choi Y S, Chung I J, "Synthesis and characterization of maleated polyethylene/clay nanocomposites", *Polymer*, **42 (24)**, 9819, 2001.

15. Morawiec J, Pawlak A, Slouf M, Galeski A, Piorkowska E, Krasnikowa N, "Preparation and properties of compatibilized LDPE/organo-modified

montmorillonite nanocomposites", *European Polymer Journal*, **41 (5)**, 1115, 2005.

16. Liang GD, Xu JT, Bao SP, Xu WB, "Polyethylene maleic anhydride grafted polyethylene organic-montmorillonite nanocomposites. I. Preparation, microstructure, and mechanical properties", *Journal of Applied polymer Science*, **91 (6)**, 3974, 2004.

17. Wang KH, Choi MH, Koo CM, Xu MZ, Chung IJ, Jang MC, Choi SW, Song HH, "Morphology and physical properties of polyethylene/silicate nanocomposite prepared by melt intercalation", *Journal of Polymer Science Part B-Polymer Physics*, **40 (14)**, 1454, 2002.

18. Lienhard IV J. H., Lienhard V J. H., Chapter 8, *A Heat Transfer Textbook, Third Edition,* 419, 2002.

CHAPTER 5

MIXING IN MINIATURE TWIN SECREW EXTRUDER

5.1 Introduction

Mini twin-screw extruders (TSE) using several grams of material have been developed to meet the requirement of mixing polymer blends and nanocomposites on the small scale. Because of the small amount of specialty laboratory material, the mini twin-screw extruders are usually operated in batch mode. There are several commercially available small-scale TSE such as HAAKE MiniLab II (7ml, Thermo Scientific) [1], DACA MicroCompounder (5ml, DACA Instrument, Discontinued) [2], and DSM Micro-Compounder (5ml and 15ml, Xplore) [3, 4]. In spite of the size difference, all of the four mini-extruders consist of two detachable, conical mixing screws mounted inside a mixing compartment with a recirculation channel. While the HAAKE MiniLab II is installed horizontally, the DACA and DSM Micro-Compounders are installed vertically. Another widely used extruder, the PRISM PharmaLab 16 Series twin-screw compounder developed by Thermo Scientific [5] is a twin-screw extruder that operates continuously and is generally considered to be a mini extruder because it can be operated with about 250-500 g of materials while the larger extruders need 2-5 kg of materials [6]. These mini twin-screw extruders have been widely used in mixing polymer blends [7-11] and nanocomposites [12-17].

The morphology development of polymer blends in some of these mini twin-screw extruders has been investigated and compared to batch mixers and twin

screw extruders [6, 18-20]. However, there is no agreement whether the mini mixers perform better or comparable to the industrial devices in terms of mixing polymer blends. Oommen et al [20] compared the morphology of Nylon-6/EPR blends mixed by the Haake Rheocord mixer, the 5ml DSM micro-compounder and the ZSK-25 industrial extruder. They found that the mini extruder generated a finer dispersed phase size than the Haake batch mixer but a larger size than the industrial extruder. Walia et al [19] studied the mixing of PS/PMMA with three different viscosity ratios (VR) (by changing the mixing temperature) in the Haake batch mixer and the 7ml Haake MiniLab II. They found that the mini extruder performed similarly as the Haake batch mixer for VR < 1 and less favorably for VR > 1.

In this chapter, the DSM Micro-Compounder and Prism twin screw extruder were evaluated in terms of their efficiency of mixing polymer blends and nanocomposites and compared to MBM and APAM.

5.2 Experimental

5.2.1 Materials

Materials used in this chapter are listed in Table 5.1.

Table 5.1: Polymer and nano-filler used in experiments.

Material (Abbreviation)	Source (Tradename)	$M_w \cdot 10^{-4}$ (g/mol)	Density (g/cc, 25°C)
Polystyrene (PS)	Dow Chemical (Styron 666D)	16	1.05
Polystyrene-5% maleic anhydride (PSMA)	Arco	Not available	Not available
Polyamide (PA)	DuPont (Zytel330)	Not available	Not available
Polyethylene: low variance in MW-PE (HDPE)	Nova Chemical (SP Sclair 2907)	Not available	0.96
5% Maleic Anhydride Grafted Polyethylene (PEMA)	Dupont (Fusabond 2650)	4.84	0.73
Montmorillonite Clay (C20A)	Southern Clays (Cloisite 20A)	Not available	1.77
Polyamide 6 (PA-B3)	BASF (ULTRAMID B3)	Not available	1.13
Polyamide 6 with 20 w% FIBRIL Nanotubes (MB4020)	Hyperion Catalysis (MB4020-00)	Not available	Not available

5.2.2 Mixing

The compositions, mixing temperature, and rotational speeds of polymer blends and nanocomposites are given in Table 5.2. Two mini twin-screw extruders, DSM micro-compounder (15ml, Xplore, Figure 5.1) and Prism twin

screw extruder (16mm,Thermo Scientific, Figure 5.2), were used to mix polymer

blends and nanocomposites on the laboratory-scale.

Table 5.2: The compositions of polymer blends and nanocomposite with mixing conditions.

Compositions	Composition Ratio	Temperature (°C)	Rotation speed (rpm)
PS/PA	80/20	200	50 100 150
PSMA/PA	80/20	200	50 100 150
HDPE/C20A	95/5	200	50 100 150
PEMA/C20A	95/5	200	50 100 150
PA6-B3/MWCNT	99.5/0.5 99/1 98.5/1.5 98/2 97.5/2.5 97/3 96/4 94/6 92/8 90/10	260	150

5.2.2.1 Mixing procedures in DSM

DSM has a capacity of 15ml and consists of two conical co-rotating screws

with a bypass allowing the material to circulate. It was operated in batch mode.

Materials were pre-mixed before feeding and then introduced into the pre-heated

rotating compounder. The time required for feeding was about 1 min and mixing

was done for an additional 10 min in batch mode. After the mixing time, the material was extruded through the heated cylindrical die to a water tank and then collected after drying in air.
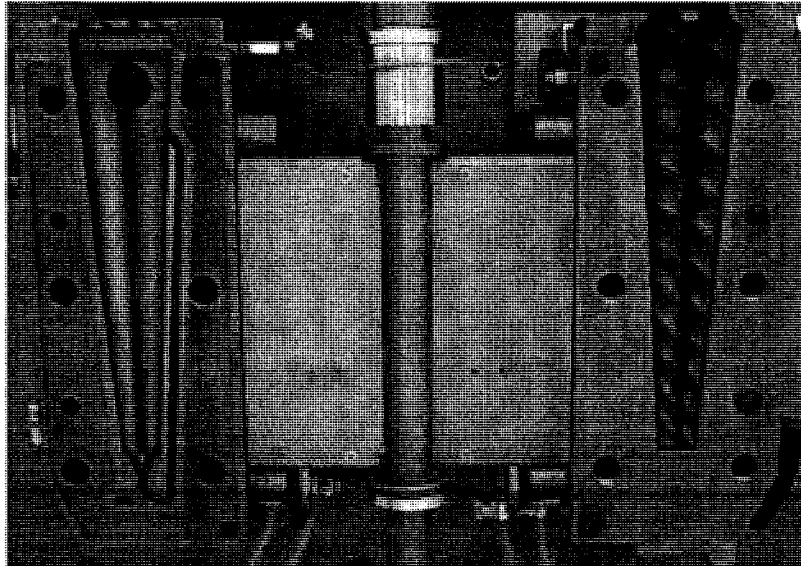
Figure 5.1: Photograph of 15mL DSM mini-twin screw extruder.

5.2.2.2 Mixing procedures in Prism

The Prism machine shown in Figure 5.2 is a co-rotating twin screw extruder with the screw length-to-diameter ratio (L/D) of 25. The total throughput in all composites was 0.7kg/h. The operating conditions for all composites are listed in Table 5.2. The material was cooled in a water bath and pelletized.
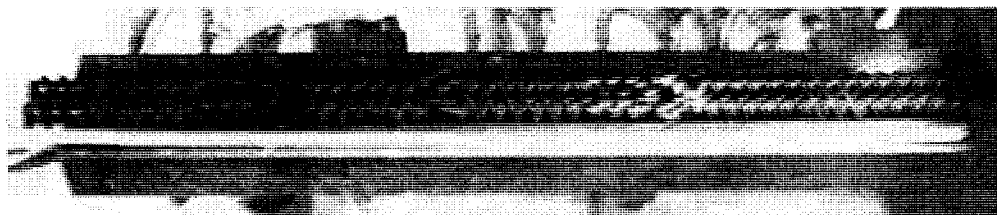
Figure 5.2: Photograph of Prism twin screw extruder (L/D: 25).

The nanocomposites were compression molded to discs for XRD and electrical measurements.

5.2.3 Characterization

The volume conductivity was measured on compression molded thin discs with a diameter of 60mm and a thickness of 0.6mm. The electrical volume resistance was measured with a Keithley Electrometer Model 6517 and an 8009 Resistivity Test Fixture equipped with ring electrodes. An alternate polarity method was used for the measurements utilizing the high resistance measurement software Keithley 6524. The surfaces of the samples were cleaned with ethanol prior to the measurements. According to ASTM D4496 and D257, the measured volume resistance, R_V, was converted to volume resistivity, ρ_v, using the formula

$$\rho_v = \frac{A}{t} R_v \qquad (5.1)$$

where A is the effective area of the measuring electrode and t is the average thickness of the specimen. Voltages of 40 or 400 V were used for conductive or resistive samples, respectively.

The experimental techniques for TEM and XRD were described in Chapter 3.

5.3 Results and discussion

5.3.1 Morphology of PS/PA uncompatibilized and compatibilized polymer blends

PS/PA blends were prepared by DSM and Prism respectively, at several different rotational speeds. Figure 5.3 shows the morphology development of the immiscible PS/PA blends mixed by DSM and Prism as a function of rotational speed. Under the same barrel temperature and rotational speed, the particles formed in DSM at 50 rpm as shown in Figure 5.3a were very large, on the order of 30-40 micron in diameter, while finer particles were formed in Prism at the same rotational speed as shown in Figure 3d. The morphology indicates that the dispersion mixing in DSM is very poor at 50 rpm. For Prism machine, an increase in rotational speed from 50 rpm to 150 rpm does not have significant influence on the morphology, which indicates that any significant change occurs at rotational speeds less than 50 rpm. However, for DSM, the particle size of the dispersed phase changes significantly from about 40μm at 50rpm to about 30μm at 100rpm and 1-3 μm at 150 rpm, which indicates that between rotational speeds of 100 to 150 rpm a very large change in the breakup of dispersed phase occurs in the DSM.

As shown in Figure 5.1, the DSM consists of only forwarding screw elements. When adding material into the DSM, forwarding screw elements convey material from the entrance to the bottom of the screw while also melting the material. The melted material is then re-circulated through the side channel. Although DSM is supposed to mimic the mixing behavior of a twin screw extruder (TSE), it does not have any kneading blocks or mixing sections, which are essential in a TSE to

promote both dispersive and distributive mixing. The main flow type inside the

DSM is pure shear flow, which is not sufficient for promoting dispersive
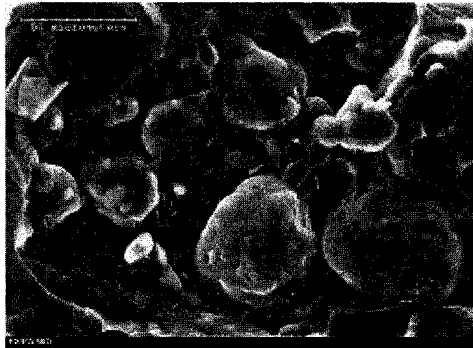
(a)
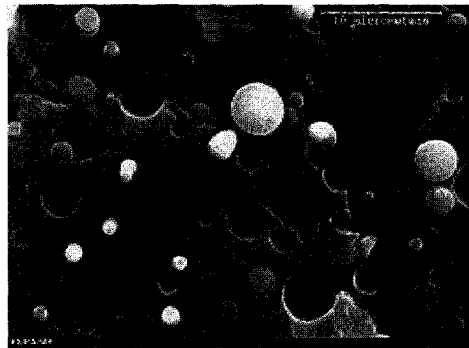
(d)
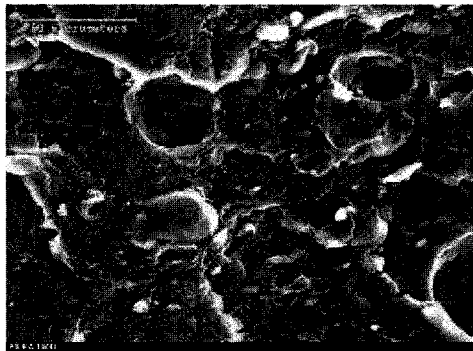
(b)
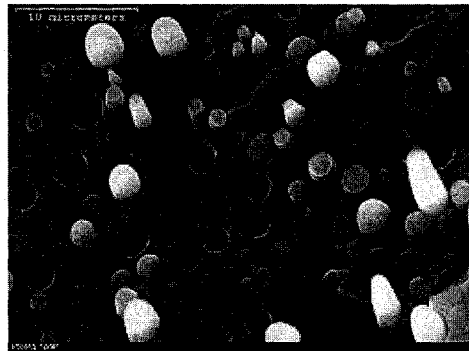
(e)
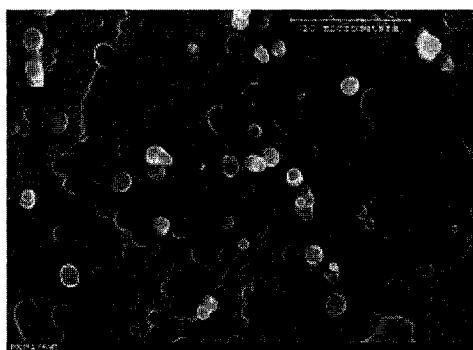
(c)
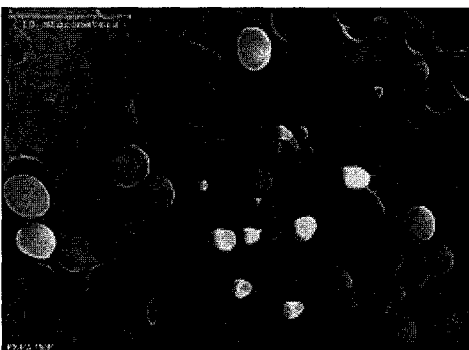
(f)

Figure 5.3: Comparison of Morphology of PS/PA blends mixed by DSM: (a) 50 rpm; (b) 100 rpm; (c) 150 rpm; and Prism (d): 50 rpm; (e) 100 rpm; (f) 150 rpm.

mixing [20]. The rotational speed required to break down the PS/PA blend in the 15ml DSM is much higher than the speed that Oommen et al [21] claimed was required for a 5ml DSM. In their study, the breakdown of the dispersed phase for Nylon-6/ethylene propylene rubber blends occurs at a rotor speed between 9 and 20rpm. Besides the difference in our system (different polymer blends), the clearance between the barrel and the rotor that determines the maximum shear rate is also different between a 5 ml DSM and a 15 ml DSM.

A reaction PSMA/PA system was studied. MA groups are introduced to the PS backbone to improve the adhesion between the PS and PA phases. The MA groups are expected to react with the amino acid groups of PA to form graft polymers that can link PS and PA phases. The morphology of reactive PSMA/PA blends is shown in Figure 5.4 as a function of rotational speed. For DSM, compared to the uncompatibilized PS/PA blend in Figure 3a-c, the dispersion of PA in PSMA in Figure 4a-c is much finer and the domain size is comparable to the domain size in Figure 4d-f. Overall, the influence of the rotor speed and the mixer type (DSM vs. Prism) on the morphology is not significant for reactive polymer blends. Thus, PSMA/PA may not be a good model system to study processing response because the dispersion in this system is fairly insensitive to the mixing equipment and the processing conditions [22].
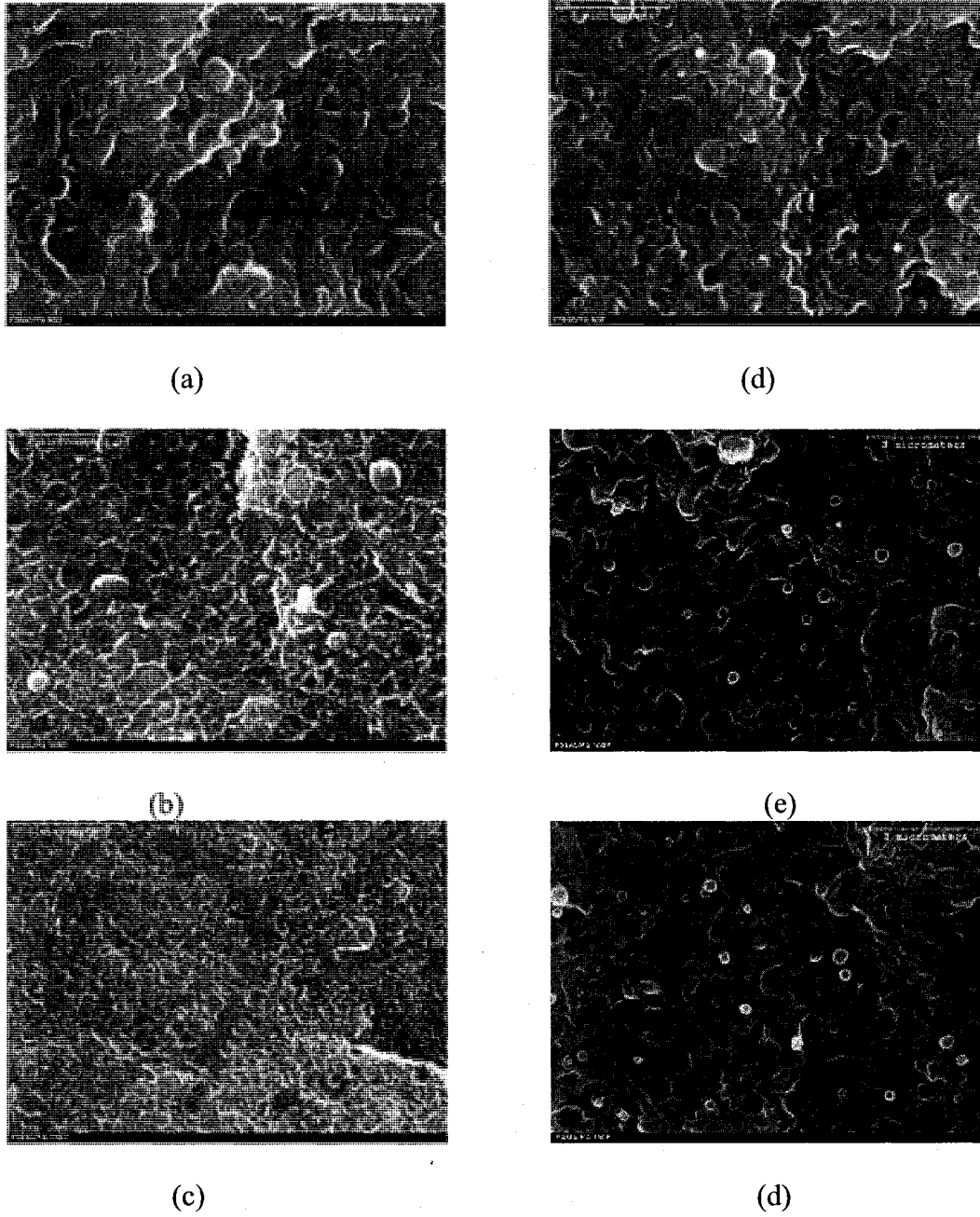
Figure 5.4: Comparison of Morphology of PSMA/PA blends mixed by DSM: (a) 50rpm; (b) 100rpm; (c) 150rpm; and Prism (d): 50rpm; (e) 100rpm; (f) 150rpm.

5.3.2 Polymer nanocomposites-clay

Figure 5.5 shows the XRD pattern of PE/C20A nanocomposites processed by DSM and Prism respectively, where the peaks correspond to the (011) plane reflections of the clay. The XRD of the Cloisite 20A clay indicates a layer spacing of 2.23nm. After melt blending with PE, the position of the clay peak shifted to lower angle for all samples, which indicated that the melt-mixed PE/C20A nanocomposite was intercalated at the tested rotational speeds. For DSM, the interlayer spacing increased to a slightly higher value of 2.38nm for 50rpm, 2.44nm for 100rpm and 2.50nm for 150rpm. For Prism, the interlayer spacing was about 2.63nm for 50 and 100rpm and increased to 2.7nm for 150rpm. The clay peak also becomes shorter and broader as the rotational speed increases, which is another overall indication of increasing interlay spacing of clay [23]. Prism at the lowest tested speed yielded better dispersion than DSM at the highest speed for unmodified PE/C20A nanocomposites. From Chapter 3 and Chapter 4, we see that for PE/C20A mixed at 150rpm, the d-spacing is 3.2nm for MBM and 2.54nm for APAM. The MBM has the best mixing performance among these miniature mixers because of the co-existence of shear flow and elongational flow.

Modifying non-polar olefins by adding polar groups such as maleic anhydride helps to promote the exfoliation of nano-filler in olefinic polymers. The PEMA used here contains 5wt% maleated groups. Figure 5.6 shows the XRD patterns of PEMA/C20A nanocomposites mixed by DSM and Prism at different rotational speed. Under the same processing conditions, adding MA groups greatly promoted the intercalation of clay in the nanocomposites mixed by both mixers.
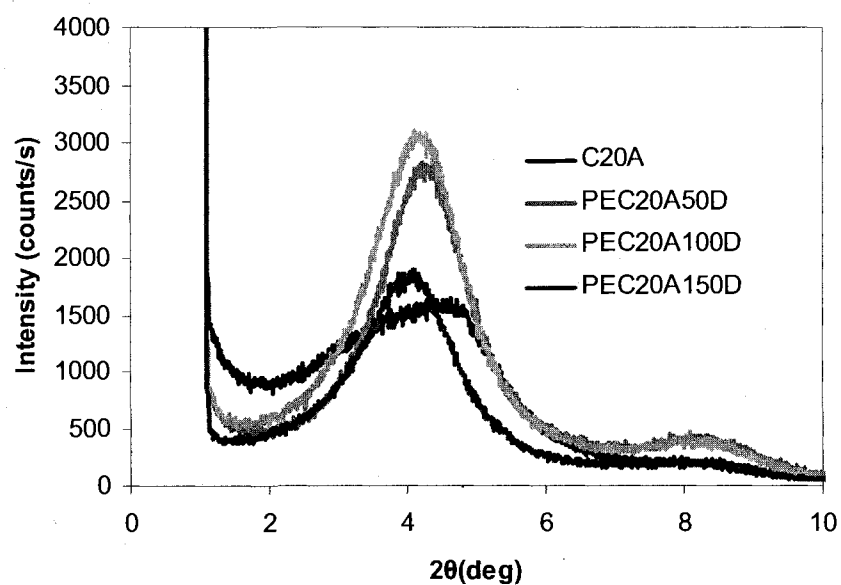
(a)
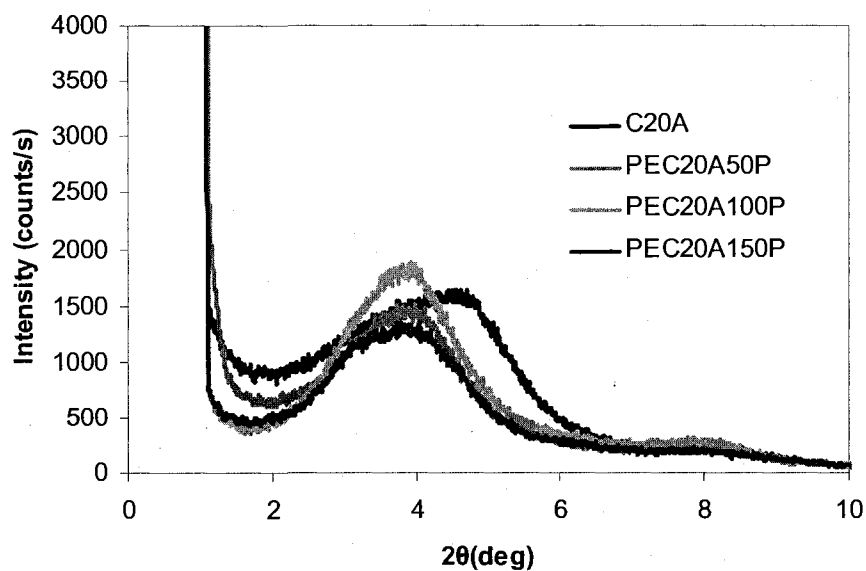
(b)

Figure 5.5: XRD pattern of PE/C20A (5 wt% C20A) with different rotor speed for (a) DSM and (b) Prism.

Even at 50 rpm, the PEMA/C20A nanocomposite mixed by DSM has an interlayer spacing of 3.9 nm, which is a substantial increase from the d-spacing of 2.38 nm in the corresponding PE/C20A system. The clay peak disappeared for

samples compounded in both mixers at 150 rpm and indicated a high extent of exfoliation and delamination under high shear rate. All other samples exhibited a mixture of exfoliated and intercalated structures in the composites. The exfoliated structure in the composites compounded at 150 rpm was also confirmed by the TEM analysis of microtomed sections of the samples as shown in Figure 5.7.

From Chapter 3 and 4, we see that the PEMA/C20A nanocomposites mixed by MBM and APAM are also exfoliated or highly intercalated. While the PEMA/C20A system shows that DSM has the ability to achieve exfoliated nanocomposites under favorable conditions (i.e., it is a compatibilized mixture). The system is insensitive to distinguish the mixing efficiency between different equipment.
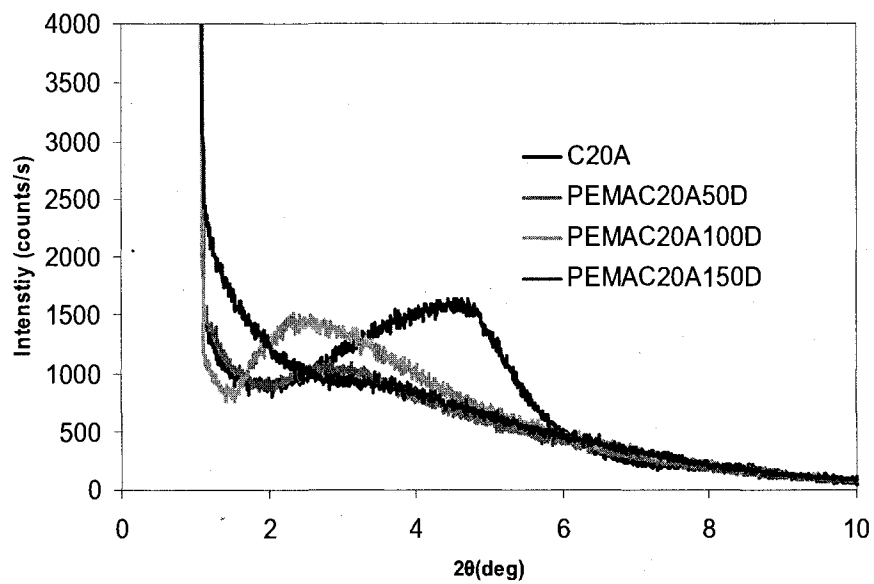
(a)
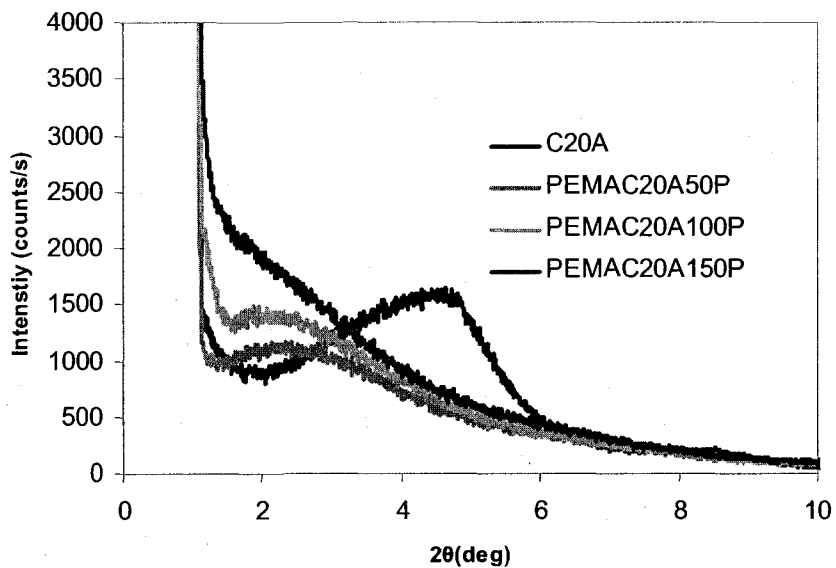
(b)

Figure 5.6: XRD pattern of PE/C20A (5 wt% C20A) with different rotor speed for (a) DSM and (b) Prism.
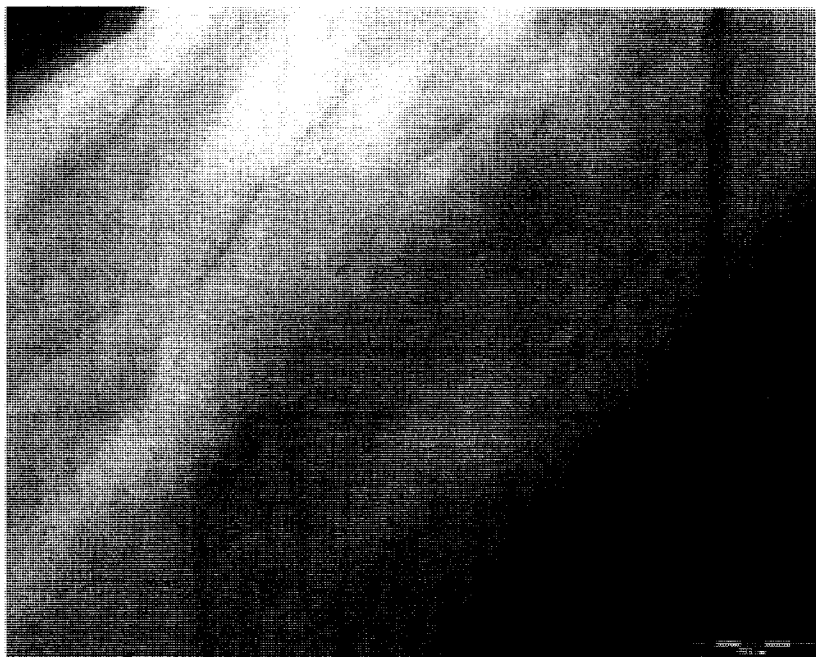
(a)
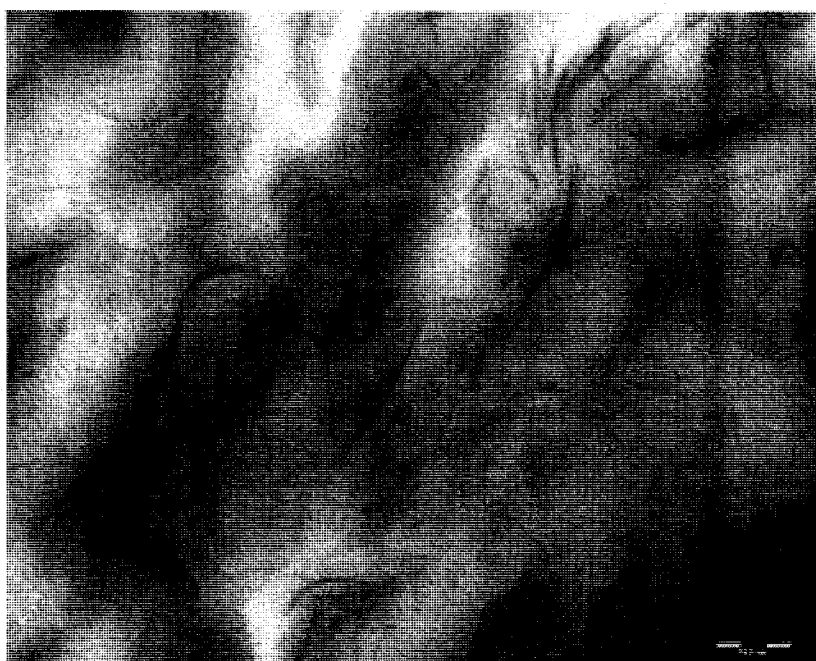
(b)

Figure 5.7: TEM of PEMA/C20A (95:5wt) compounded by (a) DSM and (b) Prism
respectively at 150rpm.

5.3.3 Polymer nanocomposites: MWCNT

One of the motivations to develop small-scale mixer or extruders is the high cost of carbon nanotubes and therefore the intention to lower the cost by using small amount of materials. From previous analysis based on polymer blends and clay nanocomposites, it is found that less miscible systems should be chosen to compare the mixing efficiency of different devices. The MWNT without chemical treatment is difficult to disperse into PA-6 matrix by melt compounding. Therefore the PA-6/MWNT system was used to evaluate the processing ability of the two small-scale extruders.

The indication for efficient dispersion and interconnectivity of MWCNT in PA-6 can be obtained from volume resistivity measurement of the PA6/MWCNT nanocomposites. The composites were obtained by diluting a masterbatch containing 20 wt% MWCNT. Figure 5.8 shows the volume resistivity as a function of weight fraction of MWCNT in the PA-6 matrix mixed by DSM and Prism respectively at 150rpm. The volume resistivity of the PA-6 used in this study was 1015 Ω-cm. Increasing MWCNT content from 0.5% to 10wt% resulted in almost 13 orders of magnitude reduction in volume resistivity. A significant drop in volume resistivity was achieved at a percolation threshold of about 5 wt% for both mixers. This value is in accordance with the reported values of 4-6 wt% in PA6/MWCNT composites using the same masterbatch [24, 25]. Interestingly the composite compounded by Prism has two sharp drops: one close to 2wt% with a 7 orders of magnitude reduction and another close to 6 wt% with a

further 5 orders of magnitude reduction. This may be caused by the inaccuracy of the measurement in the middle range of the volume resistivity.
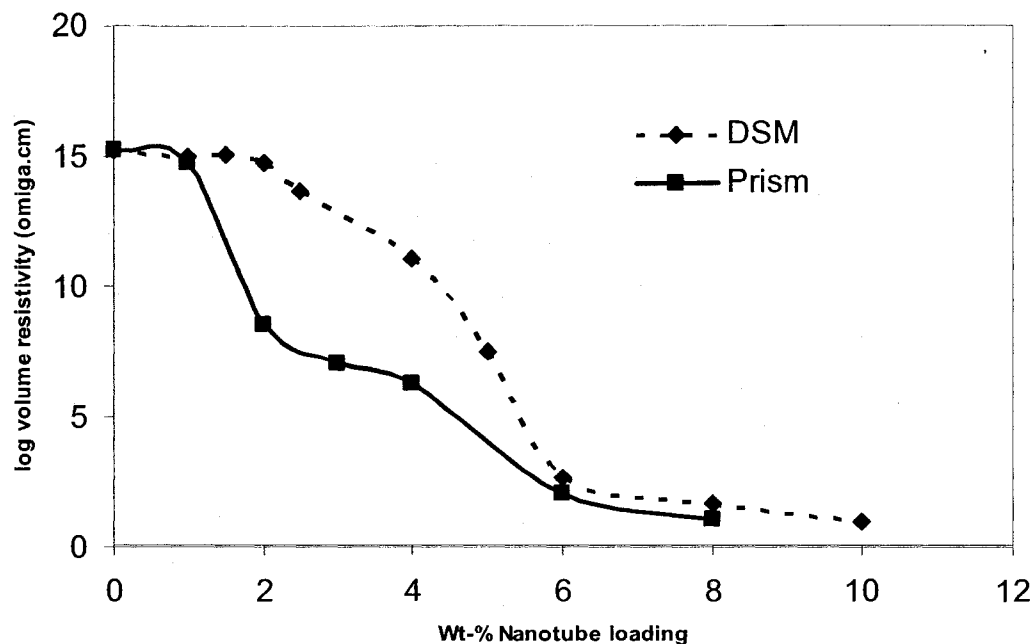
Figure 5.8: Change in volume resistivity with MWCNT content in PA6-B3/MWCNT nanocomposites compounded by (♦) DSM and (■) Prism.

As shown in Figure 5.9, the MWCNT was already well dispersed in PA-6 at a concentration of 4 wt%. The individual nanotubes is visible in Figure 5.9a and 5.9b with a diameter about 12nm, which is in accordance with the report by Hyperion [26, 27]. At a higher concentration of 6 wt% MWCNT, the formation of nanotubes aggregates was observed along with the dispersed individual tubes.

Both the percolation threshold and the TEM images of MWCNT /PA-6 (4wt% and 6wt% MWCNT) compounded by DSM and Prism are comparable with the

reported MWCNT dispersion in Nylon 6 extruded by a twin screw extruder (ZSK25) at 200 rpm.

(a)   (b)

(c)   (d)
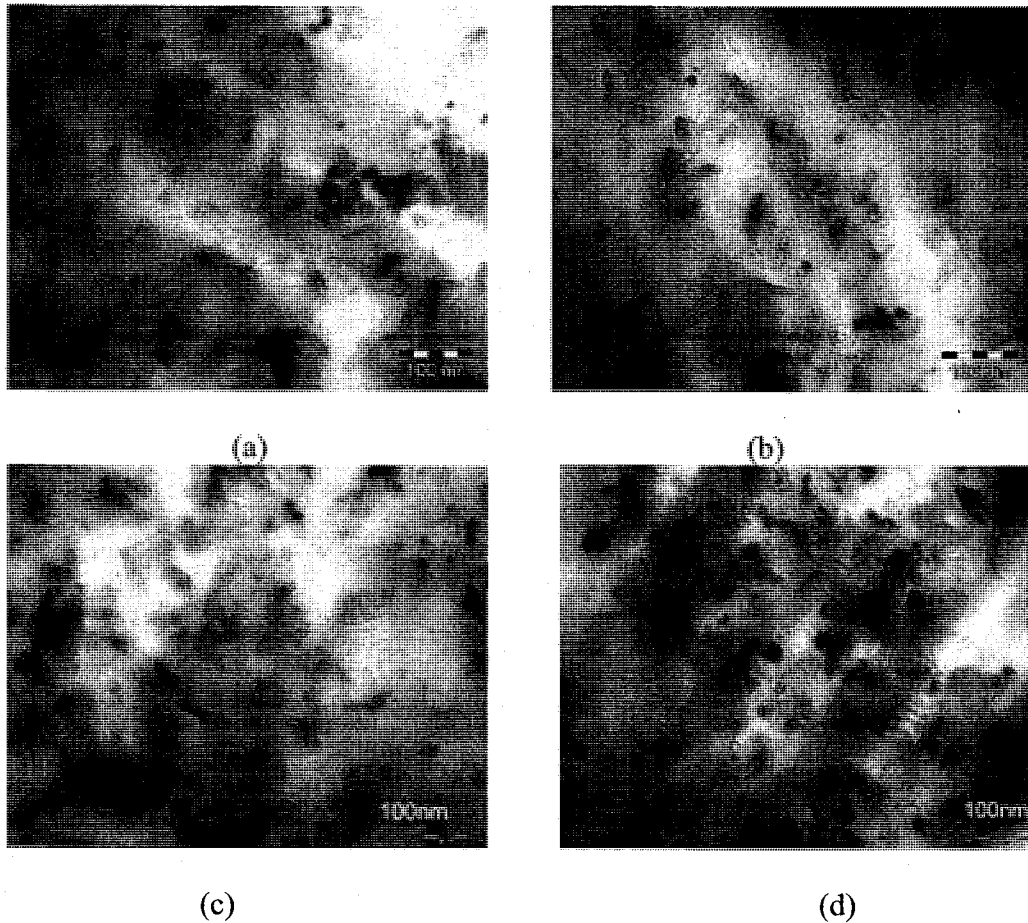
Figure 5.9: TEM images of PA-6 with 4wt% MWCNT compounded by (a) DSM and (b) Prism; 6wt% MWCNT compounded by (c) DSM and (d) Prism.

5.3.4 Simulation of Mixing

Isothermal simulations at 50 and 150 rpm were done for DSM using Polyflow 3.10 based on material properties of PS (Chapter 2) at 200°C. The computational procedures were described in Chapter 2. Since no detailed dimensions for DSM was disclosed by the manufacturer, the DSM geometry was constructed based on our measurements to best possible accuracy. Because of the large length/diameter

ratio and complex geometry, there is a huge cost for memory and a lengthy time is required to model the complete extrusion process. For modeling continuous twin screw extruders, a mixing section based on the geometry of ZSK25 was constructed to model the mixing in a TSE. As shown in Figure 5.10, from right to left, the mixing section consists of one 12 mm forward screw element with 24mm pitch (FSE 24/12), one forward 24 mm 45°-staggered kneading blocks with 24 mm pitch (FKB 24/24), one 12 mm reverse pumping element (RPE 24/12) and another 12 mm FSE 24/12. The total axial distance is 60 mm.

The particle tracking was done in Polyflow and visualized using the code from Alemaskin et al [28]. Three thousand massless points were released at the entrance of the DSM and the mixing section of TSE at the starting time to visualize the particle movement with time. No more particles were released after the initial release.

As shown in Figure 5.10, it took about 4s for the first particle to move to the exit of the 60mm mixing section at a throughput of 0.7 kg/h and 50 rpm. After the first second, the particles front moved to the end of the first forward screw element and enters the kneading block. With time, more particles moved to the left and were distributed uniformly. The particles were also observed to flow through the gap between the rotor and the barrel. After 4 s, the particle front was at the exit while the majority of particles were still in the pumping elements after to the left of the kneading block.
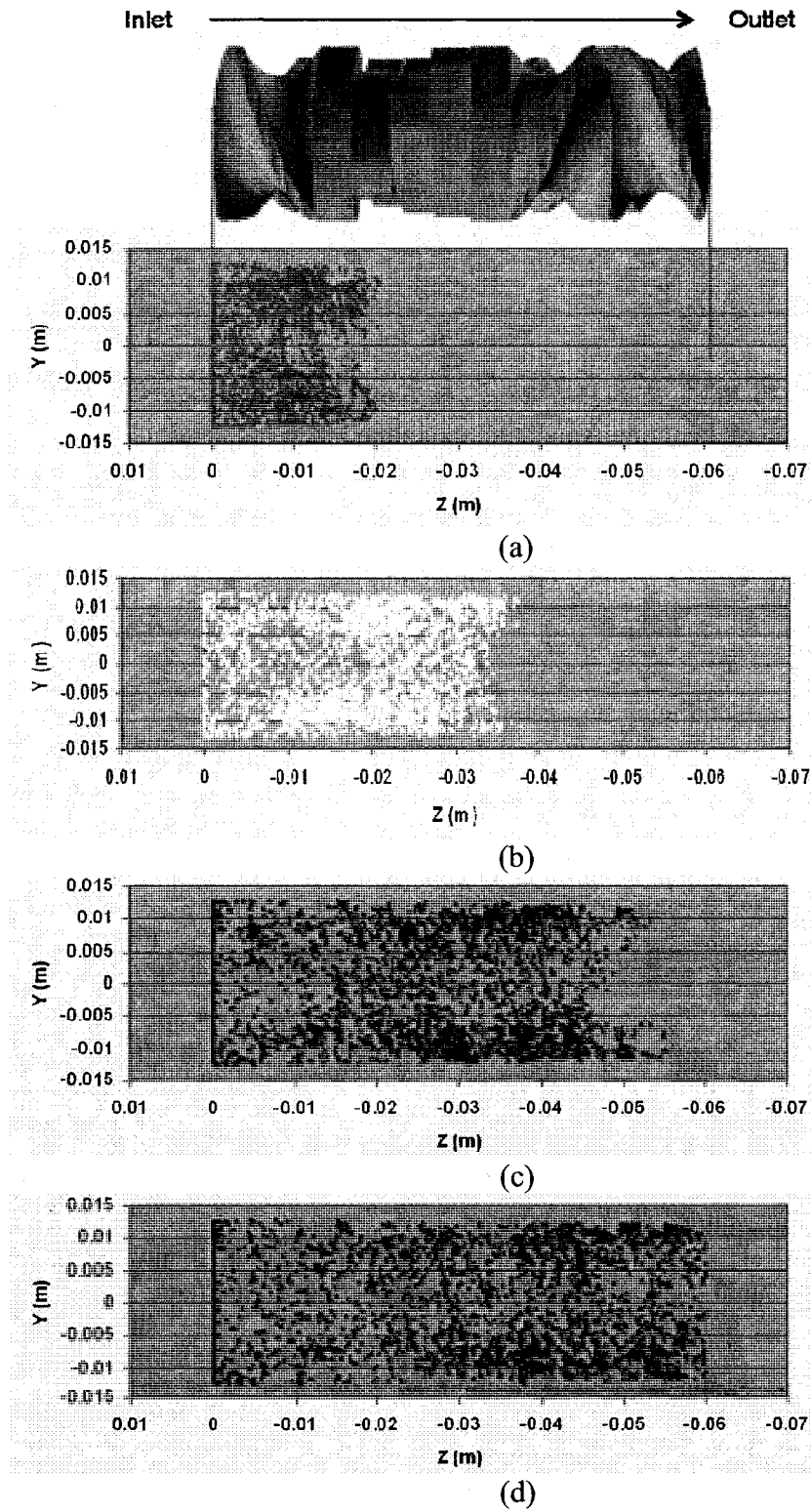
Figure 5.10: Particle movement in a 60mm length mixing section of 25mm ZSK TSE at 50rpm: (a) after 1s;(b) after 2s; (c) after 3s and (d) after 4s.

At the same rotational speed, it took much longer time for particles in DSM to go from the top to the bottom at 50 rpm as shown in Figure 5.11. The particles were released from a small cylindrical box (1mm D*10 mm L) located in the center of the screws at time zero. After 100 s, the particle front had moved halfway down the mixer. It took about 300 s for the particle front to move to the bottom of the mixer. After 600 s, there were only a few particles entering the side channel but no recirculation occurred. While some of the particles seem to move along the rotor blades near the entrance, most of particles were stuck in the bottom instead of re-circulating through the side channel.

The same particle tracking simulation was done for DSM at 150 rpm and the results are shown in Figure 5.12. The recirculation in the side channel appeared after 10 min at 150 rpm. As shown in Figure 5.12, the particle front had moved to the end of screw after 100 s. This makes sense since the speed of the particles was three times as fast as that at 50 rpm. After 600 s, there were particles in the side channel that had almost flowed back to the main chamber.

Due to the limitation of the software, one of the assumptions made for the simulation was that the mixer was always fully filled, which is not the case for the experiment where the mixer was only 80% filled. In the partially filled chamber, the pressure at the top of the screw would be much lower than in the fully filled chamber and therefore should make the recirculation flow faster. Combining the lack of mixing shown in the simulation results with the poor morphology of PS/PA blends at 50rpm, the lack of enough recirculation flow may account for the poor mixing in DSM at low rotational speed. Therefore, the mixing time may

need to be extended at low rotation speed (less than 150 rpm) to ensure good

quality mixing. The better solution would be to use rotational speed of 150 rpm

or higher so that the material does not degrade during high mixing speed.
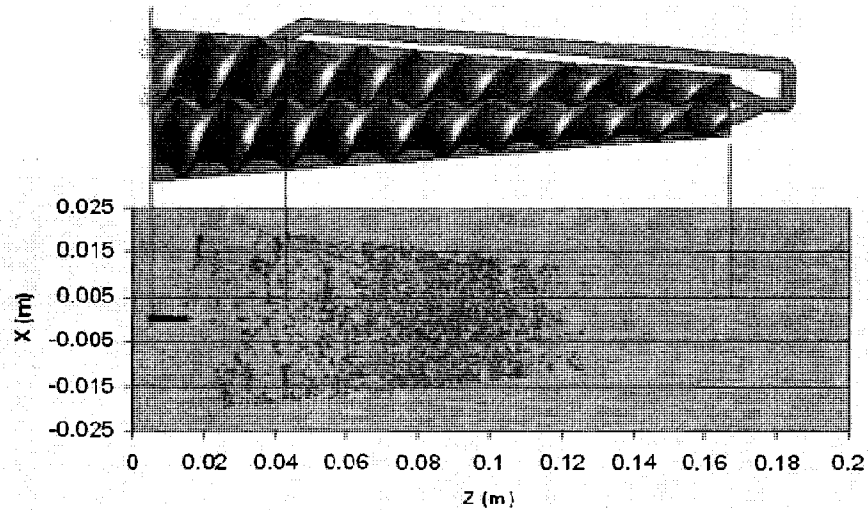
(a)
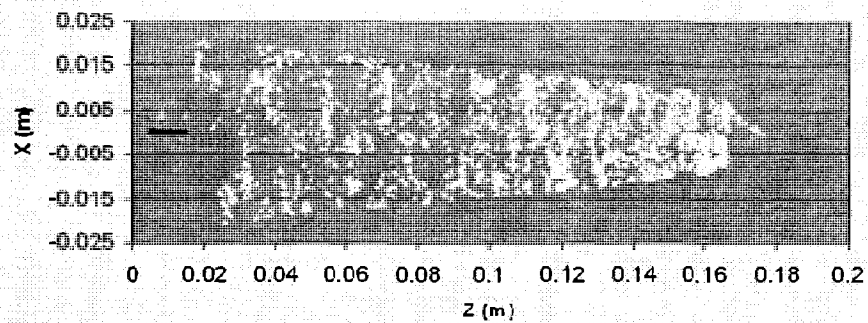
(b)
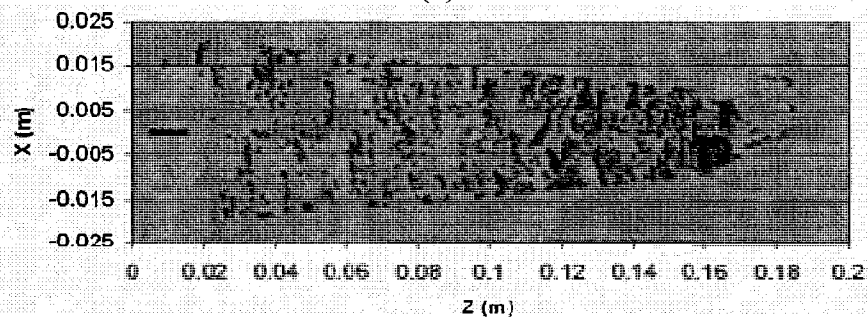
(c)

Figure 5.11: Particle movements in DSM at 50 rpm: (a) after 100 s; (b) after 300 s; (c) after 600 s.
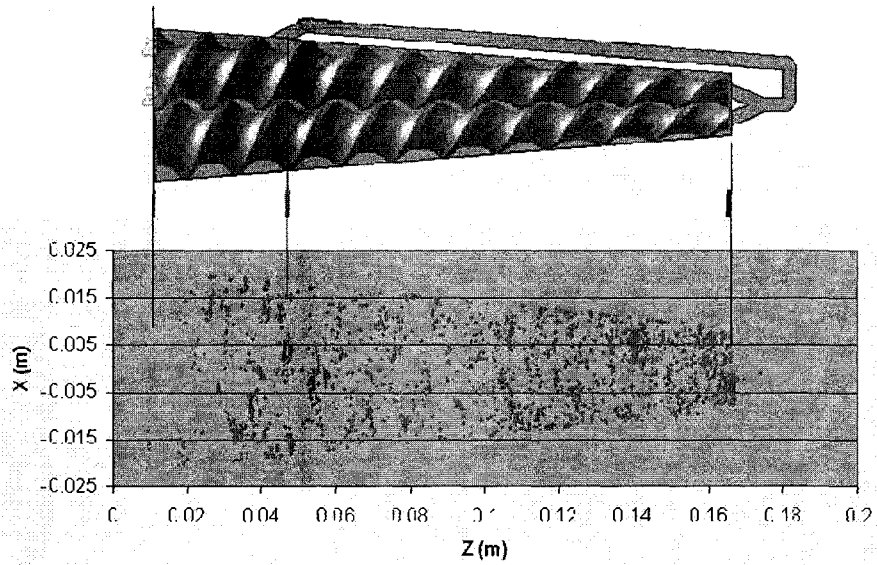
(a)
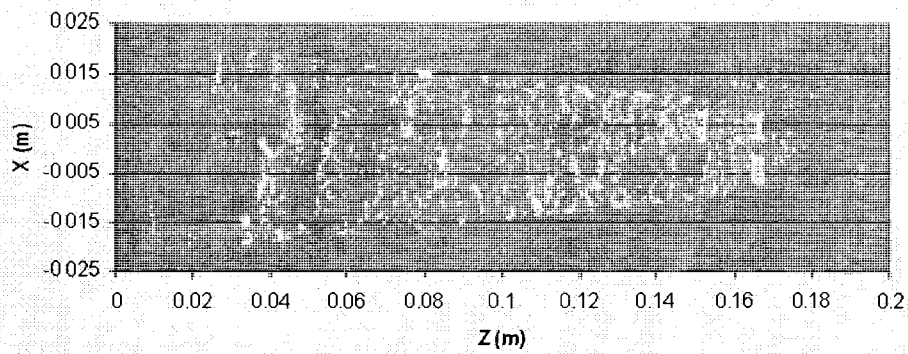
(b)
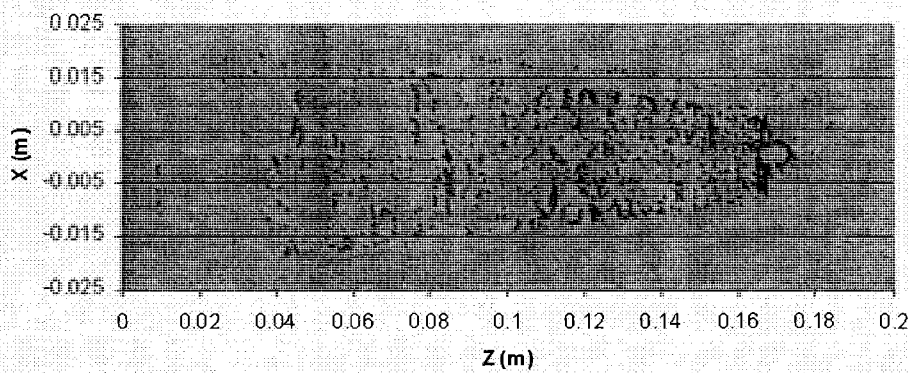
(c)

Figure 5.12: Particle movements in DSN at 150 rpm: (a) after 100 s; (b) after 300 s; (c) after 600 s.

5.4 Summary

The mixing performance of DSM and Prism mini twin screw extruders was evaluated for polymer blends and nanocomposites processing. For a high rotational speed of 150 rpm, DSM has a mixing efficiency comparable to the Prism. Exfoliated nanocomposites were observed for PEMA/C20A compounded by both mixers at 150rpm. A percolation threshold of about 5 wt% was found for PA6/MWCNT mixed in both mixers at 150rpm, which is in agreement with the reported values [23, 24]. However the initiation of percolation occurred at a much lower concentration in Prism at MWCNT concentration of 2-5 wt%, while the resistivity of the PA6/MWCT nanocomposite was five orders of magnitude lower in Prism than DSM.

At lower rotational speed, the mixing quality in DSM was poor, especially for non-reactive polymer blends. The simulation results show that there was not much recirculation flow at 50 rpm within 10 min mixing. The poor morphology of polymer blends and nanocomposites produced in DSM at low rotational speed also indicates poor mixing performance. Extended mixing time is suggested for DSM operating at low speed to ensure enough recirculation through the side channel.

The non-reactive polymer blends and uncompatibilized nanocomposites were difficult to disperse and generally sensitive to the mixer type. Therefore, these type of systems should be used for differentiating the mixing performance of different types of equipment.

5.5 Reference

1. http://www.thermo.com/com/cda/product/detail/0,1055,21955,00.html

2. http://www.daca.com/productsdaca/mcpage.html

3. http://www.xplore-together.com/5ml_compounder.htm

4. http://www.xplore-together.com/15ml_compounder.htm

5. http://www.thermo.com/com/cda/product/detail/1,1055,23501,00.html

6. Charoensirisomboon P., Weber M., "Reactive PSU/PA blends: comparison of materials prepared by mini-twin screw extruder and batch mixer", *Polymer*, **42 (16)**, 7009, 2001.

7. Sarkissova M, Harrats C, Groeninckx G, Thomas S, "Design and characterisation of microfibrillar reinforced composite materials based on PET/PA12 blends", *Composites Part A-Applied Science and Manufacturing*, **35 (4)**, 489, 2004.

8. Everaert V, Aerts L, Groeninckx G, "Phase morphology development in immiscible PP/(PS/PPE) blends influence of the melt-viscosity ratio and blend composition", *Polymer*, **40 (24)**, 6627, 1999.

9. Anttila U, Hakala K, Helaja T, Lofgren B, Seppala J, "Compatibilization of polyethylene/polyamide 6 blends with functionalized polyethylenes prepared with metallocene catalyst", *Journal of Polymer Science Part A-Polymer Chemistry*, **37 (16)**, 3099, 1999.

10. Vocke C, Anttila U, Seppala J, "Compatibilization of polyethylene polyamide 6 blends with oxazoline-functionalized polyethylene and styrene ethylene

butylene styrene copolymer (SEBS)", *Journal of Applied Polymer Science,* **72 (11),** 1443,1999.

11. Vocke C, Anttila U, Heino M, Hietaoja P, Seppala J, "Use of oxazoline functionalized polyolefins and elastomers as compatibilizers for thermoplastic blends", *Journal of Applied Polymer Science,* **70 (10),** 1923, 1998.

12. Davis CH, Mathias LJ, Gilman JW, Schiraldi DA, Shields JR, Trulove P, Sutto TE, Delong HC, "Effects of melt-processing conditions on the quality of poly(ethylene terephthalate) montmorillonite clay nanocomposites", *Journal of Polymer Science Part B-Polymer Physics,* **40 (23),** 2661, 2002.

13. Potschke P, Bhattacharyya AR, Janke A, Goering H, "Melt mixing of polycarbonate/multi-wall carbon nanotube composites", *Composite Interfaces,* **10 (4-5),** 389, 2003.

14. Potschke P, Bhattacharyya AR, Janke A, "Carbon nanotube-filled polycarbonate composites produced by melt mixing and their use in blends with polyethylene", *Carbon,* **42 (5-6),** 965, 2004.

15. Abdel-Goad M, Potschke P, "Rheological characterization of melt processed polycarbonate-multiwalled carbon nanotube composites", *Journal of Non-Newtonian Fluid Mechanics,* **128 (1),** 2, 2005.

16. McNally T, Potschke P, Halley P, Murphy M, Martin D, Bell SEJ, Brennan GP, Bein D, Lemoine P, Quinn JP, "Polyethylene multiwalled carbon nanotube composites", *Polymer,* **46 (19),** 8222, 2005.

17. Dondero WE, Gorga RE, "Morphological and mechanical properties of carbon nanotube/polymer composites via melt compounding", *Journal of Polymer science Part B-Polymer Physics,* **44 (5),** 864, 2006.

18. Maric M. and Macosko C. W., "Improving polymer blend dispersions in mini-mixers", *Polymer Engineering and Science,* **41(1),** 118, 2001.

19. Walia P., Barger M., McKelvy M., "Quantitative mixing uniformity assessment in two laboratory scale devices", *ANTEC,* 265, 2005.

20. G. Özkoc(a), J. Tiesnitsch(b), M. Quaedflieg (b) and G. Bayram, "Micro-compounding of ABS/PA6 Blends Based Nanocomposites", *presented at PPS-22,* YAMAGATA, 2006.

21. Oommen Z., Zachariah S. R., Thomas S., Aravind I., Groeninckx G., "Phase morphology development in uncompatibilized and reactively compatibilized Nylon-6/Ethylene Propylene Rubber (EPR) blends: Effect of mixer type on morphology", *Journal of Macromolecular Science Part B-Physics,* **B43 (5),**1025, 2004.

22. Sundararaj, U.; Macosko, C. W., "Drop breakup and coalescence in polymer blends - the effects of concentration and compatibilization", *Macromolecules,* **28 (8),** 2647, 1995.

23. Dennis H. R., Hunter D. L., Chang D., Kim S., White J. L., Cho J. W., Paul D. R., "Effect of melt processing conditions on the extent of exfoliation in organoclay-based nanocomposites", *Polymer,* **42 (23),** 9513, 2001.

24. Meincke O, Kaempfer D, Weickmann H, Friedrich C, Vathauer M, Warth H, "Mechanical properties and electrical conductivity of carbon-nanotube filled

polyamide-6 and its blends with acrylonitrile/butadiene/styrene", *Polymer*, **45**

(3), 739, 2004.

25. Schartel B, Potschke P, Knoll U, Abdel-Goad M., "Fire behaviour of polyamide 6/multiwall carbon nanotube nanocomposites", *European Polymer Journal*, **41 (5),** 1061, 2005.

26. http://www.fibrils.com/PDFs/New%20Developments.pdf

27. http://www.fibrils.com/PDFs/SPE%20Auto%20Composites%202002-09-13%20.pdf

28. Alemaskin K, Manas-Zloczower I, Kaufman M, "Color mixing in the metering zone of a single screw extruder: Numerical simulations and experimental validation", *Polymer Engineering and Science*, **45 (7),** 1011 2005.

Chapter 6

GENERAL DISCUSSION AND FUTURE WORK

6.1 General discussion and conclusions

The focus of this thesis is to investigate processing of polymer blends and nanocomposites in small-scale mixers by both experimental and computational approaches. The work is driven by the need to develop new polymer nanocomposites on the small scale (tens of grams) or the miniature scale (grams) and to understand the fundamental aspects related to processing polymer materials in such mixers. Two main topics are addressed in this thesis: one is non-isothermal modeling of polymer processing in batch mixers using full 3-D geometries, and the other is evaluating the mixing efficiency of the small-scale mixers in terms of compounding polymer blends and nanocomposites.

In a cost and time efficient way, the non-isothermal modeling of polymer processing in batch mixers provided the essential information of heat transfer, temperature distribution, flow type, and shear stress in the process, which are important to understand the relationships between the final morphology of polymer blends and composites and the processing parameters such as processing conditions and mixer geometry. For the modeling work, the difficulty lies in incorporating the non-Newtonian fluid properties of polymers and the complexity of the mixer geometry.

In the second topic, polymer blends and nanocomposites were mixed using commercially available miniature mixers and using customer designed mixers that

built in-house. The commercially available miniature mixers studied were the 15 ml DSM micro-compounder and Haake batch mixer (Produced by Thermo Fisher Scientific). The in-house custom-built mixers were the APAM and the MBM. Representative systems of immiscible polymer blends, reactive polymer blends, uncompatibilized nano-clay composites, compatibilized nano-clay composites and carbon nanotubes composites were chosen and were processed in all mixers. The morphology of the polymer blends and nanocomposites was examined and compared to larger scale mixers such as the Prism twin screw extruder (Currently manufactured by Thermo Fisher Scientific).

For polymer processing in batch mixers, the final temperature of the polymer melts often exceeds the pre-set processing mixer barrel temperature due to viscous heating resulting from conversion of mechanical energy to thermal energy via viscous dissipation. The amount of viscous heating depends on the mixer type, processing conditions and the polymer properties. The resulting temperature may change chemical structure and therefore affect the final properties of the processed material. In worst situation, the viscous heating may cause serious degradation and greatly lower the final product performance. The temperature rise of polymer melt in batch mixers due to viscous heating under constant mixer barrel wall temperature was addressed using a non-isothermal simulation based on full 3-D geometries of the mixers. The simulation was validated by comparing the temperature history and the mechanical power data from experiments and a good agreement was obtained for both the 69 mL BM and the 3 ml MBM.

From the simulation results based on the same processing temperature (463K), rotational speed (50 rpm) and the same polymer properties (PS), the average temperature rise is about 2K for BM and 1K for MBM, which are relatively low and will not cause any serious thermal degradation. However, even though the volume of the APAM is smaller (2 mL compared to 69 mL BM and 3 ml MBM), it caused an average of 4K, which is twice that of BM and MBM. Moreover, the highest temperature in APAM was about 7K higher than the pre-set processing temperature, which is significant for such a small volume. The relatively large temperature rise in APAM was caused mainly by the significantly high shear rate generated in the smallest gap (0.25 mm), which is half the size of the smallest gap (0.5 mm) in MBM. The smallest gap also limited material passage and convective heat transfer in the area, causing heat accumulation, which gave rise to the high local temperature. By extending the cup diameter of APAM (6.5 mm), two revised versions, APAM_Rev1 and APAM_Rev2 with a diameter of 6.75 mm (0.50 mm gap) and 7 mm (0.75 mm gap) respectively, were obtained virtually and modeled under the same processing conditions and polymer properties. By increasing the gap size to 0.5 mm, the average temperature rise for APAM_Rev1 was 1K lower than that in APAM. The temperature distribution is much more uniform because the larger gap allows more material passage. Increasing the gap size further to 0.75 mm did not significantly lower the temperature rise and required a much longer time to reach thermal steady. So 0.5 mm may be an optimum gap size for APAM.

Because of the small scale, other than the natural convection to the surrounding air, no extra cooling is added for MBM and APAM to remove the viscous heating. To validate this assumption, the heat transfer coefficients during the process were derived from simulation results. The time average heat transfer coefficient is about 9 $W/m^2/K$ for BM, 3 $W/m^2/K$ for MBM and 14 $W/m^2/K$ for APAM. These values are close to the natural convection heat transfer coefficient determined from empirical correlations, so this indicated that natural convection can transfer most of the heat generated from viscous heating.

One of the advantages of 3-D simulation based on full geometry is that it provides the detailed flow and temperature information everywhere inside the mixer instead of only the averaged parameters derived from analytical calculations or simulations of simplified geometries. The temperature distributions of BM and MBM at the thermal steady state are very similar due to the geometry similarity. The highest temperature rise appeared in the area around the rotor tips in all three mixers (BM, MBM and APAM). While BM and MBM both had quite a uniform temperature distribution with a small temperature gradient toward the mixer wall, there were quite a few hot spots in APAM with a temperature 7K higher than the wall temperature. Once again, the highest temperature in APAM was caused by the extremely small gap. The hot spots disappeared when we extended the cup diameter of APAM to 6.75 mm, which gave a 0.5 mm minimum gap.

The velocity profiles of BM, MBM and APAM obtained from simulation show detailed information on the nature of shear flow, folding and reorientation in

all mixers. The elongational flow was generated because of the nature of counter-rotating two asymmetric rotors and the different rotational speeds of the two rotors in BM and MBM. In APAM, the single asymmetric rotor generated elongational flow in a limited area. Mixing index obtained from simulation confirmed the existence of elongational flow and showed the area where it occurred.

The average shear rate under the simulated conditions is 21 s^{-1} for BM, 23 s^{-1} for MBM and 35 s^{-1} for APAM. Simulation results showed that APAM has wider shear rate and shear stress distributions resulting from the narrow gap region.

The MBM and APAM were tested for their ability to process polymer blends and polymer nanocomposites and their mixing performance was compared with that of the larger scale BM. Under the same processing conditions and for the material, both MBM and APAM produced a similar and sometimes even finer dispersed phase than BM, especially for nanocomposites. Under the same processing conditions, an exfoliated structure was obtained for PEMA/clay nanocomposites by direct melt-mixing in all three mixers.

The mixing performance of a commercial miniature mixers, DSM micro-compounder and a small twin screw extruder Prism, were evaluated for polymer blends and compared to the custom-built miniature mixers. For the compatibilized systems, PSMA/PA and PEMA/C20A, the morphology from samples mixed by the five different mixers did not show much difference. For PSMA/PA system, the Maleic anhydride groups reacted with PA during mixing and the reaction stabilized the interface between the two phases. Therefore, all

mixers produced a fine dispersed PA phase in a continuous PSMA matrix at three tested rotational speeds: 50, 100 and 150 rpm. No significant morphology change was observed with increasing rotor speed. For PEMA/C20A, a mixture of intercalated and exfoliated morphology was obtained for all mixers at rotational speeds of 50 and 100 rpm. The d-spacing of clay increased with larger rotor speed and an exfoliated structure was obtained at 150 rpm. While the reactive systems demonstrated that all small scale mixers have a comparable mixing performance as the larger mixer and have the ability to exfoliate the nanocomposites under favorable conditions, reactive systems are not suitable to allow us to discriminate the mixing abilities of different mixers.

For immiscible PS/PA system, BM and MBM generated morphology comparable to that obtained by Prism at 50rpm. The dispersed phases are spherical particles with diameters less than 2-3 microns. However, for PS/PA blend produced by APAM, the morphology showed some of the unstable elongated phases co-existing with spherical particles. This result indicates that a stable particle size was not reached after the set mixing time of 10 minute at 50 rpm. However, the size of the dispersed phases is still comparable to these mixed by BM and Prism. For the DSM, the dispersed particles were very big, on the order of 30-40 micron in diameter, and much coarser than particles formed in other mixers. The poor morphology produced by DSM results from, poor recirculation, low shear rate and lack of flow reorientation as confirmed by the simulation.

Overall, this thesis has demonstrated that using non-isothermal modeling based on fully filled geometries and non-Newtonian properties is an efficient tool to examine polymer processing. The heat transfer and flow information derived from the simulation provided the essential information needed for optimizing processing conditions and equipment designs. In terms of processing polymer blends and nanocomposites, the miniature mixers (MBM, APAM, and DSM) proved to be comparable to larger mixers (BM and Prism) for compatibilized systems and less efficient for immiscible systems. The in-house built miniature mixer MBM and APAM have an overall superior mixing ability to the commercial miniature extruder DSM based on the simulation and the experimental morphologies of non-reactive systems.

6.2 Future work

6.2.1 Temperature and torque measurements for APAM

In this thesis, the temperature and torque data for BM and MBM were measured and compared with the data from simulations. We were unable to track the temperature and torque data for APAM because originally APAM was not equipped with temperature and torque measurement device and data acquisition system.

Figure 6.1 shows the schematic drawing of a design that has a torque meter and a melt thermocouple for APAM. The thermocouple will be installed through a narrow channel in the rotor and will protrude into the mixer to monitor the real-time temperature change. These design modifications have been finished recently.

The experiment to measure the torque and the temperature as described in Chapter 2 and 3 for BM and MBM respectively should be carried out for APAM.

Acquiring the torque and temperature data for APAM will help us to better monitor the thermal and flow history of mixing happening inside the mixer and provide real data to compare to the simulation.
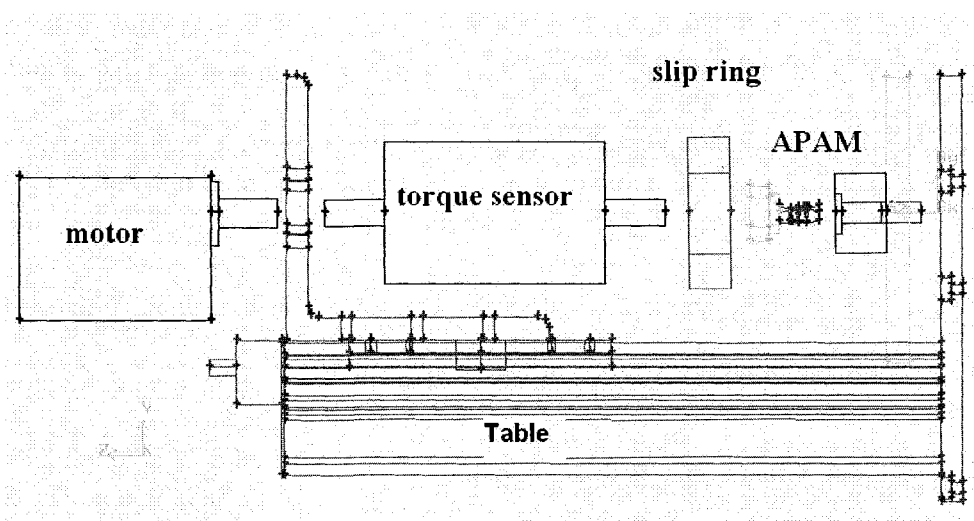
Figure 6.1: Schematic of the design equipping APAM with torque and temperature measurement.

6.2.2 Non-isothermal simulations for DSM micro-compounder and a twin screw extruder

Because it takes much more time and memory to do non-isothermal simulations, isothermal simulations were carried out for DSM and a kneading block of a TSE in Chapter 5 to illustrate the flow inside the extruders. If larger computational memory and parallel computation available, it would be of interest to see the temperature distribution and heat transfer for both mixers by performing non-isothermal simulations.

6.2.3 Mixing characterization of miniature mixers by simulation

We previously calculated the flow and thermal fields of the miniature mixers and obtained volumetric distribution of shear rate, shear stress and flow numbers, which can qualitatively give us a general idea of the stress and temperature distributions in the mixer. However, it is hard to tell which mixer has a better mixing efficiency from these values and we need to formulate mixing parameters to quantify it. Therefore, in the future work, we will use the former flow and thermal fields of these mixers to compute the trajectory of a large set of materials points and then analyze these results with statistical tools to obtain a global and quantitative overview of the mixing evolution. Polyflow will be used once to perform the mixing simulation and produce mixing files. These mixing files will be then read into Polystat, which is a postprocessor of Polyflow, to perform the statistical analysis.

Several parameters defined in literature to quantify the mixing in a mixer. A general approach to quantify distributive mixing is to examine the kinematics of laminar flow [1]. The distance change, λ, between two infinitely close particles is referred to as length stretch and expressed as following [2]:

$$\lambda(X,M,t) = \lim_{|dX| \to 0} \frac{|dx|}{|dX|} \qquad (6.1)$$

where dX is the initial distance between two particles and dx is the distance at time t. Similarly the area stretch, η, is defined as [2]:

$$\eta(A,N,t) = \lim_{|dA| \to 0} \frac{|da|}{|dA|} \qquad (6.2)$$

where dA and da are initial area and area at time t respectively. The value of λ and

η depends on the initial placement X or A, initial orientation M or N and

experiencing time t. A large value of λ or η throughout time and space is an

indication of very good local distributive mixing. The length or area stretch

distributions can be calculated from a set of particles. Time evaluation and

average values of these distributions can provide a quantitative measure of

distributive mixing efficiency.

The efficiency of stretching is defined as the comparable mixing ability of

different flows: [2]

$$e_\lambda = \frac{\dot{\lambda}/\lambda}{D}$$ (6.3)

where D is the magnitude of the rate of deformation and $\dot{\lambda}$ is the rate of stretching.

$\dot{\lambda}$ is a function of time and the initial position of the material. For pure viscous

fluid, the physical meaning of the efficiency is the fraction of energy dissipated

locally that is used to stretch fluid material.

Avaloss et al. [3] used the length stretch and the stretching efficiency to

discriminate the mixing efficiency of single cam, co-rotating cam and counter-

rotating cam. He found that the counter-rotating cam has a more uniform length

stretch distribution, which indicates a good distributive mixing efficiency.

However the efficiency and its time-averaged value are not significant for the

three systems.

Mans-Zloczower et al. [4] uses Renyi entropies to characterize distributive mixing. The relative entropy is defined as a ratio of the generalized dimension to the embedding space dimension:

$$S_{relative}(\beta) = d(\beta) / DES \qquad (6.4)$$

where $d(\beta)$ is the Renyi generalized dimension and DES is the dimension of the embedding space. The relative Renyi entropy equals 1 for perfect mixing and 0 for poorest mixing. The Renyi entropies are independent of the processing geometries, therefore, provides an efficient way to compare the mixing efficiency of different types of mixers.

Another method to assess distributive mixing in batch mixer was developed by Hutchinson et al [5]. Their method measured the behavior of the coefficient of variation during mixing and defined a variance as following:

$$\sigma^2 = \frac{1}{n-1} \sum_{i=1}^{n} (x_i - \overline{x})^2 \qquad (6.5)$$

where x_i is the number of material points in a particular wedge and is the average number of particles in each wedge. The coefficient of variation (CV) was then defined as:

$$CV = \frac{\sigma}{\overline{x}} \cdot 100 \qquad (6.6)$$

A normalized mixing parameter was modified as:

$$M = \frac{\sigma}{\overline{x} \cdot \sqrt{n}} \qquad (6.7)$$

where M= 1 for no mixing at all and M= 0 for perfect mixing. When this method was applied, the mixing region was divided into n parts and a set of material points was added for each part. Then these mixing parameters were calculated.

Wong and Manas-Zloczower [6] also use pair-wise correlation functions to study the overall distribution of the minor component in the mixing region in a batch type mixing equipment. They tracked the evolution of the distance between pairs of particles in the mixing chamber and used the correlation function to characterize the distributive mixing inside a 2-D mixing chamber.

Whether dispersive mixing occurs or not depends on the force balance between the applied hydrodynamics forces and the attractive force holding clusters and droplets together. So the magnitude of the shear stress is an important factor that determines the drop size distribution. Studies [7, 8] also show that elongational flows are more effective in breaking up agglomerates than simple shear flow. Most mixing equipment has very complicated geometry and produces both elongational flow and simple shear flow. Manas-Zloczower [9] defined a parameter MI (mixing index), which is usually called flow strength or flow number to quantify the dispersion:

$$MI = \frac{|D|}{|D| + |\omega|}$$

(6.8)

where $|D|$ and $|\omega|$ are the magnitudes of the rate of strain and vorticity tensors respectively. The value of λ is between 0 for pure rotation and 1 for pure elongation. For simple shear flow, the value is 0.5. This parameter was used by

Manas-Zloczower and coworkers [10, 11] to compare the dispersive mixing efficiency of different mixing equipment and processing conditions.

In their later work, Wang and Manas-Zloczower [12] also defined a flow strength parameter S_f to quantify the elongation flow components:

$$S_f = \frac{2(trD^2)^2}{tr\dot{D}^2}$$

(6.9)

Where $\dot{D}$ is the time derivative of D with respect to a frame of reference rotating with the same angular velocity as the fluid element. The flow strength parameter is normalized as following:

$$\lambda_{new} = \frac{S_f}{S_f + 1}$$

(6.10)

Similar to λ, λ_{new} is equal to one for pure elongation flow, 0.5 for pure shear and zero for pure rotation. They showed that λ_{new} is more rigorous than λ for mixing equipment comparison.

Avalosse et al [13] compared the dispersive mixing efficiency between co-rotating and counter-rotating twin-screw extruders using commercial software Polyflow (Fluent Inc.). They performed statistical analysis of shear stress, flow number and shear rate in these two mixers. The average values of these parameters and the probability function of the flow number were then used to evaluate the dispersive mixing. As defined previously, the area stretching η and the efficiency of stretching e_λ will be used to characterize the distributive mixing and compare the distributive mixing efficiency of the mixers. We will calculate the mean and standard deviation of the logarithm of stretching and the efficiency

of stretching, the time evolution of the probability function and percentile functions, and use these parameters to quantify the mixing efficiency.

The scale of segregation was also used to describe the uniformity of the minor component throughout the major phase. We will create a specific zone inside the mixer and fill it with the minor fluid, then after a certain mixing time we will study how well the minor phase is distributed.

Recently Manas and coworkers define Renyi entropies to perform the same task. We will write a user-defined subroutine and implement it in Polyflow to compute these values. We will compare the effectiveness of these mixing parameters and evaluate whether they can describe mixing well for these complex geometries.

From the shear stress field of a mixer, we already have a general idea of applied force on the dispersed phase when it passes a specific area. However for dispersive mixing, we not only require that the dispersed phase pass the region where the stress level is above a given threshold value but also needs the repeated ruptures of the minor component through this region. We need to know how often the fluid elements pass through the high stress region in the equipment within a specific processing time.

It is proposed to trace a number of the massless particles and calculate the mixing indexes (Both λ and λ_{new}) along the trajectories. The stress and MI experience of each particle can be found in a given processing time and then the number of particles that pass the specific stress and MI level can be calculated

using the histogram displaying the flow history of the particles. These analyses should be done for APAM and MBM.

6.3 References

1. Zegev Tadmor, Costas G. Gogos, *Principle of Polymer Processing*, Wiley Interscience publication, 1979.

2. J. M. Ottino, *The Kinematics of Mixing: Stretching, Chaos, and Transport*, Cambridge university press, 1989.

3. Th. Avalosse and M. J. Crochet, "Finite-element simulation of mixing: 1. two-dimensional flow in periodic geometry", *AICHE J.* **43(3)**, 577, 1997.

4. W. Wang, I. Manas-Zloczower and M. Kaufman, "Characterization of distributive mixing in polymer processing equipment using Renyi entropies", *International Polymer Processing,* **16 (4)**, 315, 2001.

5. B.C. Hutchinson, A. C. Rios and T. A. Osswald, "Modeling of the distributive mixing in an internal batch mixer", *International Polymer Processing*, **14 (4)**, 315, 1999.

6. Tang H. Wong and Ica Manas-Zloczower, "Two-dimensional dynamic study of the distributive mixing in an internal mixer", *International Polymer Processing*, **9 (1)**, 3, 1994.

7. R. L. Powell and S. G. Mason, "Dispersion by laminar flow", *AICHE J.* **28,** 286, 1982.

8. I. Manas-Zloczower, D. L. Feke, International Polymer Processing, IV, 3, 1987.

9. I. Manas-Zloczower, "Analysis of Mixing in Polymer Processing Equipment", *Rheology Bulletin,* **66 (1)**, 5, 1997.

10. H. H. Yang, I. Manas-Zloczower, "3-D flow field analysis of a Banbury mixer", *International Polymer Processing*, **VII (3)**, 195, 1992.

11. T. Li, I. Manas-Zloczower, "Flow-field analysis of an intermeshing counter-rotating twin-screw extruder", *Polymer Engineering and Science*. **34**, 551, 1994.

12. W. Wang, I. Manas-Zloczower, "Temporal distribution: the basis for the development of mixing indexes for scale-up of polymer processing equipment", *Polymer Engineering and Science*, **41 (6)**, 1068, 2001.

13. TH. Avalosse, Y. Rubin and L. Fondin, "Non-isothermal modeling of co-rotating and contra-rotating twin screw extruders", *Journal of Reinforced Plastics and Composites*, **21 (5)**, 419, 2002.